ASSESSMENT OF TROPOSPHERIC SLANT FACTOR MODELS: COMPARISION WITH THREE DIMENSIONAL RAY-TRACING AND IMPACT ON GEODETIC POSITIONING
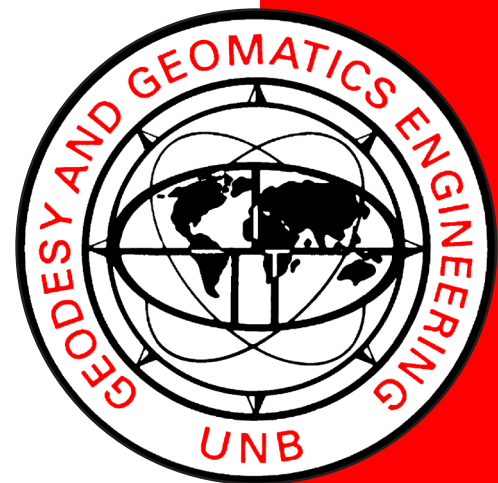
LANDON URQUHART

January 2011

ASSESSMENT OF TROPOSPHERIC SLANT FACTOR MODELS: COMPARISON WITH THREE DIMENSIONAL RAY-TRACING AND IMPACT ON GEODETIC POSITIONING

Landon Urquhart

Department of Geodesy and Geomatics Engineering
University of New Brunswick
P.O. Box 4400
Fredericton, N.B.
Canada
E3B 5A3

January 2011

PREFACE

This technical report is a reproduction of a thesis submitted in partial fulfillment of the requirements for the degree of Master of Science in Engineering in the Department of Geodesy and Geomatics Engineering, January 2011. The research was supervised by Dr. Marcelo Santos, and support was provided by the Natural Sciences and Engineering Research Council of Canada.

As with any copyrighted material, permission to reprint or quote extensively from this report must be received from the author. The citation to this work should appear as follows:

Urquhart, Landon (2011). *Assessment of Tropospheric Slant Factor Models: Comparison with Three Dimensional Ray-Tracing and Impact on Geodetic Positioning*. M.Sc.E. thesis, Department of Geodesy and Geomatics Engineering Technical Report No. 275, University of New Brunswick, Fredericton, New Brunswick, Canada, 166 pp.

Dedication

For Sellah

Abstract

The tropospheric delay still remains a limiting factor to the accuracy of space based positioning techniques. If this effect is not properly modeled it can adversely effect the accuracy and precision of station coordinates derived from these techniques. Particulary susceptible to errors in the delay, is the station height parameter which is important for geophysical studies such as studying sea level rise and isostatic adjustment and for the realization of a stable reference frame.

Ray-tracing through numerical weather models has been shown to be very beneficial for the development of mapping functions which model the elevation angle dependence of the tropospheric delay. Typically, due to computational constraints, only the vertical profile above the site is utilized, and the atmosphere is assumed to be spherically symmetric, therefore ignoring the azimuth-dependence of the delay. Instead of only using the vertical profile, it is possible to make no assumptions about the nature of the atmosphere and use the full information provided by the numerical weather model. Ray-tracing through the 3D state of the numerical weather model, generally referred to as 3D ray-tracing, makes it possible to model both the elevation angle- and azimuth-dependence of the tropospheric delay.

This contribution is divided into two parts, first an assessment of current mapping functions and functional formulations for describing both the elevation angle- and azimuth-dependence of the tropospheric delay is performed using the three dimensional ray-tracing

as truth data. The results of this experiment indicate that currently, the Vienna Mapping Function 1 (VMF1) should be used for all geodetic applications, and if necessary, the Global Mapping Function (GMF) can serve as an acceptable replacement without introducing a significant bias into the station position. Secondly, the Marini expression, truncated at three coefficients, is capable of modeling 3D ray-traced delays down to the $3°$ elevation angle with sub-millimeter accuracy and therefore it's use as the basis of current mapping functions is supported. In terms of modeling the asymmetry of the tropospheric delay with respect to azimuth, the Chen & Herring linear horizontal gradient formulation was found to be the best candidate when estimating the gradient parameters from space geodetic observations, although some tuning of the elevation dependent term may still be possible. The benefit of the higher order functional formulations was somewhat dependent on the nature of the asymmetric delay, although in general, the second degree spherical harmonics were better able to model the asymmetry of the delay at low elevation angles. In terms of estimating the unknown coefficients using the space geodetic observations, these higher order functions may not be practical as they introduce more unknown parameters into the design matrix. However, these formulations may be useful for providing asymmetric delay corrections in a convenient closed-form which can be distributed to end users.

The second experiment investigated the use of three dimensional ray-tracing at the observation level for the reduction of space geodetic observations. This consisted of a global precise point positioning (PPP) campaign comparing four strategies to modeling the delay. It was found that the use of three dimensional ray-tracing gave identical performance in the horizontal station repeatability as the current recommended approach of estimating two gradient parameters from the space geodetic observations, while in the vertical domain the estimation of the gradient parameters resulted in a small improvement. Both of these methods performed better than ignoring the asymmetric nature of the tropospheric

delay all together. Although the ray-traced zenith delays and the estimated zenith delays using the PPP approach agreed to the 3 mm level, the ray-traced zenith delays could not capture the short term fluctuations which occur, mainly due to the presentee of water vapor in the atmosphere. For this reason, it was still necessary to estimate a residual zenith delay parameter in order to achieve sub-cm repeatability in the vertical component.

Acknowledgments

This work was not completed without the help of many other people. Firstly, my supervisor Marcelo Santos. You have provided me with more opportunities than I could have imagined. Thank you for believing in me, supporting me, and helping me along the way. I have had the opportunity to work with many great students both at UNB and abroad.

In particular, Felipe Nievinski, thank you for laying the foundation which this work was built on and for providing me with excellent feedback on ideas and methodologies used in this work. Rodrigo Leandro for providing me with complete access to the GAPS source code, explaining the intricacies of the software, and for general advice which has greatly improved my understanding of precise point positioning. Thanks also to Alex, James, Lili and Robbie, my roommates in E19.

To the entire group of the Institute of Geodesy and Geophysics at the Technical University of Vienna, particularly Dr. Schuh and Dr. Boehm, for their financial support which allowed me to spend several months at their institute. The experience was very beneficial, both in terms of scientific collaboration, as well as the social aspect.

Also, the financial contribution of the Natural Sciences and Engineering Research Council of Canada, whose support allowed me to focus entirely on my research.

Finally, and most importantly, Sarah, for your love and support for all of these years and for putting up with me while I prepared this thesis.

Table of Contents

List of Tables

List of Figures

xviii

List of Symbols and Nomenclature

α	azimuth	rads
ΔL	total delay	m
ΔL^z	total zenith delay	m
ΔL_a	along path delay	m
ΔL_g	geometric delay	m
ΔL_h	hydrostatic delay	m
ΔL_{nh}	non-hydrostatic delay	m
ε	elevation angle	rads
$\boldsymbol{\nabla} n$	gradient of refractivity (vector)	$1/\mathrm{m}$
κ	slant factor model	unitless
λ	longitude	degrees
ϕ	latitude	degrees
ρ	total density of air	Pa
$\boldsymbol{r}$	position vector	m
c	vacuum speed of light	m/s
h	geodetic height	m
H_s	orthometric height of station	m
k	slant factor	unitless
k_1	coefficient of refractivity	K/Pa
k_2	coefficient of refractivity	K/Pa

k_2'	derived coefficient of refractivity	K/Pa
k_3	coefficient of refractivity	K^2/Pa
k_h	hydrostatic slant factor	unitless
k_{nh}	non-hydrostatic slant factor	unitless
N	refractivity	unitless
n	index of refraction	unitless
N_h	hydrostatic refractivity	unitless
N_{nh}	non-hydrostatic refractivity	unitless
P_d	partial pressure of dry air	Pa
P_w	partial pressure of water vapor	Pa
R_d	dry gas constant	$\mathrm{J}/\mathrm{kg} \times K$
R_w	water vapor gas constant	$\mathrm{J}/\mathrm{kg} \times K$
T	temperature	K
v	electromagnetic speed	m/s

Chapter 1

Introduction

As the accuracy of space geodetic techniques used for positioning continue to improve, so must the models used to mitigate error sources present in the observations. The effect of the electrically neutral atmosphere on signals propagating from outer space to receivers located on or near the Earth's surface is an important source of error where highly accurate positioning is required. This thesis evaluates the current state-of-the-art models used by the space geodetic community to mitigate the neutral atmospheric delay, identifies weaknesses in the current models and assesses various solutions to these problems.

To begin this chapter, I first discuss the motivation and objectives of this work, the contribution of this work to the geodetic community and provide an outline of the chapters to follow.

1.1 Motivation

The Earth is a continuously evolving body. In order to understand the forces which are driving this evolution, we often rely on the accurate determination of point positions on the Earth's surface. Space geodetic techniques such as very long baseline interferometry

(VLBI), global navigation satellite systems (GNSS) such as the Navstar Global Positioning System (GPS), laser ranging systems (SLR) and doppler systems have allowed for the determination of point positions with unprecedented accuracies. One limitation of these techniques is that they all rely on electromagnetic signals which must propagate through the Earth's electrically neutral atmosphere before being observed at the Earth's surface. This medium both delays the arrival of the signal as well as bends the path of the signal. For the determination of accurate positions both of these effects must be carefully modeled.

With the exception of the laser ranging techniques, the signals used in space geodesy fall within the microwave portion of the electromagnetic spectrum, shown in Figure 1.1. This work deals mainly with GPS but as VLBI and Doppler also fall within the same portion of the electromagnetic spectrum it can be applied equally to them as well.
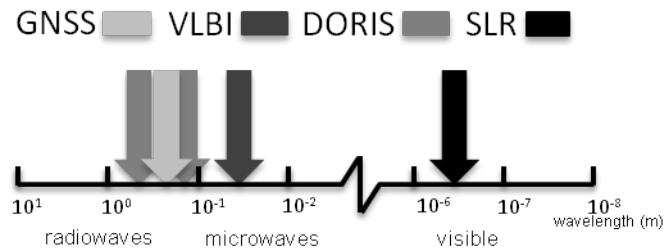
Figure 1.1: Location of the various space geodetic techniques in the electromagnetic spectrum.

As the signals propagate through the atmosphere they are both bent and delayed by the presence of electrically neutral particles. The majority of the delay is due to the troposphere, which is the portion of the atmosphere beginning at the ground and extending upwards to approximately 16km. Hence, the delay is often refereed to as the tropospheric delay. For a signal arriving at the zenith of the observer, the delay can reach a magnitude of 2.5 metres and increases quite rapidly with respect to the elevation angle. This delay is usually decomposed into two parts: a stable hydrostatic component; and a less stable,

more rapidly varying non-hydrostatic component.

Due to the less stable non-hydrostatic component, it is common practice in high accuracy applications to estimate a residual tropospheric delay parameter as an unknown along with the position and a receiver clock parameter. Due to the similarities in the partial derivatives of the residual tropospheric delay parameter and the station height parameter, it is common for an error in the troposphere delay model to be absorbed by the station height parameter.

The continuing need for improved tropospheric delay models is most important for applications requiring millimeter level accuracy in the height domain. Mendes [1999] compiled a comprehensive list of applications requiring millimetric height determinations. These include monitoring sea level rise, vertical motion due to isostatic adjustment, ice thickness variation, regional and global deformation monitoring, earthquake hazard mitigation, realization of reference frames, earth orientation parameters and time transfer. Because of the similarity between the partial derivatives of the station height and residual troposphere delay parameter these effects can be very difficult to separate and therefore it can lead to biases in the station height parameter which could result in incorrect interpretations of the geophysical signals derived from space geodetic techniques.

To illustrate this point graphically we can use several approximations and assumptions. The tropospheric delay increases with respect to a decreasing elevation angle (ε) approximately as $1/sin(\varepsilon)$. Hence, the propagation delay (ΔL), or range error, due to the troposphere can be expressed as:

$$\Delta L \approx \frac{\Delta L^z}{sin(\varepsilon)}, \tag{1.1}$$

where ΔL^z is the delay experienced by a signal arriving at the observer's zenith.

Treuhaft [1992] gives us an expression for a change in signal propagation time ($\Delta \tau$), in units of distance, due to a change in the station height (Δh):

3

$$\Delta\tau \approx \Delta h \cdot \sin(\varepsilon). \tag{1.2}$$

If for instance, as in Treuhaft [1992], we assume an error in station height of 2 cm along with an un-modeled clock bias of 3 cm, which is not uncommon, and a un-modeled zenith delay of 1 cm, from Figure 1.2 we can see that the range error caused by these phenomenon are very similar. It is only with the inclusion of low elevation observations, at least below 20 degrees, where we begin to see a separation between the height parameter and the residual troposphere delay parameter. The observations made at these low elevation angles are therefore critical to appropriately separate the height and troposphere parameters in the estimation process. However, the inclusion of the low elevation observations is only valid if we can properly model the troposphere delay at these low elevation angles.
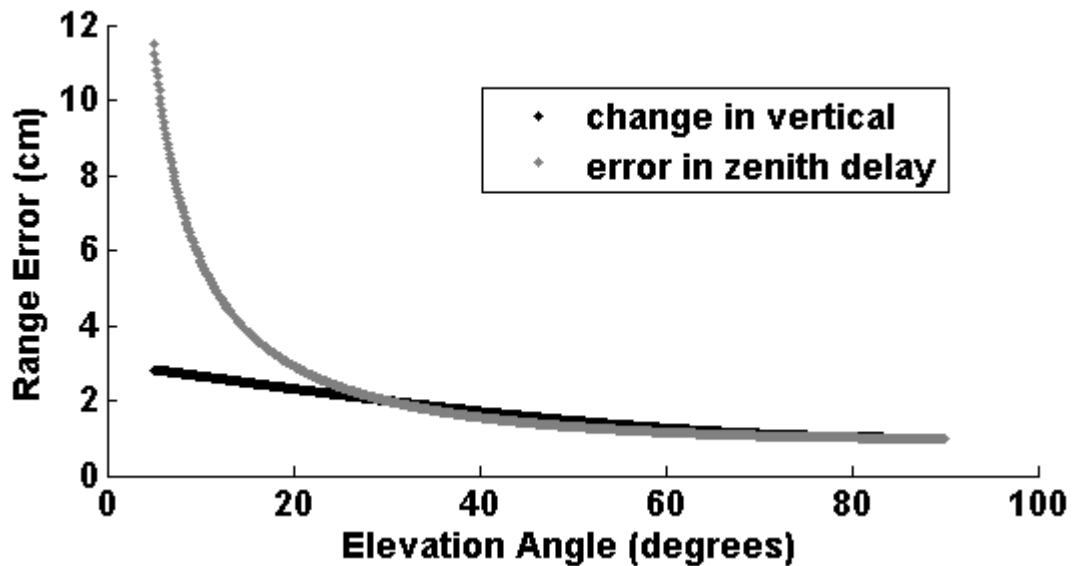
Figure 1.2: Comparison of range error due to a change in the station height along with a 3 cm clock error (black) to an error in the zenith delay (gray). After [Yunck, 1993]

The growth of the delay with respect to elevation angle can be modeled by applying a scale or slant factor, more commonly refereed to as a mapping function, which maps

the delay experienced at the zenith direction to a given elevation angle. A wide variety of mapping functions have been developed over the years and many of these mapping functions developed before 1996 have been tested by Mendes [1999]. Although these mapping functions have typically assumed that the atmosphere is symmetric (no azimuthal variation) they have still been able to produce very accurate results as this assumption is valid for observations arriving at elevation angles above 20–30 degrees.

On the other hand, the atmosphere is not symmetric by nature, but rather, can vary quite drastically with respect to azimuth especially at elevation angles below 10 degrees As discussed, these low elevation angle observations are essential to separate the height and troposphere delay parameters for accurate height determinations. MacMillan [1995] showed that ignoring the asymmetric portion of the delay can degrade the WRMS of a solution by more than 1 cm. Unlike the symmetric mapping functions, the models currently used for parameterizing the asymmetric delay have not been tested on a global, long term basis although several small scale studies (Pany et al. [2009] and Hobiger et al. [2010]) have suggested that they may be insufficient. Therefore it is necessary to properly assess these models and produce recommendations on which models should be used in high accuracy applications such as those discussed above.

Within the past decade, we have seen a large improvement not only in computing power but also in our ability to disseminate large amounts of data over the Internet. These developments have allowed for the use of numerical weather models (NWM) for the reduction of space geodetic observations. NWM are an essential tool for weather forecasters as well as climate scientists but have begun to play a larger and larger role in geodetic positioning.

In terms of modeling the tropospheric delay, the reliance on NWM can vary with several degrees of complexity. In the beginning, NWM were used as a substitute for surface measurements which are then fed into a priori zenith delay models. Rather than relying

on a model which predicts the zenith delay based on surface parameters, it is possible to quantify the zenith delay by modeling the signal as a ray and tracing its path through a profile extracted from the NWM. This was the technique employed in Jensen [2005] and Nievinski [2006] for both static-style and kinematic-style positioning. If we assume that the profile extracted from the NWM is valid for the entire sky, we can then ray-trace not only at zenith but also at various elevation angles. This approach has played an important role in the development of slant factor models (mapping functions) such as those created by Niell [2000] and Boehm and Schuh [2003].

The most complex method, which also uses the most information from the NWM, is to make no assumptions about the structure of the atmosphere and ray-trace through the entire three dimensional NWM (Chen and Herring [1997], Hobiger et al. [2008b], Nievinski [2009]). This technique has been made possible as computing power has increased to a point where we can now nearly apply this technique for the analysis of space geodetic data on an operational basis. However, the advantages of this technique for positioning accuracy have not yet been fully assessed on the global scale.

Böhm and VanDam [2009] describes the change from corrections based on simple mathematical formulas, to corrections based on large amounts of external data as a paradigm shift in the geodetic community. In order for this paradigm shift to be worthwhile, at least with respect to modeling tropospheric delays, we must answer the following questions:

- Is there is a deficiency in the current state-of-the-art mapping functions which must be addressed?

- Are the closed form expressions (functional formulations) capable of modeling the delay with sufficient accuracy to meet the demands of space geodetic applications?

- Do the new techniques such as three dimensional ray-tracing provide a significant improvement in the attainable accuracy and reliability of space geodetic techniques?

6

Answering these three questions are the motivation behind the research carried out in this thesis.

1.2 Contribution

The main contributions of this work are as follows:

- Review of the current state-of-the-art mapping functions and functional formulations recommended for use by the space geodetic community;

- Comprehensive assessment of current symmetric mapping functions and functional formulations on a global subset of 20 IGS stations for a year long period;

- First global assessment of Vienna Mapping Functions (currently recommended by the IERS for all geodetic applications) using an external weather model and ray-tracing algorithms;

- Comprehensive assessment of current asymmetric functional formulations and gradient mapping functions on a global subset of 20 IGS stations for a year long period;

- Characterization of global asymmetric tropospheric delay structures;

- Realization of the total, hydrostatic and non-hydrostatic gradient mapping function developed by Chen and Herring [1997] based on a database of three dimensional ray-traced delays from a high resolution NWM;

- First global campaign using three dimensional ray-traced slant factors applied at the observation level;

- Evaluation of ray-traced non-hydrostatic zenith delays compared to PPP derived zenith delays;

7

- Evaluation of tropospheric gradients derived from various techniques.

1.3 Outline

The document is organized in the following manner. I have begun Chapter 1 by discussing the motivation and objectives of this research along with its contribution to the geodetic community. Chapter 2 discusses the necessary theory, background and terminology of tropospheric delay modeling. Chapter 3 describes the current state-of-the-art models used by the geodetic community. This includes symmetric and asymmetric models as well as gradient mapping functions. The results and analysis of the thesis are divided into two sections: Chapter 4 and Chapter 5. The first section deals with assessing the current mapping functions and functional formulations using ray-tracing through the three dimensional NWM while the latter involves a global GPS campaign for evaluating the application of three dimensional ray-traced slant factors for geodetic positioning. Finally I conclude with Chapter 6 which summarizes the conclusions and recommendations arising from the work presented throughout this thesis.

Chapter 2

Background: Microwaves and the Neutral Atmosphere

This chapter describes the theoretical background and developments in modeling the propagation of electromagnetic waves as they pass through the Earth's neutral atmosphere. Sections 2.1 and 2.2 discuss how the propagation of electromagnetic waves is characterized in the atmosphere and how this in turn allows the calculation of the delay experienced by a signal.

Section 2.3 introduces the components of the delay, namely the zenith and slant components. Various approaches for modeling the zenith delay are discussed and the general formulation of the slant delay in terms of slant factors is presented. The need for a distinction between the terms mapping functions and slant factors is discussed which will aid in the discussion of the results to follow in Chapter 4.

Section 2.4 briefly describes the procedure of ray-tracing through NWM for modeling the tropospheric delay. The use of ray-tracing both as a tool for calibrating mapping functions as well as applied directly for the reduction of space geodetic observations is discussed. Two approaches for applying the ray-traced delays in geodetic software are

explained and the advantages and disadvantages are discussed. Finally, we conclude with an overview of the chapters to follow.

2.1 Refraction in the Neutral Atmosphere

The basic observable in space geodesy is the travel time of a signal from a transmitter to a receiver located on or near the Earth's surface. In a perfect vacuum, electromagnetic signals travel at a speed of light (c) which is $299,792,458$ m/s. As the Earth's atmosphere is not a perfect vacuum, instead being composed of both neutral and charged particles, the electromagnetic waves are retarded (and bent) as they pass through the Earth's atmosphere. The ratio of the speed of propagation in a vacuum as compared to the medium (v), is described by the refractive index (n) defined as:

$$n \equiv \frac{c}{v}.$$
(2.1)

The refractive index is more conveniently expressed as the refractivity (N), assuming that n does not vary from unity by more than a few parts per thousand, which is:

$$N = 10^6(n-1).$$
(2.2)

Although there are several formulations of the total refractivity of a point in the Earth's atmosphere we have chosen the formulation of Davis et al. [1985]. In this formulation, the total refractivity of air can be separated into two components: a ***hydrostatic component***, due to the dry gases (mainly to nitrogen and oxygen) and the non-dipole component of the water vapor; and a ***non-hydrostatic component*** which is due to the remaining water vapor [McCarthy and Petit, 2004].

The hydrostatic refractivity (N_h) is defined as:

$$N_{\mathrm{h}} \equiv k_1 R_d \rho, \tag{2.3}$$

and is dependent on an empirically determined coefficient k_1, the specific gas constant for the dry constituents of air (R_d) and the total density of air (ρ) which includes the density of both the dry constituents and of the water vapor.

The non-hydrostatic refractivity is defined as:

$$N_{\mathrm{nh}} \equiv k_2' \frac{P_{\mathrm{w}}}{T} + k_3 \frac{P_{\mathrm{w}}}{T^2}, \tag{2.4}$$

where $k_2' = k_2 - k_1 R_{\mathrm{d}}/R_{\mathrm{w}}$, P_{d} and P_{w} are the partial pressure of dry gases and partial pressure of water vapor in units of hectare pascals (hPa) and T is the temperature in units of Kelvin (K).

Thessin [2005], Rüeger [2002], Mendes [1999] and Bevis et al. [1994] provide discussions on several realizations of the empirically determined constants k_1, k_2 and k_3. Rüeger [2002] provides a very comprehensive review and based on past realizations recommends $k_1 = 77.6890(\mathrm{K}/\mathrm{hPa})$, $k_2 = 71.2952(\mathrm{K}/\mathrm{hPa})$ and $k_3 = 3.75463(\mathrm{K}^2/\mathrm{hPa})$ to be "*best average*" coefficients. For this reason we have chosen to use these values throughout this work.

The separation of the total refractivity into eqs. (2.3) and (2.4) is beneficial for geodesy as the hydrostatic component does not depend on the highly variable mixing ratio of dry gases and water vapor. This allows for a very accurate prediction of the hydrostatic component, relying only on surface parameters. Unfortunately, the non-hydrostatic refractivity cannot be predicted accurately using only surface measurements and alternative methods must be employed which will be discussed in section 2.3.1.

11

2.2　From Refraction to Signal Delay

The total delay (ΔL), expressed in units of length, is defined as the difference between the apparent ray-path length (the actual ray-path) and the geometric distance (path of the ray in a vacuum). Mathematically that is:

$$\Delta L = \underbrace{\int n(\ell)\,\mathrm{d}\ell}_{\substack{\text{bent} \\ \text{ray-path}}} - \underbrace{\int 1\,\mathrm{d}\ell}_{\substack{\text{straight} \\ \text{line}}}, \tag{2.5}$$

where the bent ray-path is the actual path of the ray, from the satellite propagating through the atmosphere to the receiver and the straight line ray-path is the theoretical path of the ray in a vacuum. The refractive index, n, is defined in a ray-based coordinate system, where ℓ is the distance along the path.

Assuming that the actual ray-path is known or computed iteratively, and the refractive index is available at any given point along the path, the total delay can be computed. The total delay can be separated into the along path delay (ΔL_a) and the geometric delay (ΔL_g):

$$\Delta L = \Delta L_a + \Delta L_g. \tag{2.6}$$

Using the relation between the refractive index (n) and the refractivity (N), the along path delay is equal to the integral of the refractivity (N) over the bent ray-path:

$$\Delta L_a = \underbrace{\int n(\ell)\,\mathrm{d}\ell}_{\substack{\text{bent} \\ \text{ray-path}}} - \underbrace{\int 1\,\mathrm{d}\ell}_{\substack{\text{bent} \\ \text{ray-path}}} = 10^{-6}\underbrace{\int N(\ell)\,\mathrm{d}\ell}_{\substack{\text{bent} \\ \text{ray-path}}}, \tag{2.7}$$

and the geometric delay is equal to:

$$\Delta L_g = \underbrace{\int 1\,\mathrm{d}\ell}_{\substack{\text{bent} \\ \text{ray-path}}} - \underbrace{\int 1\,\mathrm{d}\ell}_{\substack{\text{straight} \\ \text{line}}}. \tag{2.8}$$

12

In a similar manner, the along-path delay (eq. (2.7)) can be further separated into a hydrostatic (ΔL_h) and non-hydrostatic ($\Delta L_n h$) component:

$$\Delta L_a = \Delta L_h + \Delta L_{nh} = 10^{-6} \int\limits_{\substack{\text{bent} \\ \text{ray-path}}} N_h(\ell)\, \mathrm{d}\ell + 10^{-6} \int\limits_{\substack{\text{bent} \\ \text{ray-path}}} N_{nh}(\ell)\, \mathrm{d}\ell, \tag{2.9}$$

where N_h and N_{nh} are the hydrostatic and non-hydrostatic refractivity defined in eqs. (2.3) and (2.4).

The integration path for the hydrostatic and non-hydrostatic is the same. Therefore, it is not possible to separate the geometric delay from the along path delay and for practical purposes it is common to include the geometric delay with the hydrostatic delay. Thus, the total slant delay in its most basic form is given as:

$$\Delta L = (\Delta L_h + \Delta L_g) + \Delta L_{nh}. \tag{2.10}$$

2.3 Modeling the Delay

Following Nievinski [2009], in its most general form, the total delay is a function of epoch (or date and time (t)), receiver location (latitude (ϕ), longitude (λ) and height (h)) and satellite direction (given in the topocentric frame as elevation angle (ε) and azimuth (α)):

$$\Delta L = f(t, \phi, \lambda, h, \varepsilon, \alpha). \tag{2.11}$$

It is convenient to decompose the total slant delay into a zenith delay term (ΔL^z) and a slant factor (k):

$$\Delta L = \Delta L^z \times k, \tag{2.12}$$

where the total zenith delay is:

$$\Delta L^z = f(t, \phi, \lambda, h, \varepsilon = 90°), \tag{2.13}$$

and the variation of the delay is now contained to the slant factor which is a function of:

$$k = f(t, \phi, \lambda, h, \varepsilon, \alpha). \tag{2.14}$$

There are alternative terms for slant factor which have been used in the past. Both "obliquity factor" and "mapping function" have been used inter-changeably with slant factor. However, it is important to distinguish between these terms in order to properly aid the discussion. Both the slant factor and mapping function are a dimensionless quantity. By rearranging eq. (2.12) we can see that the slant factor is simply the zenith delay divided by the slant delay:

$$k = \frac{\Delta L^z(t, \phi, \lambda, h, \varepsilon)}{\Delta L(t, \phi, \lambda, h, \varepsilon, \alpha)}. \tag{2.15}$$

According to Nievinski [2009], a mapping function can be defined as a model for the variation of slant factors with respect to the independent variables. Therefore, a mapping function can be thought to be a slant factor model, denoted κ, while the evaluation of the mapping function results in the slant factor value, denoted k. Although the slant factor can come from several sources, in terms of mapping functions, the slant factor is obtained by evaluating a mapping function at a particular epoch ($t = t'$), position ($\phi = \phi', \lambda = \lambda', h = h'$), and direction ($\varepsilon = \varepsilon'$ and $\alpha = \alpha'$):

$$k = \kappa(t', \phi', \lambda', h', \varepsilon', \alpha'). \tag{2.16}$$

To facilitate the discussion of the errors associated with the slant factors, it is useful to

multiply the slant factor (or mapping functions) by a nominal zenith delay to allow for the expression of their error in units of length. In all cases to follow, we have chosen a nominal zenith delay equal to 2300 mm for the hydrostatic component and 220 mm for the non-hydrostatic component.

In a similar fashion to the slant delays, the slant factors can be further decomposed into a hydrostatic (including the geometric delay) and non-hydrostatic component. This leads to our final expression of the total delay in terms of slant factors and zenith delays to be:

$$k_{\mathrm{h}} \equiv \left(\Delta L_{\mathrm{h}} + \Delta L_{\mathrm{g}} \right) / \left(\Delta L_{\mathrm{h}}^{z} + \Delta L_{\mathrm{g}}^{z} \right) = \left(\Delta L_{\mathrm{h}} + \Delta L_{\mathrm{g}} \right) / \Delta L_{\mathrm{h}}^{z}, \tag{2.17}$$

$$k_{\mathrm{nh}} \equiv \Delta L_{\mathrm{nh}} / \Delta L_{\mathrm{nh}}^{z}, \tag{2.18}$$

$$\Delta L = k_{\mathrm{h}} \Delta L_{\mathrm{h}}^{z} + k_{\mathrm{nh}} \Delta L_{\mathrm{nh}}^{z}. \tag{2.19}$$

Equation (2.19) is the decomposition of the tropospheric slant delay which has become standard practice in geodetic positioning. The problem of tropospheric delay mitigation has benefited greatly from this decomposition of the mitigation problem into the distinct entities of zenith delays and slant factors. Early on, the zenith delay models and the slant factor models (mapping functions) were not clearly separated [Mendes, 1999]. This made the problem more complex because it required a complete solution for both the zenith delay modeling and the slant factor modeling rather then decomposing the problem into several smaller problems which could be approached concurrently. Next we will discuss how zenith delays and slant factors are modeled.

2.3.1 Zenith Delay Modeling

Although improving zenith delay modeling is not within the scope of this work, it is necessary to have an understanding of the different approaches which can be used for obtaining the zenith delay as there are several techniques, all of which have their benefits and drawbacks. Later on this will be used as one of the justifications for the choice of applying ray-traced slant factors, rather than ray-traced delays as discussed in section 2.4.

In-Situ Measurements This approach involves using measurements made at the site other than those from a space geodetic technique. This may include meteorological parameters (for example surface pressure, temperature and humidity), water vapor radiometers or Raman Lidars, among others, to obtain the delay. The hydrostatic component of the delay can be determined very accurately from only surface measurements and using the Saastamoinen model [Saastamoinen, 1972]. However, even with water vapor radiometers or Raman Lidars the non-hydrostatic delay can only be determined to an accuracy of several centimeters. Additionally, these techniques may suffer from equipment upkeep and maintenance, poor temporal resolution and are not capable of operating in rainy conditions. Bock et al. [2001] provides an excellent review of external calibration techniques for the zenith non-hydrostatic delay.

Estimation Using Space Geodetic Techniques Limitations of the external calibration techniques to model the zenith delay at a precision comparable to the measurement noise of the space geodetic observations led researchers to attempt to estimate a residual zenith delay parameter along with the other parameters of interest such as receiver position. Typically, an a priori hydrostatic zenith delay model is used, based on either NWM or in situ calibrations, to remove the more easily predicted hydrostatic zenith delay while the non-hydrostatic delay term is estimated. Of course, as there are errors present in the a priori

16

hydrostatic models, these along with other error sources may contaminate the residual delay estimation. However, this approach has proven to be very useful and is standard practice for high accuracy geodetic positioning.

In this approach the non-hydrostatic mapping function is used to map the slant observations to zenith, thereby making it a common parameter among all satellites. This allows for the estimation of a single residual delay parameter. Although for positioning purposes this parameter is treated as a nuisance parameter it can be useful for climatological studies as the wet delay can be easily converted to partial water vapor pressure.

Numerical Weather Models   Ray-tracing through refractivity fields obtained from NWM in the zenith direction has also been shown to work well for sub-decimeter accuracy positioning [Johnson et al., 2002] and [Cove, 2005]. However, due to limits in the temporal and spatial resolution of the NWM a residual zenith delay parameter must still be estimated for millimeter level positioning. The main limitation for using NWM to calibrate zenith delays is representing the small scale fluctuations of the water vapor in the atmosphere. To overcome these limitations, geodesists and meteorologists have worked together to study the assimilation of both GPS non-hydrostatic zenith and slant delays into NWM analyses [Ware et al., 2000]. These observations can provide important information concerning both the spatial and temporal variation of the water vapor content in the atmosphere.

Interpolation From Nearby Stations   Rather than assimilating the GPS derived zenith non-hydrostatic delay into a NWM, it is possible to simply interpolate the zenith wet delay from nearby stations. In this case the zenith non-hydrostatic delay is determined by estimating a residual delay using space geodetic techniques as described above. Usually to achieve high accuracies when interpolating, this approach is only viable where dense GPS networks are available. With the proper network infrastructure in place, these corrections can even be used in real time.

2.3.2 Slant Delay Modeling: Slant Factors and Mapping Functions

In section 2.3 we defined a mapping function as a slant factor model. When a mapping function is evaluated at a specific epoch, location and direction we then obtain a slant factor. The objective of slant factor modeling is to provide an end user with a convenient, closed-form expression for the tropospheric delay which can be used in an efficient manner. This is based on the belief that it is unreasonable to have users interacting directly with slant factors (as we will discuss in section 2.4) perhaps due to the large computational and storage demands this approach would require.

Following the convention introduced in Davis et al. [1993], but simply applying it to slant factors rather than in terms of the delay itself, it is convenient to model the elevation-dependence and azimuth-dependence of the slant factors independently. For the symmetric slant factor model, which assumes no azimuth dependent variation of the refractivity, we have:

$$\kappa_0(\varepsilon) = \kappa_{0_h}(\varepsilon) + \kappa_{0_{nh}}(\varepsilon), \tag{2.20}$$

where κ_{0_h} is the hydrostatic slant factor model which includes the geometric delay and $\kappa_{0_{nh}}$ is the non-hydrostatic slant factor model. We have dropped the parametrization in terms of epoch and receiver location for brevity.

The asymmetric slant factor model:

$$\delta\kappa(\varepsilon,\alpha)_j = \kappa_{G_j}(\varepsilon) \times F_{G_j}(\varepsilon,\alpha), \tag{2.21}$$

is comprised of two parts, one to model the change in the magnitude of the gradient with respect to elevation angle which we term the ***gradient mapping function*** ($\kappa_G(\varepsilon)$), and a second component to model the horizontal variation of the refractivity with respect to azimuth, which we term the ***gradient function*** ($F_G(\varepsilon,\alpha)$). The subscript j indicates the

hydrostatic or non-hydrostatic component.

The complete model for the slant factor, achieved by adding eq. (2.21) and eq. (2.20), can then be written, for the hydrostatic component:

$$\kappa_h(\varepsilon, \alpha) = \kappa_{0_h} + \kappa_{G_h}(\varepsilon) \times F_{G_h}(\varepsilon, \alpha), \tag{2.22}$$

and for the non-hydrostatic:

$$\kappa_{nh}(\varepsilon, \alpha) = \kappa_{0_{nh}} + \kappa_{G_{nh}}(\varepsilon) \times F_{G_{nh}}(\varepsilon, \alpha). \tag{2.23}$$

Most often the parameters of the gradient function are estimated directly from the space geodetic observations themselves. As the partial derivatives of the hydrostatic and non-hydrostatic gradient function are very similar it is not possible to estimate both components separately using space geodetic techniques, and normally a total gradient function is used. On the other hand, the hydrostatic gradient can be fairly well predicted as it is due to large scale gradients in temperature and pressure which are quite stable. By removing the asymmetric hydrostatic delay from the space geodetic measurements a priori, it is more likely that the gradients estimated using the space geodetic observations will reflect the non-hydrostatic gradient of refractivity which are due to small scale variations of water vapor in the atmosphere Niell [2003].

2.3.3 Development of Slant Factor Models

Equations (2.20) and (2.21) are the general form used for slant factor modeling today by the geodetic community. There have been many different slant factor models developed, in particular those that account for the symmetric portion of the delay were evaluated in Mendes [1999]. There are three basic components which all slant factor models must

include and they are shown in Figure 2.1.
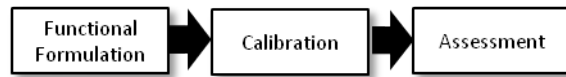
Figure 2.1: Steps in the development of a slant factor model.

The *functional formulation* is a closed-form, mathematical model for describing how the slant factors vary with respect to some parameter. The aim of the functional formulation is to compress the information contained in the slant factors and represent them in a way that can be easily distributed to, and implemented by, an end user. As we will see in Chapter 3 there are many different functional formulations available for modeling both the symmetric and asymmetric slant factors. Additionally, the parametrization of the functional formulation can be very different. For example, the Niell Mapping Function (NMF) [Niell, 1996] models the temporal variation of the slant factors by fitting a sinusoidal equation to each parameter which models only the seasonal and latitude dependent trends.

The *calibration* stage involves the realization of the functional formulation, the end result being a mapping function. There are many different options for realizing a functional formulation. One of the most commonly used methods is ray-tracing through a numerical representation of the atmosphere. Ray-tracing procedures can vary quite dramatically, using different assumptions about the path of the ray and structure of the atmosphere, and even the atmospheric sources could include radiosondes, climatologies or NWM. Therefore, the realization of the functional formulation can be significantly different depending on the procedure followed.

The purpose of the *assessment* is to identify any biases of the calibrated slant factor model and to give expected performance indicators. Typically each author, in developing a mapping function also performs an assessment to show the agreement with some truth

value. Normally, this truth value is once again obtained from ray-tracing. These evaluations can be done in an ad-hoc manner, with each slant factor model being evaluated using different criteria chosen by the author.

Mendes [1999] performed a comprehensive assessment of mapping functions developed before 1999 using a homogenous ray-tracer and assessment statistics and was able to draw conclusions on which mapping functions performed best with respect to this truth value. Several limitations to the study were that the ray-tracer assumed a spherically symmetric atmosphere, which is fine for evaluating symmetric mapping functions but which cannot be used to evaluate asymmetric models. Additionally, since this time there have been several new mapping functions developed based on NWM data and therefore these must also be assessed.

Additionally, due to inhomogeneity of the calibration stage of the mapping function development it is very difficult to evaluate the underlying functional formulation as differences in the calibration technique results in different realizations of the mapping function, rather than the functional formulation itself. For this reason we have chosen to use a homogenous approach and adopt a fixed atmosphere and ray-tracing procedure for both the calibration of the slant factor models and their assessment. Therefore the focus will solely on the functional formulations themselves which will hopefully aid in the development of future slant factor models. Next, the ray-tracing procedure used in the calibration and assessment will be reviewed.

2.4 Ray-tracing Through Numerical Weather Models

Ray-tracing has become an important tool for modeling the tropospheric delay. In the past, due mainly to computational constraints, ray-tracing has only been used as a way to calibrate functional formulations or assess the tropospheric delay models. However,

with advances in computing power and availability of numerical weather data sets, from which refractivity fields of the atmosphere can be computed, ray-tracing is on the verge of becoming a useful tool for the mitigation of the troposphere delay for highly accuracy positioning.

Ray-tracing is a method for describing the propagation of a wave or particle through a given medium. The ray's propagation is governed by the laws of geometrical optics and therefore obeys Fermat's principle of *least travel time*. The electromagnetic waves are modeled as a narrow beam, termed a *ray*. The 3-D Eikonal Equation, eq. (2.24), describes the propagation of the ray along the ray's path [Born and Wolf, 1999], and is given as:

$$\frac{\mathrm{d}}{\mathrm{d}\ell}\left(n\frac{\mathrm{d}\boldsymbol{r}}{\mathrm{d}\ell}\right) = \boldsymbol{\nabla}n, \tag{2.24}$$

where $\boldsymbol{\nabla}n$ is the gradient of refractivity, $\boldsymbol{r}$ is the position vector along the path, and $\mathrm{d}\ell$ is the incremental length along the path. In order to solve the differential equation shown in eq. (2.24), a number of approaches can be employed including Runge-Kutta [Hobiger et al., 2008a], perturbation method [Nievinski, 2009] or the shooting method [Boehm and Schuh, 2003].

In order to compute the delay, it is necessary to compute the refractivity at discrete intervals along the ray-path. From eqs. (2.3) and (2.4), the refractivity can be computed knowing the pressure, temperature and water vapor pressure. As discussed in section 2.3.3 these parameters can be derived from various atmospheric sources and must be interpolated, and in some cases extrapolated to obtain the parameters at the desired intervals. Details on the specific ray-tracing algorithms used in this work is given in Appendix IV and Nievinski [2009].

2.4.1 Numerical Weather Models for 3D Ray-tracing

Numerical weather model analyses provide three dimensional snapshots of the atmosphere's state. They are an essential tool for weather forecasting and are becoming more and more important for space geodesy. The applications of NWM within the geodetic community range from modeling surface deformation due to loading, earth rotation and gravity field variations; however, we focus solely on their use in modeling the tropospheric path delay.

Operational NWM are produced from the data assimilation cycle depicted in Figure 2.2. To begin, raw observations are acquired. These include over 700 radiosondes launched twice daily, surface stations both on land and on water, aircraft reports and satellite observations. Due to the large number of observations some filtering and quality control is required to ensure data consistency and to make the data manageable.

Figure 2.2: The data assimilation cycle.
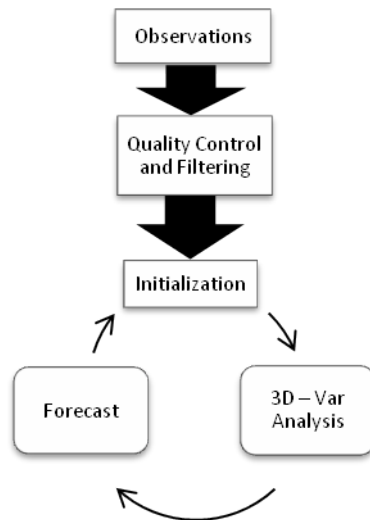
An initial model is necessary to act as the basis of the analysis and to act as boundary conditions for the physical processes used to model the atmospheric conditions. Additionally, for areas of the Earth which do not have observations present, the initial model

may be the only contribution to the analysis [Laroche, n.d.]. This initial model could be a climatological model, but more often the most recent forecast model is used as it is more accurate. Finally the observations are assimilated into the forecast model producing the analysis which is the essential component to the weather forecasting system [Laroche, n.d.]. From the analysis, the weather forecasting system, which we rely on every day to predict our weather, is produced.

For this research the Canadian Global Environmental Mesoscale model produced by the Canadian Meteorological Center (CMC-GEM) was used. The CMC-GEM consists of both a global model and a regional model. As we are interested in studying troposphere delay models over the entire globe, we have chosen the global model.

At the CMC, a global analysis is produced every twelve hours, at 00:00UTC and 12:00 UTC and forecasts are produced every three hours into the future up to 48 hours. Since September 20th, 2007, the global analysis covered an area from 85°N to 84.2°S and had a grid resolution of $0.6° \times 0.6°$. As of June 3rd, 2008, the coverage was expanded to include the entire globe while remaining at the same grid resolution.

In the vertical direction, the parameters of the NWM are provided on the following 28 constant isobaric levels (hPa): 1015, 1000, 985, 970, 950, 925, 900, 875, 850, 800, 750, 700, 650, 600, 550, 500, 450, 400, 350, 300, 275, 250, 225, 200, 175, 150, 100 and 50. Additionally, several parameters are provided at or near the surface. The parameters which are of interest for ray-tracing include the geopotential height, relative humidity, temperature and pressure.

One important note about the resolution of a NWM should be made. Although the grid resolution is usually given as an indicator of the ability of the NWM to resolve features in the atmosphere this is not the case. Realistically, a NWM can only resolve features that are $4--5$ times the actual grid resolution COMET-UCAR [1999]. This fact is one of the main limitations of NWM for space geodetic applications. Due to the spatial resolution

24

constraints, the small scale water vapor fluctuations are not resolvable in the analyses.

2.4.2 Ray-tracing for the Reduction of Space Geodetic Observations

Rather than using ray-traced delays as a means of calibrating a mapping function, there has been recent interest in using the ray-traced delays at the observation level. This is also known as ***direct mapping*** [Rocken et al., 2001]. The end goal of this approach would be to model the delay to such an accuracy that it is not necessary to estimate a residual zenith delay parameter. However, due to imperfections of the NWM, particularly for modeling the non-hydrostatic delay, it is still necessary to estimate a residual zenith delay parameter to obtain millimeter accuracy in the height domain.

The KAshima RAy-Tracing Service (KARATS), described in Hobiger et al. [2008b], is a web based ray-tracing service for applying ray-traced slant delays for geodetic position-ing, among other applications. KARATS relies on the Japanese Meteorological Agencies meso-scale 4D Var model which covers a large part of Eastern Asia. Users from this region can submit RINEX files (among other formats) to a web server which is connected to a ray-tracing cluster. The observation directions (outgoing elevation angle and azimuth) are determined using orbit files and then the ray-traced delays are computed and subtracted from the observations. A "reduced" observation file is then sent back to the user which is now free (at least in theory) from tropospheric effects.

To process the reduced observation file with a conventional software package several modifications are necessary. As the delays are applied directly, there is no longer a need for an a priori zenith delay. Hence, the a priori delay must be set to zero. Secondly, a residual zenith delay parameter must be estimated to account for the bias between NWM derived zenith delay and GPS estimated zenith delays. As the bias is, in general, on the centimeter level this can be done using a simple mapping function. In the case of Hobiger et al. [2008b], a basic mapping function of:

$$\Delta L(\varepsilon, t) = \frac{\Delta L_z(t)}{\sin \varepsilon}, \tag{2.25}$$

which is a function of time and elevation angle, is used.

The temporal variation of this residual zenith delay term can be modeled in the traditional manner using either a piece-wise linear function or a random-walk process. However, as the residual zenith delay parameter is much smaller than the traditional wet zenith delay that is estimated, the stochastic model should be adjusted to reflect this difference [Hobiger et al., 2008b].

Finally, using the slant delay approach, the total zenith delay is not directly recoverable from the estimation process. It is necessary to reconstruct the total zenith delay by adding the estimated residual delay parameter to a ray-traced zenith delay quantity.

An alternative method for applying ray-tracing at the observation level is to use the slant factor parametrization as done in [Nievinski et al., 2008; Urquhart et al., 2010]. In this case, the ray-traced slant factors can be used much in the same way current mapping functions are implemented. In theory, a similar web based service could be established. A user would submit an observation file and the directions to the targets (outgoing elevation angle and azimuth) would be computed. Instead of reducing the observations in the RINEX file, ray-traced slant factors for each RINEX observation would be computed, as per the definition of the slant factor:

$$k(t, \phi, \lambda, h, \varepsilon, \alpha) = \frac{\Delta L_z(t, \phi, \lambda, h, \varepsilon = 90)}{\Delta L(t, \phi, \lambda, h, \varepsilon, \alpha)}. \tag{2.26}$$

Rather than only computing the total delays, both the hydrostatic (including the geometric delay) and non-hydrostatic would be computed, then stored in a file and returned to the user.

To apply the slant factors in the software package, very little would need to change.

An a priori zenith delay would still be needed as is required in most software packages. This could come from several sources, either included with the slant factors (ie., ray-traced zenith delays) or from any method described in section 2.3.1. The residual zenith delay would be computed by using the non-hydrostatic slant factors to map the residuals to zenith, in the same manner a non-hydrostatic mapping function is used, and the same stochastic model could be implemented as in the traditional processing strategy. The output from the processing software would then allow for the direct estimation of the total zenith delay as an output.

Several advantages of the slant factor technique are that the observations themselves are not modified, thereby eliminating the chance of troposphere reduced observations being confused with the original observation files. The slant factor files could be produced and stored in a similar manner to the IGS precise orbit and clock products. Secondly, as the slant and zenith delay used to compute the slant factor share both the epoch and receiver location they are highly correlated. Therefore, the uncertainty present in each individual term is greater than the uncertainty of the slant factor itself as common errors will be mostly canceled out due to the correlation [Nievinski, 2009].

Although slant factors require the use of an a priori zenith delay this can actually be beneficial. The external calibration technique described in section 2.3.1 may prove to be more accurate for determining zenith delays than from ray-tracing through NWM, which are somewhat limited in accuracy due to spatial and temporal resolution. However, if the user does not have an external calibration method available, they can at least use the zenith delay as it is computed when determining the slant factors.

Finally, and perhaps most importantly, ray-traced slant factors used in the method described above can be applied in much the same way current mapping functions are provided and may be more intuitive for users to implement. As mentioned in section 2.3, a mapping function is simply a way of modeling slant factors, which in this case we are

providing explicitly to the user on a epoch-by-epoch, satellite-by-satellite basis.

Currently, a typical mapping function (VMF1 for example) requires the user position, epoch, and elevation angle of target. From these parameters, the hydrostatic and non-hydrostatic slant factors are returned and then multiplied by the a priori zenith delays. In much the same way, for the use of ray-traced slant factors, the user would be required to submit position, epoch, elevation angle and, in addition, azimuth to the target and from these the hydrostatic and non-hydrostatic slant factors are determined. Alternatively, the slant factors could be made a function of user position, epoch and satellite ID. As the only addition required is the azimuth of the target, this should allow for simpler adaptation of geodetic software packages rather then if the slant delays were used directly.

2.5   Summary

Chapter 2 reviews the theory behind troposphere delay modeling. The decomposition of the troposphere into separate parts was shown. We reviewed how we currently model the tropospheric delay in space geodetic applications, normally predicting the stable hydrostatic zenith delay, while estimating the non-hydrostatic component. We distinguished between a mapping function and a slant factor, the latter resulting from the evaluation of the former at a specific location, epoch and direction. We discussed the transition towards ray-tracing through NWM, not only for calibrating mapping functions but also for applying the ray-traced observables directly in the geodetic processing packages. Finally, we concluded with an overview of the chapters to follow.

2.6 Overview of Following Chapters

Coming back to the questions that were raised at the end of Chapter 1. For ray-tracing through the troposphere to become a standard processing strategy it is necessary to show that there are limitations to the way we currently model the troposphere delay and that ray-tracing can significantly improve the attainable positioning accuracies. The following chapters will be dedicated to testing these two hypotheses.

First we review the various functional formulations and mapping functions which can be used for modeling the elevation- and azimuth- dependence of the tropospheric delay Chapter 3. Chapter 4 will be evaluating the current mapping functions and functional formulations in use today to identify any weaknesses or limitations of these approaches. For this purpose three dimensional ray-tracing will act as truth data which will be used to evaluate the mapping functions and functional models. Chapter 5 considers the effect of different troposphere delay mitigation strategies on the estimated parameters, including receiver position, residual zenith delay and tropospheric gradients. Additionally, we will consider their effect on convergence time of the solutions. Here we will be trying to identify what is the optimal strategy for mitigating the tropospheric delay in geodetic applications. This will involve a global GPS precise point positioning campaign comparing the standard approaches for mitigating the tropospheric delay versus applying the slant factors at the observation level.

Chapter 3

Review of Functional Formulations, Mapping Functions and Gradient Models

This chapter describes the tropospheric models which will be systematically evaluated in this work. The chapter is organized in a manner to have a separation between the models based on a symmetric formulations and asymmetric formulations. The description of the mapping functions and functional formulations has been kept brief, focusing on the key points which distinguish the models from one another. For a complete discussion on the model the reader is asked to view the original references which are cited throughout this section.

3.1   Symmetric Models

Symmetric models are based on the assumption that the atmosphere can be adequately modeled, neglecting any horizontal variation in refractivity. For this reason the symmetric

models do not include an azimuth dependence in their parameterizations. For the majority of the sky this is a valid assumption although as we will see for low elevation angles this is no longer the case.

Over the course of their development, the functional formulations discussed below have been realized using various methods including ray-tracing through radiosonde data, climatologies and NWM. This makes the comparison of the functional formulation difficult. To avoid this downfall, we have realized the functional formulations using a homogeneous ray-tracing approach (more details in section 4.2.1) to allow us to compare the underlying mathematical models. By using this approach we hope to identify any shortcomings of the current mapping functions which use these functional formulations and thus aid the development of future mapping functions.

Since Mendes [1999], several new mapping functions have been developed. We have included these in the analysis as they represent the current state-of-the-art techniques for modeling the symmetric delay. Not only will this act as a validation and assessment for those models, but it will also allow us to identify any deficiencies in their development or realization.

3.1.1 Functional Formulations

Marini Continued Fractional Form: Marini [1972] showed that the elevation dependence of the tropospheric delay in a horizontally stratified atmosphere can be described as a continuous fraction of $1/sin(\varepsilon)$, which was normalized to yield unity at zenith by Herring [1992], to be:

$$\kappa(\varepsilon) = \cfrac{1 + \cfrac{a}{1 + \cfrac{b}{1 + \cfrac{c}{\cdots}}}}{\sin\varepsilon + \cfrac{a}{\sin\varepsilon + \cfrac{b}{\sin\varepsilon + \cfrac{c}{\cdots}}}}, \tag{3.1}$$

where a, b, c, $\cdots$ are unknown coefficients which must be determined, usually from ray-traced observations.

Marini [1972] found that by continuing the expression to four terms and tuning the coefficients, an error of less than 0.1 % of the delay could be obtained for elevation angles down to one degree.

Most mapping functions which are in use today use the expression from eq. (3.1), but the expansion is truncated at three terms rather than four. Both the three term and four term functional formulation will be evaluated.

As mentioned above, eq. (3.1) was originally intended for a horizontally stratified atmosphere. Although a good approximation, up until now the Marini expression has not been evaluated for a three dimensional atmosphere on a global scale and therefore this could identify any limitations to this approach.

Davis Continued Fractional Form: Chao [1972] and Chao [1974] modified the Marini continued fraction form by truncating it at two terms and replacing the second term with $tan(\varepsilon)$ to yield unity at the zenith. Davis et al. [1985] added a third term to this continued fraction to yield:

$$\kappa(\varepsilon) = \cfrac{1}{\sin\varepsilon + \cfrac{a}{\tan\varepsilon + \cfrac{b}{\sin\varepsilon + c}}}. \tag{3.2}$$

As $tan(\varepsilon)$ does not approach $sin(\varepsilon)$ quickly enough, this can potentially introduce a 1–2 mm error for elevation angles between $20°$ and $60°$ [Davis et al., 1985].

Davis et al. [1985] found that the functional formulation of eq. (3.2) could model the elevation angle dependence of the delay to within 3 mm for all elevation angles down to five degrees.

Generator Function Method: Yan and Ping [1995] developed an alternative continued fraction form based on the complementary error function. Once again the elevation dependence of the slant factor is modeled using a continued fraction form:

$$\kappa(\varepsilon) = \cfrac{1}{\cos\varepsilon + \cfrac{D_1}{I^2\sec\varepsilon + \cfrac{D_2}{\cos\varepsilon + \cfrac{D_3}{I^2\sec\varepsilon + D_4}}}}, \tag{3.3}$$

where D_1, D_2, D_3 and D_4 are the unknown coefficients. The parameter I is the normalized effective zenith argument defined as:

$$I = \sqrt{\frac{r_0}{2H}}\cot\varepsilon, \tag{3.4}$$

33

where r_0 is the radius of the Earth and H, the effective height of the atmosphere, is:

$$H = \frac{R_d T}{g},\qquad(3.5)$$

where R_d is the specific gas constant for dry air (287.06 J/kg*K), T is the surface temperature in Kelvin, and g is the gravitational acceleration at the center of the air column.

One drawback to this mapping function is that it is dependent on a surface parameter, temperature. Although in the past this parameter was determined from in situ observations or climatologies, we have used the NWM to derive the surface temperature.

According to Yan and Ping [1995] this functional formulation was not originally calibrated for the non-hydrostatic delay. In order for completeness we have chosen to calibrated the functional formulation to both the hydrostatic and non-hydrostatic delay slant factors.

3.1.2 Mapping Functions

Niell Mapping Function: Niell [1996] developed both a hydrostatic and a non-hydrostatic mapping function valid down to 3° based on the continued fraction expression of Marini [1972], normalized to yield unity following Herring [1992], truncated at the third term. The first term in eq. (3.6) represents the elevation dependence of the hydrostatic and non-hydrostatic mapping functions while the second term (to the right of the addition sign) is a height correction which is only applied to the hydrostatic mapping function to arrive at the functional form.

$$
\kappa(\varepsilon) = \cfrac{1 + \cfrac{a}{1 + \cfrac{b}{1+c}}}{\sin\varepsilon + \cfrac{a}{\sin\varepsilon + \cfrac{b}{\sin\varepsilon + c}}} + H_s \times 10^{-3} \left[\cfrac{1}{\sin\varepsilon} \cfrac{1 + \cfrac{a_{ht}}{1 + \cfrac{b_{ht}}{1 + c_{ht}}}}{\sin\varepsilon + \cfrac{a_{ht}}{\sin\varepsilon + \cfrac{b_{ht}}{\sin\varepsilon + c_{ht}}}} \right], \quad (3.6)
$$

where H_s is the orthometric height of the station. The height correction is required as the ratio of the atmosphere "thickness" to the radius of curvature of the Earth increases with height [Niell, 1996].

The mapping function was realized by a ray-tracing campaign performed through temperature and humidity profiles given at predefined pressure levels obtained from the U.S. Standard Atmosphere. The U.S. Standard Atmosphere provides nine profiles of temperature and humidity at latitudes of $15°N$, $30°N$, $45°N$, $60°N$ and $75°N$ for two epochs, January and July. The profile for $15°$ is valid for the entire year therefore there are only nine in total. These profiles were meant to represent mean longitudinal values of the whole of North America but were applied over the entire globe.

The three coefficients for both the hydrostatic and non-hydrostatic mapping function are calibrated by means of a least squares fit of nine ray-traces calculated between $3°$ and $90°$ in a spherically symmetric atmosphere. The coefficients are summarized in Tables 3.1 and 3.2.

The height correction coefficients (a_{ht}, b_{ht} and c_{ht}) were determined by a least squares fit of the ray-traced delays performed at the same nine elevation angles as before but varying the station height from 1000m to 2000m above sea level.

The temporal variation of the coefficients is modeled as a sinusoid with a period of

Table 3.1: Hydrostatic and Height correction coefficients for the NMF.

			Latitude		
coefficient	15	30	45	60	75
a	1.2769934e-03	1.2683230e-03	1.2465397e-03	1.2196049e-03	1.2045996e-03
b	2.9153695e-03	2.9152299e-03	2.9288445e-03	2.9022565e-03	2.9024912e-03
c	62.610505e-03	62.837393e-03	63.721774e-03	63.824265e-03	64.258455e-03
			Amplitude		
a	0.0	1.2709626E-05	2.6523662e-05	3.4000452e-05	4.1202191e-05
b	0.0	2.1414979E-05	3.0160779e-05	7.2562722e-05	11.723375e-05
c	0.0	9.0128400E-05	4.3497037e-05	84.795348e-05	170.37206e-05
			Height Correction		
a_{ht}			2.53e-05		
b_{ht}			5.49e-03		
c_{ht}			1.14e-03		

Table 3.2: Non-hydrostatic coefficients for the NMF.

			Latitude		
coefficient	15	30	45	60	75
a	5.8021897e-04	5.6794847e-04	5.8118019e-04	5.9727542e-04	6.1641693e-04
b	1.4275268e-03	1.5138625e-03	1.4572752e-03	1.5007428e-03	1.7599082e-03
c	4.3472961e-02	4.6729510e-02	4.3908931e-02	4.4626982e-02	5.4736038e-02

365.25 days:

$$a(\phi_i, t) = a_{avg}(\phi_i) - a_{amp}(\phi_i) \cos\left(2\pi \frac{t - T_0}{365.25}\right), \tag{3.7}$$

where the mean value, $a_{avg}(\phi)$, for a given latitude (ϕ) is taken as the average of the January and July values while the amplitude, $a_{amp}(\phi)$, is taken as half the difference of the January and July values. Equation (3.7) was applied in the same manner for the b and c coefficients. For the southern hemisphere a shift in phase of half a year is added to account for the fact that the seasons are inverted as there was no atmospheric data available.

Unlike the hydrostatic coefficients no clear temporal relationship for the non-hydrostatic coefficients was found. For this reason the non-hydrostatic coefficients are simply linear interpolated in both time and latitude.

Vienna Mapping Function: The Vienna Mapping Functions 1(VMF1), described in Boehm et al. [2006b] are based on ray-tracing through the European Center for Mid-range Weather Forecasting (ECMWF) operational analysis. The functional formulation chosen for this mapping functions was once again, the Marini continued (eq. (3.1)), normalized to yield unity at zenith,truncated at three coefficients. The unique approach to the VMF1 arises from determining the *b* and *c* coefficients as empirical functions which constrains the variation of the delay from these mean values to the *a* coefficient which is determined by inverting the Marini expression.

The VMF1 is site specific, although a gridded form has been developed and shown to be essentially equivalent in terms of accuracy [Kouba, 2008]. The gridded format is not limited to sites included in the IGS site list and can be used at any location. Currently, the VMF1 is recommended by the IERS for all geodetic applications.

Originally, the empirically determined functions for the *b* and *c* coefficients were taken to be equal to those of the Isobaric Mapping Functions (IMF) [Niell, 2000]. However, Boehm et al. [2006b] improved the hydrostatic coefficients using the ECMWF 40 year re-analysis to remove any systematic errors in the coefficients. The non-hydrostatic coefficients remained fixed to the NMF values at $45°$ as the non-hydrostatic delay is a factor of 10 smaller than the hydrostatic and therefore the small variations in the *b* and *c* coefficients are not significant [Boehm et al., 2006b].

The temporal variation of the hydrostatic *c* coefficient is modeled by:

$$c(\phi_i, t) = c_0 + \left[\left(\cos\left(\frac{(doy - 28)}{365} 2\pi + \Psi \right) + 1 \right) \frac{c_{11}}{2} + c_{10} \right] (1 - \cos\phi), \qquad (3.8)$$

where *doy* is the day-of-year, ϕ is the geodetic latitude and *Psi* specifies the northern (0) or southern (π) hemisphere. The coefficients are shown in Table 3.3. The *b* coefficient is fixed to a constant.

Table 3.3: Empirical b and c coefficients for computing the VMF1.

Hemisphere	b	c_0	c_{10}	c_{11}
Northern	0.0029	0.062	0.0	0.006
Southern	0.0029	0.062	0.001	0.006

The a coefficient is determined by ray-tracing at an outgoing elevation angle of $\sim$ 3° and then inverting the Marini expression to solve for the a coefficient, which for the gridded VMF1 are provided on a $2.0° \times 2.5°$ grid and have been made available from 1994 to present.

To ensure consistency in the assessment of the VMF1, two versions will be evaluated. We have chosen the site VMF1 for the analysis, but as Kouba [2008] found insignificant differences between the gridded and site VMF1 therefore results should be comparable for either choice. However, as the VMF1 is produced using the ECMWF NWM, we will also determine a separate VMF1 by ray-tracing through the CMC-GEM under the assumption of a spherical osculating atmosphere using the UNB ray-tracing algorithms develoepd origionally by Nievinski [2009] and later modified for this work. This is to prevent any differences in the atmospheric source from influencing the performance of the VMF1 functional formulation.

As the CMC-GEM is also used for the assessment this will ensure that any differences we find are due to the functional formulation (ie., constraining the variation of the delay to the a coefficient). We will name this functional form the UNBVMF to distinguish from the site VMF1.

Global Mapping Function: The Global Mapping Functions (GMF) [Boehm et al., 2006a], were developed to be compatible with the VMF1 mapping functions but do not require external inputs so they can be easily implemented into geodetic positioning packages while at the same time being consistent with NWM derived mapping functions.

Like the VMF1, the GMF use the Marini functional formulation normalized to yield unity at the zenith according to Herring [1992]. The b and c coefficients for both the hydrostatic and non-hydrostatic mapping function are obtained from the VMF1. The a coefficients are determined by ray-tracing through monthly mean values of pressure, temperature and humidity obtained from the ECMWF 40 year re-analysis data which was produced on a $15°$ by $15°$ grid for the a period from September 1999 to August 2002.

For each grid point a single ray-trace was performed for an outgoing elevation angle of $\sim 3.3°$ in the same manner as the VMF1. Using this ray-traced delay, the a coefficient is determined by inverting eq. (3.1) and solving for a. This results in 312 grid points for each of the 36 months of data.

The hydrostatic a coefficients are reduced to mean sea level using the height correction in Niell [1996]. Next the a coefficient time series at each grid point, for the hydrostatic and non-hydrostatic mapping function, are fitted to the sinusoidal function:

$$a = a_0 + A \cos \left(\frac{doy - 28}{365} 2\pi \right),$$
(3.9)

where doy is the day-of-year.

The phase of the sinusoidal function has been offset to day-of-year 28 as is the case for the NMF. Finally the mean value a_0, and the amplitude A, is expanded to a spherical harmonic function of degree and order 9 through a least square fit.

3.2   Asymmetric Functional Formulations

Asymmetric functional formulations have not received as much attention as the symmetric models due to the magnitude of the asymmetric delay being much smaller than the symmetric portion. Currently, the IERS suggests using the linear horizontal gradient model ([Chen and Herring, 1997], [Davis et al., 1993] and [MacMillan, 1995]) but has not gone

as far to define which gradient mapping function should be applied. Ghoddousi-Fard and Dare [2007] showed that differences in the gradient mapping functions can be as large as 34 mm at 5° elevation angle for a zenith gradient of 1.5 mm but did not assess which gradient mapping function performed the best.

Linear Horizontal Gradient, Davis: Davis et al. [1993], developed a gradient model based on a first-order Taylor series expansion of the refractivity at height h with respect to the horizontal position vector from the site $\boldsymbol{x}$ measured from the site to be:

$$N(\boldsymbol{x},h;t) = N_0(h;t) + \boldsymbol{\xi}(h;t)\boldsymbol{x}, \qquad (3.10)$$

where the refractivity at the horizontal position $\boldsymbol{x}$ and height h is $N(\boldsymbol{r},h;t)$, $N_0(h;t)$ is the refractivity at altitude z above the site and ξ is the horizontal gradient of refractivity above the site equal to:

$$\xi(h;t) = \frac{\mathrm{d}N(\boldsymbol{x},h;t)}{\mathrm{d}\boldsymbol{x}}. \qquad (3.11)$$

The term linear horizontal gradient is due to this first order Talyor series expansion used for describing the refractivity gradients. The final expression for the gradient model of the tropospheric delay is then formulated as:

$$\delta\kappa(\varepsilon,\alpha) = k_0(\varepsilon)\cot\varepsilon'\left[G_N\cos\alpha + G_E\sin\alpha\right], \qquad (3.12)$$

where ε' is the refracted elevation angle, and k_0 is a symmetric mapping function and G_N and G_E are the north-south and east-west tropospheric delay gradients. In some cases the hydrostatic mapping function is used, but more often than not the non-hydrostatic mapping function is used. In our case we will be estimating the symmetric mapping function given by Marini's three coefficient expression.

As we usually know the geometric elevation angle (computed from the coordinates of

the satellite or the extragalactic radio source) rather than the refracted or apparent elevation angle of the target, it is possible to relate the two quantities using the approximation [Bean and Dutton, 1966]:

$$\varepsilon' \approx \varepsilon + 10^{-6} N_s \cot \varepsilon, \tag{3.13}$$

where N_s is the surface refractivity.

Substituting eq. (3.13) into eq. (3.12) we arrive at an expression for the asymmetric slant factor, as a function of geometric elevation angle, rather than apparent elevation angle, and azimuth:

$$\delta \kappa (\varepsilon, \alpha) = k_0(\varepsilon) \cot \varepsilon \left(1 - 10^{-6} N_s \csc^2 \varepsilon \right) \left[G_N \cos \alpha + G_E \sin \alpha \right]. \tag{3.14}$$

Linear Horizontal Gradient, MacMillan: The requirement of surface refractivity in eq. (3.13) is a limitation as it requires external data. MacMillan [1995] found that the difference between using the geometric elevation angle rather than the apparent elevation angle when applying the asymmetric functional formulation to a VLBI campaign was insignificant. Therefore it was suggested to simply replace the apparent elevation angle in eq. (3.12) with the geometric elevation angle, to yield:

$$\delta \kappa (\varepsilon, \alpha) = k_0(\varepsilon) \cot \varepsilon \left[G_N \cos \alpha + G_E \sin \alpha \right]. \tag{3.15}$$

Linear Horizontal Gradient, Chen & Herring: Chen and Herring [1997] developed an expression for the asymmetric slant factor assuming that the refractivity varies linearly in the horizontal direction in the form:

$$\delta \kappa (\varepsilon, \alpha) = \frac{1}{\sin(\varepsilon) \tan(\varepsilon) + C} \left(G_N \cos \alpha + G_E \sin \alpha \right). \tag{3.16}$$

Here, the asymmetric delay is contained in the two coefficients G_N and G_E which are known as the tropospheric gradients. The elevation angle dependence of the asymmetric slant factor in eq. (3.16) is written in a continued fraction form, truncated at the first term, where C is:

$$C = \frac{3 \int \Delta N h^2 dh}{2 \int \Delta N h (h + r_0) dh}, \qquad (3.17)$$

and ΔN is the gradient of refractivity, h is the station geodetic height and r_0 is the radius of the Earth.

The coefficient C can be evaluated several different ways, either by direct integration of eq. (3.17), estimated from ray-traced slant factors, or computed by making several simplifying assumptions about the structure of the atmosphere.

For most purposes, the hydrostatic value of C is taken to be 0.0031, while for the non-hydrostatic a value of 0.001 is used. As it is difficult to estimate the hydrostatic and non-hydrostatic gradients separately, Herring [1992] suggested a values of 0.0032 for estimating the total gradients.

As the above quantities were determined by ray-tracing through a NWM with a grid resolution of approximately 200km, it may be possible to improve the values of the C coefficient by using a NWM with higher resolution [Niell, 2003]. We will evaluate the use of the suggested values for the C coefficient as well as estimate independent ones to see if it is possible to improve the formulation.

Linear Horizontal Gradient, Meindl: Meindl et al. [2004] developed a linear gradient model based on the idea of a tilting of the atmosphere to represent the tropospheric gradients. Using the law of sines, and assuming a small tilt, the asymmetric slant factor can be written as:

$$\delta \kappa (\varepsilon, \alpha) = f(z + \delta z) = f(z + G_N \cos \alpha + G_E \sin \alpha). \qquad (3.18)$$

By using a Taylor series expansion, truncated after the first term, the asymmetric slant factor can be written as:

$$\delta\kappa(\varepsilon,\alpha) = \left(\frac{\partial f}{\partial z}G_N\cos\alpha + \frac{\partial f}{\partial z}G_E\sin\alpha\right), \tag{3.19}$$

where $\frac{\partial f}{\partial z}$ is the derivative of a symmetric mapping function. Any mapping function can be substituted as the symmetric mapping function ineq. (3.19). We have evaluated the use of the hydrostatic and non-hydrostatic NMF.

By comparing eq. (3.19) to eq. (3.12), and eq. (3.16) the only difference between these expressions are the gradient mapping functions. The representation of the gradients themselves are all equivalent and will be referred to as the linear horizontal gradient functional formulation.

2nd **Order Polynomial:** Seko et al. [2004] introduced a 2nd order polynomial model as an attempt to improve upon the linear gradient models shown above. The expanded model is as follows:

$$\delta\kappa(\varepsilon,\alpha) = k_0(\varepsilon)\cot\varepsilon\left[G_{NN}^2\cos^2\alpha + G_N\cos\alpha + G_{NE}\cos\alpha\sin\alpha + G_E\sin\alpha + G_{EE}^2\sin^2\alpha\right].$$
$$\tag{3.20}$$

Notice that the elevation dependence of the gradient function still uses the same approach as the standard linear horizontal gradient model but we now have the addition of the G_{NN}, G_{NE} and G_{EE} terms which represent the higher order gradients present in the atmosphere.

Seko et al. [2004] found that the 2nd order formulation improved the positioning results in simulations with respect to the linear gradient model, at least in the case where small scale atmospheric fluctuations are present. However, this approach may not be practical

for estimation of the tropospheric gradients along with the receiver position using space geodetic techniques as the addition of three parameters (on top of the standard two gradient parameters G_N and G_E) would greatly hinder the estimation process.

Spherical Harmonic Expansions: Spherical harmonics have been widely used by the geodetic community for modeling various phenomena such as the Earth's gravity field, orbit perturbations, and antenna phase center variations. Böhm and Schuh [2001] suggested that it may be possible to use spherical harmonic expansions to describe the elevation and azimuth dependence of the tropospheric delay.

The expression for the surface spherical harmonics is given as:

$$Y(\theta, \lambda) = \sum_{n=0}^{n_{max}} \sum_{m=0}^{n} a_{nm} P_{nm}(\sin \theta) \cos(m\lambda) + b_{nm} P_{nm}(\sin \theta) \sin(m\lambda). \qquad (3.21)$$

In order to apply the spherical harmonics expression to the standard tropospheric mapping functions we define a spherical coordinate system whose origin is at the antenna, in a similar approach to Rothacher et al. [1995], where the spherical harmonic expression, equation 3.22, is in terms of azimuth and zenith angle as:

$$Y(z, \alpha) = \sum_{n=0}^{n_{max}} \sum_{m=0}^{n} a_{nm} P_{nm}(\sin(2z)) \cos(m\alpha) + b_{nm} P_{nm}(\sin(2z)) \sin(m\alpha), \qquad (3.22)$$

where P_{nm} represents the normalized associated Legendre functions, A_{nm} and B_{nm} are the unknown spherical harmonic coefficients of degree n order m, z is the zenith angle, which is the complement of the elevation angle.

Depending on the value of n and m chosen for the spherical harmonic expression, the sphere is divided into various components. If $m = 0$ we have *zonal harmonics* which divide

the sphere into $n+1$ zones. If $n=m$ the result is *sectoral harmonics* which divides the sphere into n positives and negative values. Finally there are *tesseral harmonics*, which occur when $m \neq n$ thereby dividing the sphere into tiles, each of which can represent a positive or negative value.

The use of spherical harmonics for estimating the gradients from geodetic observations is once again hindered by the addition of several parameters to the design matrix. However, they could be useful for removing the hydrostatic gradients a priori, or as a type of compression to store mapping function coefficients based on three dimensional ray-tracing.

3.3   Summary

We have reviewed the current state-of-the-art expressions for modeling both the symmetric and asymmetric troposphere delay. In the following chapter, we will begin the evaluation of these models using three dimensional ray-tracing to determine which functional formulations and mapping functions perform the best and should therefore be used for processing space geodetic observations for the highest accuracy.

Chapter 4

Evaluation of Current Mapping Functions and Functional Formulations

The purpose of this chapter is to assess the current state-of-the-art tropospheric models using ray-tracing through a three dimensional NWM. The tropospheric models assessed are those described in Chapter 3 including the functional formulations and mapping functions.

First, the previous work presented in the literature, related to the validation of functional formulation and mapping function is discussed. Here the focus is on the past work which has used ray-tracing as a means of validation rather than those works which have used geodetic observation campaigns. Next, a description of the experiment design is given including the need for a homogenous approach for validating the models. This includes a description of the observation geometry of the ray-traced slant factors, the fitting approach of the functional formulations and the assessment criteria.

The results and discussion are divided by mapping functions and functional formulations. Within each group we have further separated the results by hydrostatic and non-hydrostatic when applicable. For the asymmetric functional formulations we are also interested in the total delay as it is common to estimate these parameters using geodetic

observations. Finally, a summary of the key findings and recommendations are given.

4.1 Previous Work

For a long time ray-tracing has been an important tool for both the evaluation of and calibration of mapping functions. Most often, the ray-tracing has either been performed using radiosonde profiles, as in Marini [1972] and Yan and Ping [1995], or using representations of the atmosphere, whether it be climatologies [Niell, 1996] or state-of-the-art NWM [Boehm et al., 2006b].

Many mapping functions rely on empirical functions to model the variation of the coefficients with respect to some parameter. The advantage of this approach is that the mapping functions require no external data and can be easily implemented into existing geodetic software packages. Several examples of these types of mapping functions include those developed in Davis et al. [1985], Yan and Ping [1995], Niell [1996] and Boehm et al. [2006a]. These mapping functions do not directly rely on the NWM for their parametrization.

With the exception of the GMF [Boehm et al., 2006a], the mapping functions discussed above have been comprehensively assessed by several authors including Janes et al. [1991], Mendes [1999] and Ifadis [2000]. As these mapping functions only model trends or mean climate variations they are not able to capture the day-to-day variation of the atmosphere and therefore it has been found that no one mapping function performs best under all conditions and criteria. Especially for elevation angles below 7 degrees, these earlier mapping functions were not capable of modeling the delay to the accuracy needed for millimeter level positioning.

The next group of mapping functions are those that are directly parameterized by ray-tracing through NWM data. These include those developed by Niell [2000] and Boehm

et al. [2006b]. These are typically provided on sub-daily intervals and require external data for their computation. In the case of Boehm et al. [2006b], the mapping functions are calculated every 6 hours coinciding with the availability of the ECMWF analyses. Because of this parametrization these mapping functions are able to capture the sub-daily fluctuations of the tropospheric delay.

In the previous literature, most of the assessments of mapping functions have relied on the assumption of a horizontally stratified atmosphere. Even the functional formulations themselves are dependent on this assumption. Therefore there is a need to assess the functional formulations using a more realistic model for the atmosphere, making no assumptions about the structure of the atmosphere or variation of the refractivity.

Ichikawa et al. [2008] performed an assessment of the NMF, IMF and VMF over a small region of Eastern Asia by ray-tracing through the three dimensional JMA meso-scale analyses model. Only the total slant delay was compared, rather then its components, and it was found that large biases between 18 and 90 mm exist for the empirical mapping functions which were believed to be caused by the water vapor variability. Eresmaa et al. [2008] also assessed the NMF and VMF performance under the passage of a cold front and found that the prescribed mapping functions coefficients did not preform as well as when the coefficients were parameterized directly from the ray-traced delays. In this case the NWM used was the ECMWF HIRLAM.

For the asymmetric functional formulations fewer studies have been performed using ray-tracing through three dimensional refractivity fields. This is partly due to the complexity and computation demands of this technique. Pany et al. [2009] and Hobiger et al. [2010], both using KARATS, found that the linear horizontal gradient model, as given in Davis et al. [1993], may not be sufficient to capture the azimuth dependence of the delay for a severe weather system. Ghoddousi-Fard and Dare [2007] compared several of the gradient mapping functions and found that at 5 degrees they can vary by more than 3 cm

but did not go as far as to recommend which one performed most realistically. Once again using the passage of a cold front, Eresmaa et al. [2008] concluded that the linear gradient model was sufficient in this case.

Thus far, the assessment of these functional formulations has been performed on regional areas for short periods. Although this is very beneficial as it allows for the use of higher resolution NWM, it is difficult to expand the conclusions drawn from these individual studies. In order to draw conclusions on the overall performance of these models, there is a need for a comprehensive study on the long term behavior of these models under a wide range of conditions.

4.2 Experiment Description

In this section we describe the assessment of the tropospheric delay models. We first detail the need for a homogenous approach to the assessment. Secondly we describe the observation campaign undertaken to allow for a comprehensive assessment on a global basis. Finally, before moving on to the results, the statistical assessment of the models will be discussed.

4.2.1 Rationale for a Homogeneous Assessment

As discussed in Chapter 2 the underlying functional formulations of many mapping functions are the same, but their realization can be quite different. Their realization may differ in terms of:

- Atmospheric Modeling:
    - atmospheric source;
    - atmospheric structure;

- data assimilation.

- Ray-tracing Algorithms:

  - refractivity formulation;
  - ray-path formulation;
  - numerical solver.

- Slant Factor Compression:

  - functional formulation;
  - calibration method.

Comparing functional formulations becomes even more complex if we consider formulations which require auxiliary variables such as described in Yan and Ping [1995]. For this reason the evaluation is typically of the mapping function as a whole (functional formulation and calibration), as was the case in Mendes [1999], rather than any one specific aspect of the realization. Assessment of the mapping functions, although very beneficial, does not give insight into the performance of the underlying functional formulation used to represent the elevation angle- and azimuth- dependence of the slant factors. This insight could be beneficial for developing future mapping functions.

In order to identify which functional formulation may be best suited for future mapping functions, we have chosen to calibrate the underlying functional formulations using a homogenous approach. By keeping the calibration approach fixed between functional formulations, it allows us to remove any uncertainty which may be due to the realization of the various mapping functions and therefore draw conclusions about the functional formulations themselves. That said, we have also chosen to include the current state-of-the-art mapping functions as this will act as a reference point to judge the performance of the functional formulations and identify any limitations in the mapping functions.

4.2.2 Observations

Three dimensional ray-tracing was performed as detailed in Appendix IV using the global CMC-GEM operational analyses. The assessment was performed for twenty stations shown in Figure 4.1 at epochs of 00:00UTC and 12:00UTC from January 1st, 2008 to December 31st, 2008.
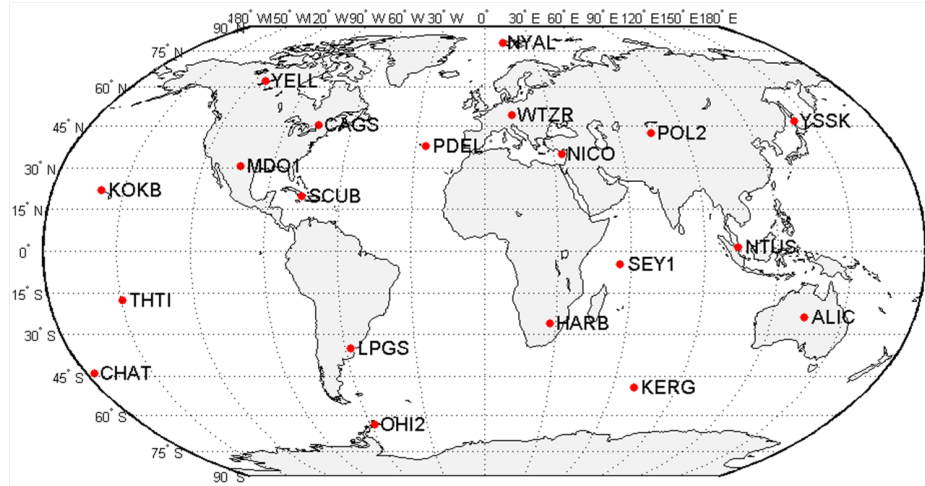
Figure 4.1: Global subset of IGS stations used in the assessment.

For each epoch and station, slant factors were computed according to eq. (2.15). For each epoch and station a total of 289 slant factor observations were made at elevation angles of 3°, 5°, 7°, 10°, 14°, 20°, 40°, 70°, and zenith and for every 10° in azimuth. In all, over 4 million slant factors were observed. These ray-traced slant factors will be referred to as observations in the text to follow.

These ray-traced directions taken for each epoch and station are a subset of all possible directions. Ideally, to perform such an assessment, we would observe on an infinitesimally dense grid of ray-traced observations, each weighted accordingly, and accounting for their correlations. Obviously, this approach would not be efficient for the analysis of long time series. As well as the NWM have a finite resolution for the features which it can resolve,

51

the observation of a dense grid would be highly correlated. Therefore, we have attempted to form a subset of observations which sample the slant factors at a sufficient density to capture the spatial fluctuations of the refractivity in the NWM. This is done by sampling at directions where we expect the slant factors to vary the most.

The objective of choosing the ray-traced directions was to obtain a sample which adequately represented the slant factors over the whole of the sky. The elevation angles were chosen as they approximately represent how the delay grows with elevation angle. This implies that they are approximately evenly spaced in $1/\sin(\varepsilon)$. The azimuth directions were chosen as they represent a conservative estimate of the smallest features a NWM with grid space equal to that of the CMC NWM can represent. Validation of the choice of directions is performed in Appendix III whereby we compare the reduced observation scheme to a dense $1° \times 1°$ grid of ray-traced observations over the entire sky, for a high resolution NWM.

4.2.3   Calibration of Functional Formulations

The ray-traced slant factors described in section 4.2.2 are fitted to the coefficients of the functional formulations using a non-linear least squares approach, for each epoch and station. The fitting of the functional formulations is not a trivial task as in some cases it is an ill-conditioned problem (see Appendix II). An ill-conditioned least squares problem is one in which small changes in the observations, result in large changes in the estimated parameters. This is normally due to a nearly linear dependence between the columns of the design matrix or in our case, most likely due to poor scaling of the design matrix elements.

The least squares problem can be stated as:

$$\boldsymbol{F}(\boldsymbol{x}) = \sum_{i=1}^{n} [y_i - f(x_i)]^2, \tag{4.1}$$

where we attempt to find the parameters, x_i, which minimizes the function $\boldsymbol{F}$, for a functional formulation $f(x_i)$ used to model the observations y_i (slant factors).

It is possible to solve for the unknown parameters using an iterative approach whereby an initial guess, $\boldsymbol{x}_0$, is updated with an increment of $\boldsymbol{\delta x}$:

$$x_1 = x_0 + \boldsymbol{\delta x}. \tag{4.2}$$

The method for computing the parameter update, $\boldsymbol{\delta x}$, is what differentiates the non-linear least squares algorithms. Ideally, to achieve fast convergence, we want to have large increments when we are far away from the final value, and small increments when we are approaching the final value, so as not to overshoot the optimal value of $\boldsymbol{x}$. The Levenberg-Marquadt [More, 1978] algorithm, although not optimal in any sense, provides a good balance and is one of the most popular approaches to solving non-linear least squares problems in practice.

The update parameter in the Levenberg-Marquadt method is calculated by inverting the system of equations and solving for $\boldsymbol{\delta x}$ [Gill et al., 1981]:

$$\boldsymbol{\delta x} = -(\boldsymbol{J}_i^T \boldsymbol{J}_i + \lambda_i \boldsymbol{I})^{-1} \boldsymbol{J}_i^T \boldsymbol{f}(\boldsymbol{x}_i), \tag{4.3}$$

where $\boldsymbol{J}$ is the jacobian:

$$\boldsymbol{J} = \left[\frac{\partial \boldsymbol{F}}{\partial \boldsymbol{x}} \right]. \tag{4.4}$$

The expression $\boldsymbol{J}_i^T \boldsymbol{J}_i$ is the first order term of the Hessian matrix. The truncation of the Hessian is only valid if the residuals are relatively small [Nocedal and Wright, 2006]. The term λ_i controls the search direction and magnitude of the step sizes.

For poorly scaled least squares problems eq. (4.3) can experience numerical difficulties and potentially produce poor solutions. By substituting the diagonal terms of the Hessian matrix into eq. (4.3) in replacement of $\boldsymbol{I}$, the spherical trust region is transformed into an

ellipsoidal trust region which reduces the possibility of poor results due to the scaling of the Hessian matrix [Nocedal and Wright, 2006]. The final update vector then becomes:

$$\boldsymbol{\delta x} = -(\boldsymbol{J}_i^T \boldsymbol{J}_i + \lambda_i diag(\boldsymbol{J}_i^T \boldsymbol{J}_i))^{-1} \boldsymbol{J}_i^T \boldsymbol{f}(\boldsymbol{x}_i). \tag{4.5}$$

4.2.4 Assessment Statistics

The two purposes of the assessment performed in this chapter are: (a) **model selection**, whereby we attempt to choose the model which can minimize the tropospheric delay error; and (b) **error prediction** whereby we obtain an estimate of the expected performance of each model over a significant period on a global scale. Here, the term *model* can apply to the mapping functions, the functional formulations or the a priori gradient models.

As discussed in section 4.2.3, the functional formulations are fitted to a subset of all possible ray-traced directions using the least squares criterion. The least squares estimator is popular because it provides an unbiased estimate of the unknown parameters which minimizes the sum of the squares of the residuals. However, when a subset of all possible observations are chosen, we can not assume that the fit statistics of the least squares estimate obtained from the subset ($\mathscr{D}_{sub}$) is also valid for the entire set ($\mathscr{D}_{full}$) of all possible observations. According to Picard and Cook [1984], although a least squares fit of a model to the full set, $\mathscr{D}$, provides an unbiased estimator of the unknown parameters $\boldsymbol{X}_{full}$, it does not guarantee that a fitted model based on a subset of observations, $\mathscr{D}_{sub}$, will provide an unbiased estimate of $\boldsymbol{X}_{full}$. Therefore, we investigated the use of cross validation techniques for the assessment of the results. However, it was found that the prediction error obtained from the residuals of the least squares fit to the subset of observations $\mathscr{D}_{sub}$, agreed best with the true error obtained by assessing the fitted functional formulations using ray-tracing through a high resolution NWM for a dense $1° \times 1°$ grid spacing in azimuth and elevation angles ranging from $3°$ to $90°$. A complete description of the experiment

54

and results can be seen in Appendix I.

Each model will be assessed based on the residuals of the least squares fit which show the discrepancy between the observations (ray-traced slant factors) and the fitted or predictive model.

In order to obtain a prediction of the error in station height due to the discrepancies between the truth observations and the models, the rule-of-thumb suggested in MacMillan [1995] and extended to PPP by Boehm et al. [2008] is used. The error in station height ($err_{\Delta h}$) due to errors in the slant factor model ($err_{\Delta \kappa}$) is equal to:

$$err_{\Delta h} \approx 1/5 \times err_{\Delta \kappa}. \tag{4.6}$$

4.3   Results and Discussion

We begin the analysis by assessing the performance of the current state-of-the-art mapping functions for space geodetic techniques. Next the functional formulations are assessed. The symmetric functional formulations are compared to the VMF parametrization to identify any deficiencies in its realization. The asymmetric functional formulations are then assessed. An attempt is made to characterize the global patterns of tropospheric gradients. This characterization is used to suggest the short coming of current functional formulations and make recommendations for mitigating the asymmetric delay.

4.3.1   Mapping Functions

All mapping functions in use today separate the delay into the hydrostatic and non-hydrostatic component. For this analysis the separation is maintained to allow us to identify deficiencies in either component. The mapping functions assessed in this section along with several characteristics of each are summarized in Table 4.1.

The UNBVMF shares the same parametrization of the VMF1, namely the empirical coefficients *b* and *c*, but the *a* coefficient is computed using the UNB ray-tracing algorithms and the CMC-GEM model has been used in place of the ECMWF model. This will prevent differences in the atmospheric source (CMC-GEM vs ECMWF) from contaminating the results.

4.3.1.1 Hydrostatic

Table 4.2 shows the mean and standard deviation of the daily biases of the symmetric hydrostatic mapping functions with respect to the three dimensional ray-tracing for the $5°$ elevation angle. In the final row the RMS of the mean biases and the average standard deviation for each mapping function are shown. Overall, the VMF parametrization, used in both the VMF1 and UNBVMF, yields the smallest bias with respect to the three dimensional ray-tracing. A slight reduction in the bias and standard deviation is seen when the VMF parametrization is used for the UNBVMF, which shares the atmospheric source of the truth data. This does not indicate that the UNBVMF is an improvement on the VMF1, it simply means that there may be differences between the NWM produced from the different agencies.

At the $5°$ elevation angle, the NMF can introduce biases on the order of several centimeters. These biases are largest for stations in the souther hemisphere, most notably

Table 4.1: Summary of the characteristics of the state-of-the-art mapping functions evaluated in this section. The number in brackets specifies the number of coefficients in the expression. "r.t." indicates that the value is determined by ray-tracing through a NWM.

Mapping Function	Atmospheric Source	Functional Form.	Parameters
NMF	US Standard Atmosphere	Marini (3)	a,b,c (empirical)
GMF	ECMWF	Marini (3)	a,b,c (empirical)
VMF1	ECMWF	Marini (3)	a (r.t.), b,c (empirical)
UNBVMF	CMC-GEM	Marini (3)	a (r.t.), b,c (empirical)

Table 4.2: Mean bias and standard deviation of the nominal hydrostatic slant delay ($\Delta L^z = $ 2300 mm) at the 5° elevation angle and approximate error in station height for the 20 IGS stations used in the study. All units in millimeters.

| | Mean | | | | | Standard Deviation (1 σ) | | | |
Station	NMF	GMF	VMF1	UNBVMF		NMF	GMF	VMF1	UNBVMF
ALIC	-7.27	-2.81	-1.90	3.62		13.68	12.75	3.78	2.53
CAGS	19.28	6.91	3.57	3.20		28.79	28.22	4.19	3.79
CHAT	7.77	-7.00	-5.62	-4.43		22.15	17.37	3.61	3.00
HARB	-6.90	-5.44	0.06	5.72		12.39	11.56	4.16	2.85
KERG	28.32	-0.96	-2.12	-1.81		32.96	26.41	4.58	3.93
KOKB	-9.74	-8.30	-9.59	-3.93		9.68	9.79	3.12	2.22
LPGS	7.63	0.27	-1.57	1.05		17.72	16.91	3.74	2.81
MDO1	-2.56	2.32	0.91	5.80		15.17	13.03	3.90	3.04
NICO	-14.44	-13.01	-9.41	-6.87		21.36	15.97	4.13	3.50
NTUS	-11.00	-5.70	-7.07	0.28		5.84	6.35	4.46	3.00
NYAL	13.75	3.46	5.67	0.63		24.33	23.92	4.75	4.39
OHI2	42.51	3.38	3.28	0.83		32.49	24.80	5.21	3.96
PDEL	-10.58	-10.67	-5.81	-2.71		14.76	13.66	3.71	2.77
POL2	9.27	8.89	6.00	9.17		22.80	19.62	4.02	3.12
SCUB	-12.06	-8.12	-8.78	-4.68		6.51	6.93	4.22	2.71
SEY1	-11.59	-8.61	-7.19	0.41		5.26	5.92	4.35	2.68
THTI	-9.82	-11.06	-11.81	-5.55		7.63	6.78	4.08	2.85
WTZR	-2.59	-1.69	2.45	3.26		22.47	21.24	3.80	3.32
YELL	8.02	4.53	5.63	2.55		27.46	28.12	3.81	3.45
YSSK	27.74	-4.55	-0.05	1.09		29.61	22.36	4.18	4.02
RMS	16.18	6.83	5.94	4.12	Avg.	18.65	16.59	4.09	3.20

OHI2, which has a bias of 42.5 mm.

The GMF performs very well for a climatology based mapping function. The drawback of the GMF is that the standard deviation is more than two times as large as the VMF1. This is a result of the use of mean atmospheric conditions which result in the GMF not being capable of modeling the day-to-day variations of the slant factors. However, its use will not introduce a significant bias in the station height, which overall has an RMS of 1.37 mm as compared to 1.19 for the VMF1 and 0.82 for UNBVMF. Therefore, it is recommended as an acceptable backup when the VMF1 is not available.
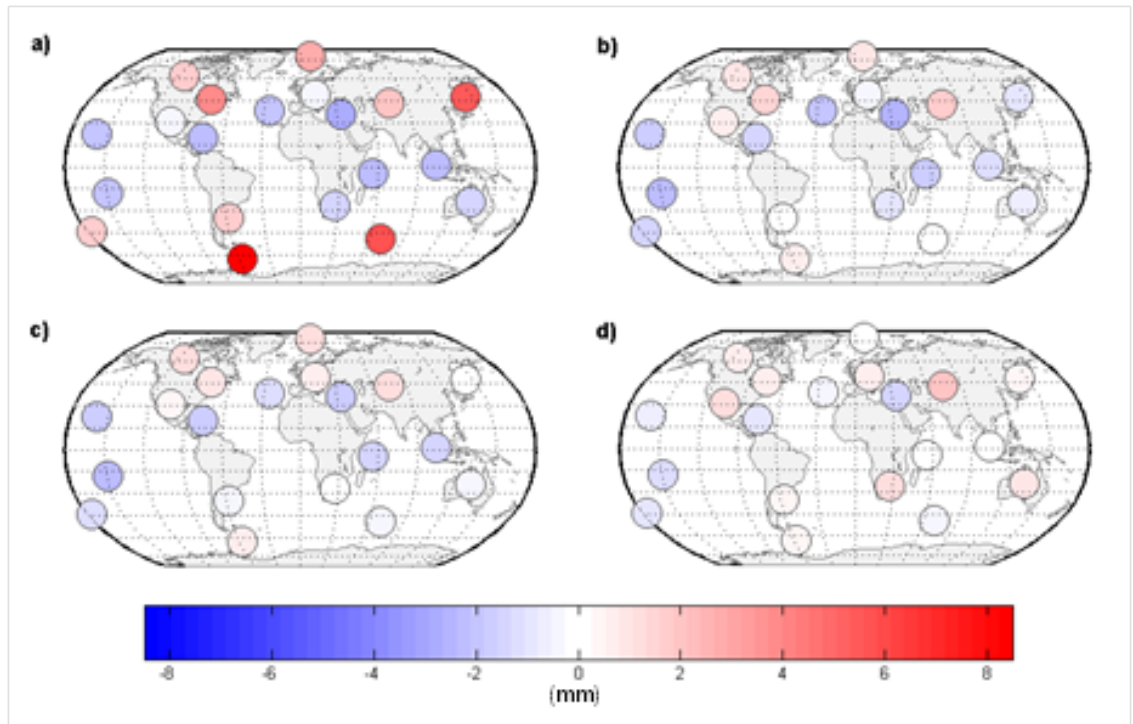
Figure 4.2: Error in station height (in mm) due to the hydrostatic component, for the year 2008. Fig. a) ray-trace minus NMF; Fig b) ray-trace minus GMF; Fig c) ray-trace minus VMF1; Fig d) ray-trace minus UNBVMF.

Figure 4.2 shows the error in station height due to the hydrostatic mapping functions using the rule-of-thumb of eq. (4.6). The largest errors occur when using the NMF, for stations in the southern hemisphere where the error can reach nearly 1 cm. Both the GMF and VMF perform very well, with the largest errors of approximately -2 mm occurring near the equator. A systematic dependency of the station error can be seen for all three mapping functions with respect to latitude, resulting in a positive error at the poles and a negative error occurring at the equator.

The cause of this latitude dependent bias, at least for the GMF and VMF1 mapping functions, is believed to be due to the simplification of the shape of the earth to a sphere of constant radius when performing the ray-tracing through the ECMWF analyses. This theory was tested by modifying the UNB ray-tracing algorithms to use a sphere of constant

58

radius rather than the gaussian mean radius which is implemented for ray-tracing through a spherically symmetric atmosphere. For the three dimensional ray-tracing, cartesian coordinates are used, therefore it is not necessary to specify a radius of the earth. Figure 4.3 shows the mean bias of the nominal slant delay at the 5° elevation angle versus latitude for the VMF1 and for UNBVMF using both the gaussian mean curvature and a constant radius. The solid lines are the result of a least squares fit of the biases to a sinusoid of the form $a \cdot \cos(2\phi - \pi) + c$. Both the VMF1 and the UNBVMF using a constant radius exhibit a similar trend in the bias with respect to latitude. The UNBVMF using the gaussian mean curvature also exhibits a small bias, but not to the same extent as the VMF1. For more details on the impact of the radius of the earth on ray-tracing, please see Appendix IV.
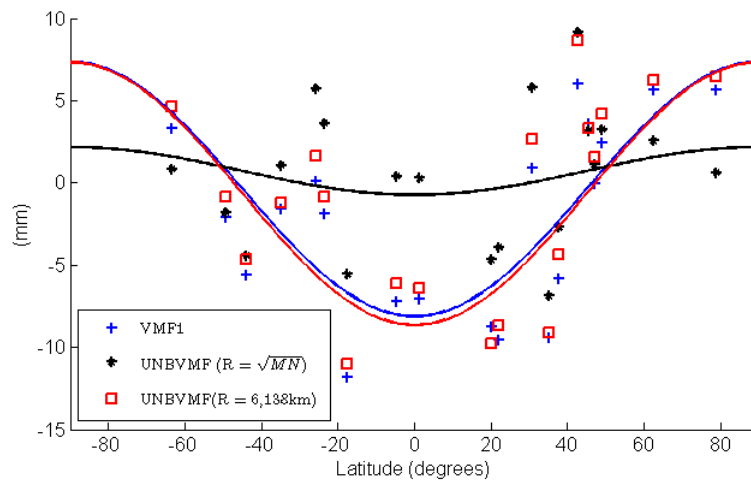
Figure 4.3: Error in station height versus latitude of the hydrostatic UNBVMF with a radius equal to the gaussian mean curvature and the UNBVMF with a radius equal to a constant and the VMF1 which also uses a constant radius. Units of millimeters.

The RMS scatter of the differences between the three dimensional ray-tracing (discrepancies) and the mapping functions will effect the repeatability of the station coordinates. Figure 4.4 shows the RMS of the discrepancies at the 5° elevation angle with respect to latitude. The cause of the latitude dependency is due to the asymmetry of the hydrostatic

delay which is on average larger at the mid-latitudes than at equatorial sites due to the larger temperature gradients existing at mid latitudes. . This is caused by the relatively large temperature gradients which exist at the mid- to high latitudes. Near the equator, the hydrostatic delay is more symmetric than at the poles as the temperature gradients are less extreme. Therefore the symmetric mapping functions are a better representation of the ray-traced slant factors near the equator than they are at mid- to high- latitudes. More discussion on the average tropospheric gradients is presented in section 4.3.3.1.
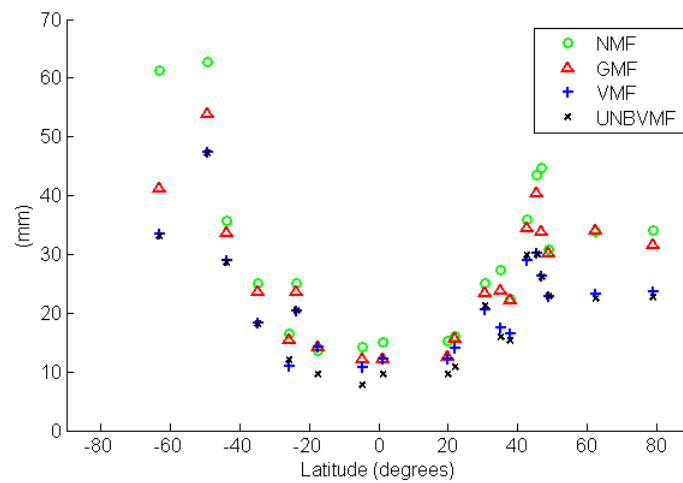
Figure 4.4: RMS of the discrepancies between the hydrostatic mapping functions and the three dimensional ray-tracing with respect to latitude for the 5° elevation angle. Units of millimeters.

Figure 4.5 shows the mean RMS of the differences between the mapping function and the three dimensional ray-tracing for all stations and the remaining elevation angles. The black bars indicate the spread of the mean RMS. For elevation angles above 14° the choice of mapping function is not critical as the error bars substantially overlap each other. Below 10° the mapping functions which are derived directly from the NWM on an epoch-by-epoch basis show a significant advantage over the climatology based mapping functions. For 5° elevation angle and below, the UNBVMF (ie., parametrization of the VMF, realized

60

using the same NWM as the truth data) shows a statistically meaningful advantage over the other mapping functions. However, that is not to say that the UNBVMF is an improvement over the VMF1. It simply implies that the choice of NWM can lead to significant differences in the realization of a mapping function. Therefore identifying which NWM are optimal is an important aspect of troposphere mapping function development.
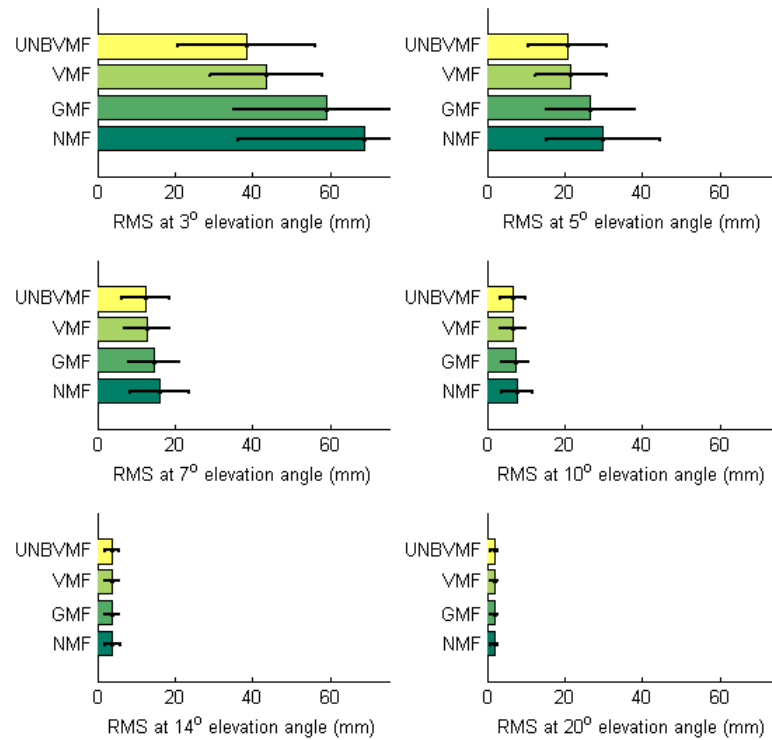
Figure 4.5: Mean RMS and standard deviation of the hydrostatic mapping function errors for elevation angles 3°, 5°, 7°, 10°, 14° and 20°. Units of millimeters.

4.3.1.2 Non-hydrostatic

Table 4.3 shows the mean and standard deviation of the daily biases of the symmetric non-hydrostatic mapping functions with respect to the three dimensional ray-tracing for the 5°

elevation angle. The RMS of the mean biases and the mean of the standard deviation are shown in the final row of the table.

Table 4.3: Mean bias, standard deviation of the nominal non-hydrostatic slant delay ($\Delta L^z = 220$ mm) at the $5°$ elevation angle and approximate error in station height for the 20 IGS stations used in the study. All units in millimeters.

| Station | Mean | | | | | Standard Deviation (1 σ) | | | |
	NMF	GMF	VMF	UNBVMF		NMF	GMF	VMF	UNBVMF
ALIC	5.49	0.83	-0.37	1.53		25.62	26.17	16.53	14.75
CAGS	7.84	10.23	2.25	3.36		30.86	30.85	24.91	23.43
CHAT	17.48	6.05	3.46	3.28		26.29	25.97	21.00	19.21
HARB	23.20	3.97	1.30	0.33		25.45	23.52	20.59	18.20
KERG	15.96	13.24	6.27	6.09		31.96	31.54	24.13	22.92
KOKB	19.90	18.73	-2.71	-0.79		23.77	24.35	19.91	18.11
LPGS	12.00	6.36	3.92	3.17		22.97	22.94	17.91	16.21
MDO1	17.93	10.90	0.93	-0.48		25.79	25.49	20.95	17.75
NICO	9.08	-0.27	-2.85	-1.27		21.99	21.99	17.05	15.12
NTUS	-18.53	0.90	-1.77	-1.39		11.80	11.93	9.42	8.57
NYAL	22.96	4.40	7.51	7.30		34.39	33.56	30.90	29.91
OHI2	16.59	6.89	2.36	2.10		21.83	21.74	16.44	15.15
PDEL	8.04	1.88	0.66	0.86		27.43	27.10	22.83	20.92
POL2	15.70	5.28	-3.72	-3.12		28.24	28.29	27.95	24.05
SCUB	-0.91	-1.08	-2.51	-1.73		23.57	22.63	20.39	17.07
SEY1	1.96	5.84	-1.18	-0.06		15.73	15.83	11.96	9.85
THTI	1.18	2.27	-1.08	-0.91		18.92	17.54	14.13	12.66
WTZR	14.63	7.95	0.87	0.22		26.48	26.35	21.48	19.81
YELL	8.18	-2.95	1.69	2.92		26.39	26.22	22.51	21.24
YSSK	4.08	-2.12	-5.41	-1.57		21.84	21.35	16.10	15.09
RMS	13.95	7.28	3.25	2.82	Avg.	24.57	24.27	19.85	18.00

Overall, the VMF1 and UNBVMF mapping functions showed excellent agreement with the three dimensional ray-tracing, while the GMF had several stations which had biases larger than 10 mm. The NMF performed the worst, with biases larger than 20 mm for several stations and in almost all cases under predicted the slant factor when compared to the three dimensional ray-tracing.

Even using the state-of-the-art NWM, the non-hydrostatic delay is very difficult to predict well as it is dependent on small fluctuations of water vapor in the atmosphere. For this reason the empirical values of the non-hydrostatic mapping functions are not as well determined as the empirical values of the hydrostatic mapping functions. Therefore the improvement in the standard deviation of the mapping functions which rely on the NWM directly, namely the VMF and UNBVMF, do not see a large improvement as compared to the mapping functions based on a climatology.

The error in station height due to errors in the mapping function are shown in Figure 4.6. Both the NMF and the GMF produce a small positive bias in the height solution. However, in the case of the GMF, the bias is still less than 2 mm for all but two stations, KOKB and MDO1. Keep in mind that we use a nominal zenith delay of 220 mm which may not be true for all areas of the globe, although it allows for a more consistent comparison of the mapping functions themselves. The mean bias in station height for the VMF1 and UNBVMF is less than 1 mm which indicates that they are fully compatible with the three dimensional ray-traced slant factors.

The bias, in the case of the NMF and the GMF, was determined to be a function of station height. Figure 4.7 shows the mean bias versus station hight and it can be seen that for the VMF1 and the UNBVMF, only a slight negative trend exists. For the NMF and to a lessor extent the GMF, a positive slope exists. As the VMF1 and UNBVMF are site specific there is no need for a correction for station height. Unlike the hydrostatic mapping functions, the non-hydrostatic NMF and GMF do not employ a height correction as the water vapor is not in hydrostatic equilibrium and therefore the distribution of the water vapor with respect to station height is difficult to predict [Niell, 1996]. This lack of a height correction could be a cause of this linear trend. However, as the magnitude of the non-hydrostatic zenith delay is about 10 times smaller than the hydrostatic zenith delay, this is not of much concern.
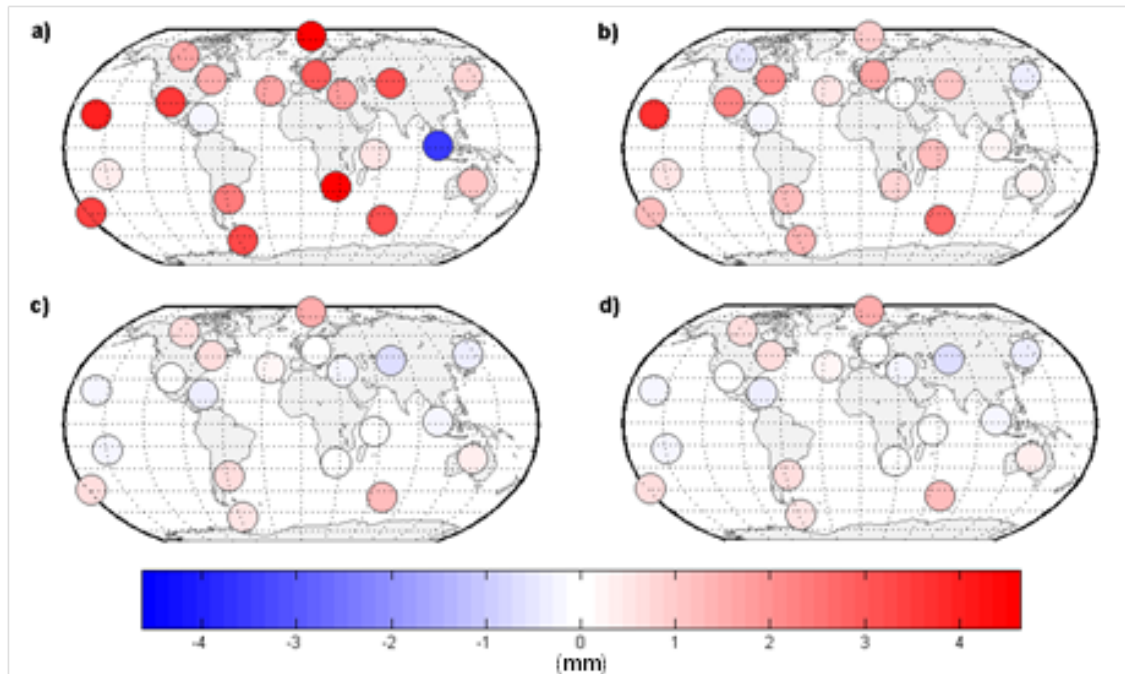
Figure 4.6: Error in station height (in mm) due to the non-hydrostatic component, for the year 2008. Fig. a) ray-trace minus NMF; Fig b) ray-trace minus GMF; Fig c) ray-trace minus VMF1; Fig d) ray-trace minus UNBVMF.
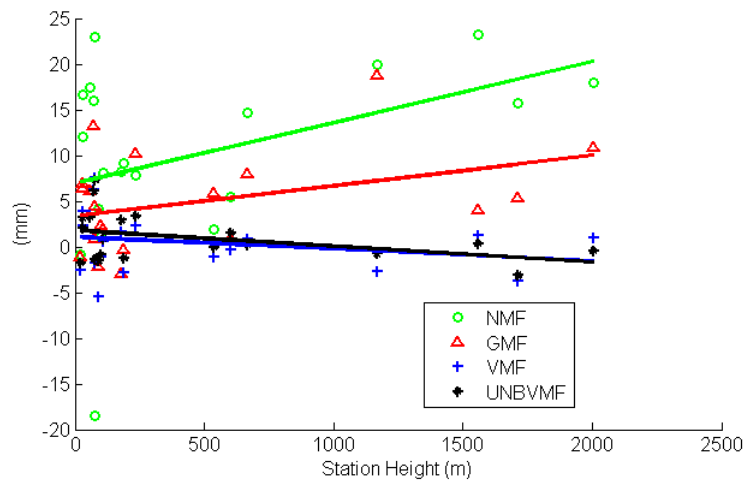
Figure 4.7: Mean bias of the non-hydrostatic mapping functions versus height. The solid lines were fitted to the mean bias using a first order polynomial.

The RMS of the non-hydrostatic mapping function discrepancies with respect to the three dimensional ray-tracing, shown in Figure 4.8, does not exhibit as clear of a latitude dependence as the hydrostatic mapping functions. It is important to keep in mind that for all stations, a nominal non-hydrostatic zenith delay of 0.220 m was used which does not accurately reflect the presence of water vapor in the atmosphere with respect to latitude. So although in these plots the RMS of the non-hydrostatic delay at mid- to high-latitudes is larger than at the equator, in reality the non-hydrostatic zenith delay would typically be smaller in these regions which would in turn produce smaller variability at the mid- to high- latitudes. This phenomenon was shown in Ghoddousi-Fard et al. [2009a] where the magnitude of the non-hydrostatic zenith delay at the equator can be more than four times the magnitude near the poles.
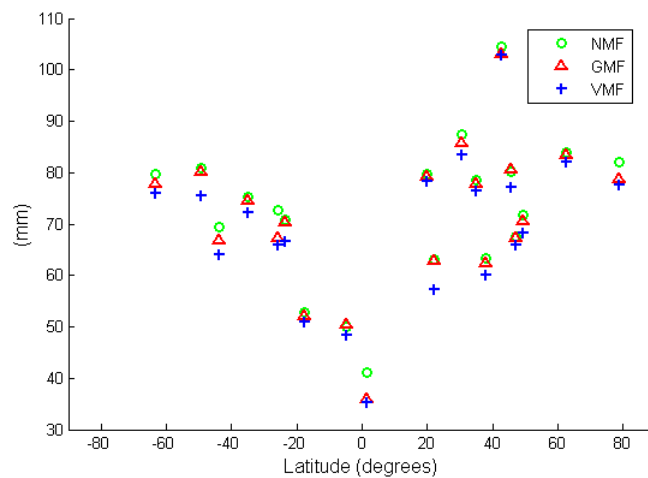
Figure 4.8: RMS of the discrepancies between the non-hydrostatic mapping functions and the three dimensional ray-tracing with respect to latitude for the 5° elevation angle. Units of millimeters.

Figure 4.9 shows the mean RMS of the mapping function error over all stations for the remaining elevation angles. The mean RMS of the non-hydrostatic mapping functions is extremely large for low elevation angles. In fact it is larger than the hydrostatic vari-

65

ability even though the magnitude of the non-hydrostatic delay is much smaller than the hydrostatic.

Although the RMS is smaller for the VMF1 and UNBVMF, the error bars of each mapping function largely overlap each other. Therefore, although the VMF1 parametrization can be used with only a sub mm bias in the station height, the repeatability could still be improved although this is limited by the accuracy of the NWM in modeling both the spatial and temporal resolution of the water vapor in the atmosphere.
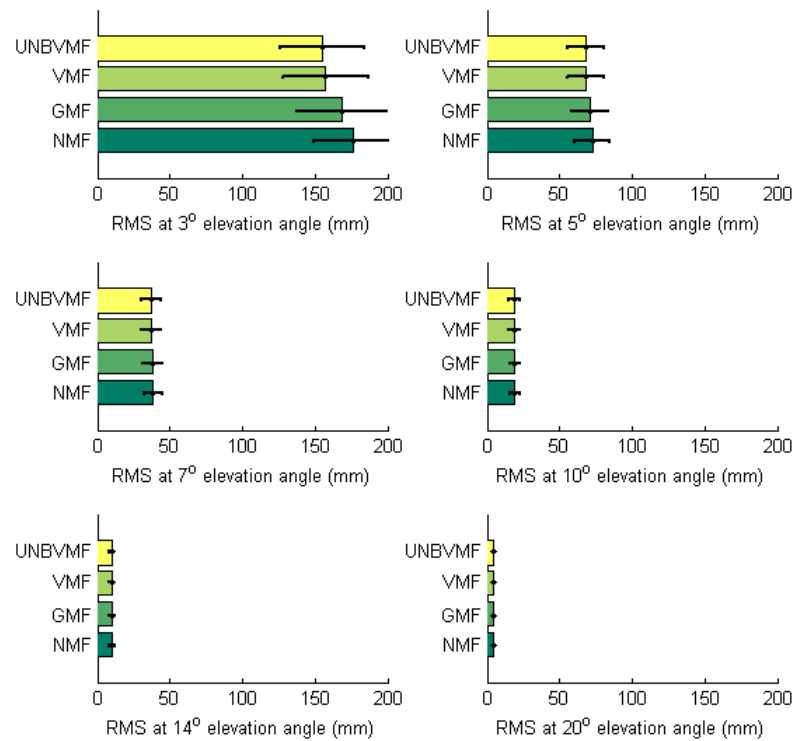
Figure 4.9: Mean RMS and standard deviation of the non-hydrostatic mapping function errors for elevation angles $3°$, $5°$, $7°$, $10°$, $14°$ and $20°$. Units of millimeters.

4.3.2 Functional Formulations, Symmetric

We now assess the symmetric functional formulations. These formulations are fitted to hydrostatic and non-hydrostatic slant factors. The VMF parametrization has also been included in this comparison. This will help identify any deficiencies in the VMF parametrization which could be improved upon in the future. To ensure consistency, we have chosen to use the *UNBVMF* as it has the same atmospheric source as the other symmetric formulations. This will allow for a direct comparison of the parametrization rather than a realization.

As these functional formulations are only meant to model the elevation angle dependence of the slant factors we are mainly interested in identifying any biases with respect to elevation angle. This would indicate a deficiency in the functional formulation's ability of modeling the elevation angle dependence of the slant factors and therefore indicate that the formulations are not suitable for modern mapping functions. A summary of the functional formulations is given in Table 4.4.

4.3.2.1 Hydrostatic

Figure 4.10 shows the mean and standard deviation of the daily biases of the the symmetric functional formulations with respect to the hydrostatic slant factors determined from ray-tracing. With the exception of the *Davis* formulation all functional formulations agree with the three dimensional slant factors to less than 1 mm above $7°$ elevation angle. As

Table 4.4: Summary of the symmetric functional formulations evaluated in this section.

Formulation	Reference	Unknown Coefficients
*Marini*3	[Marini, 1972]	a,b,c
*Marini*4	[Marini, 1972]	a,b,c,d
Davis	[Davis et al., 1985]	a,b,c
UNSW	[Yan and Ping, 1995]	a,b,c,d
UNBVMF	[Boehm et al., 2006b]	a
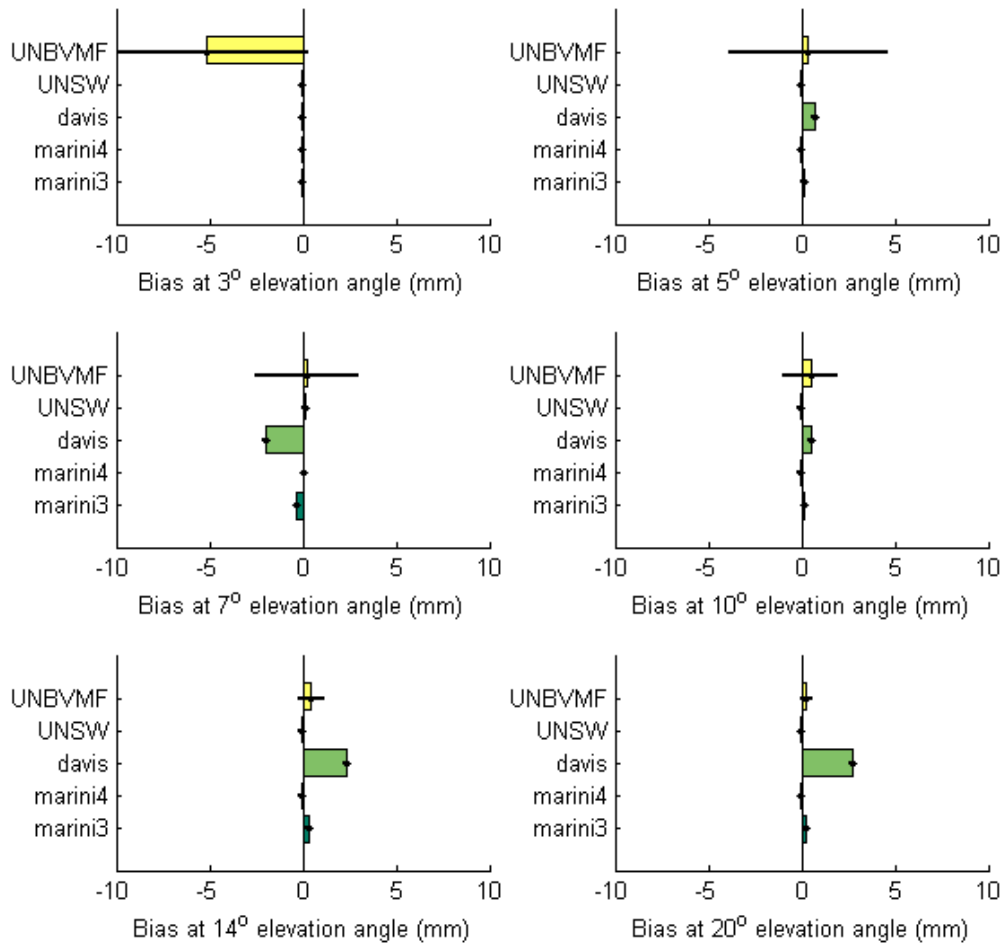
Figure 4.10: Mean and standard deviation of the functional formulations with respect to the hydrostatic slant factors determined from ray-tracing for elevation angles 3°, 5°, 7°, 10°, 14° and 20°. Units of millimeters.

noted in Davis et al. [1985] the *Davis* functional formulation has the largest bias between 14° and 70° elevation angle. This is caused by the $\tan(\varepsilon)$ term, as it does not approach $\sin(\varepsilon)$ quickly enough for these elevation angles.

As no weights were assigned to the ray-traced slant factors in the fitting process, the results are somewhat dependent on the lowest observed elevation angle, which in this case

was 3°. Both of the four coefficient function formulations (Marini 4 and UNSW) showed a small improvement over the *Marini*3 coefficient at the 1σ level. Unlike the *UNSW* formulation, the *Marini*4 coefficient expression does not contain any external parameters therefore it would be preferred. The benefit of the external parameter in the *UNSW* may not be significant and could most likely be removed. In practice, the improvement seen with the four coefficient expressions is not critical as the uncertainty in the space geodetic observations and the uncertainty in the slant factors themselves at low elevation angles is much larger than the improvement in the bias seen with the four coefficient functional formulations.

The results of the VMF parametrization (*UNBVMF*) shows that it does not introduce a significant bias even down to the 5° elevation angle, however at 3° there is a bias of almost 5 mm. The results indicate that by estimating all three coefficients from the ray-traced slant factors rather than relying on the empirical parameters (*b* and *c*) it may be possible to improve upon the VMF parametrization. This would of course come with the trade off of increased processing requirements and could possibly only introduce a small benefit in the position domain.

Figure 4.11 shows the daily mean of the five functional formulations for station KERG. In the case of *UNBVMF*, the *a* coefficient alone is not able to model the day-to-day variability to the same degree as the other functional formulations, therefore spurious signals are introduced into the time series. In the case of the other formulations, as all coefficients are estimated each day there is essentially no variability throughout the year. Once again, we can see a bias which occurs for the *Davis* formulation while the *Marini*3, *Marini*4 and *UNSW* all overlap with a mean of less than 0.5 mm
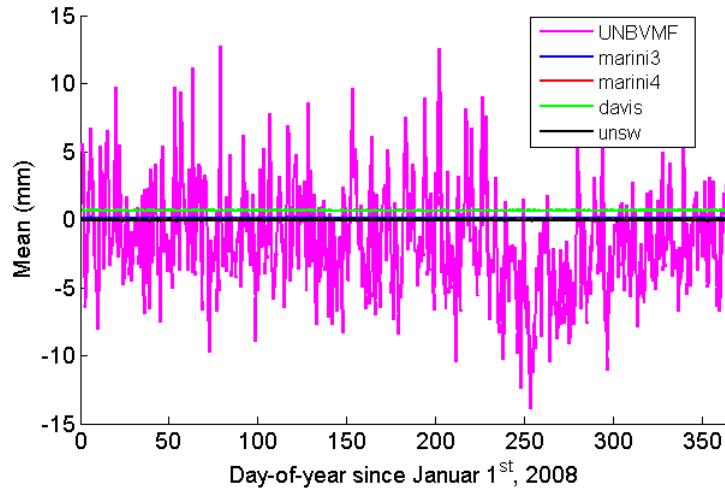
Figure 4.11: Example of the variation of daily mean bias at the 5° degree elevation angle for the functional formulations fitted to the hydrostatic slant factors for station HARB, for the year 2008. Units of millimeters.

4.3.2.2 Non-hydrostatic

Figure 4.12 shows the mean and standard deviation of the daily biases of the the symmetric functional formulations with respect to the non-hydrostatic slant factors determined from ray-tracing. Notice that the x-axis scaling for the 3° elevation angle is twice as large as the other x axes. The functional formulations which estimate all coefficients produce insignificant biases with respect to the three dimensional ray-tracing. In this case the uncertainty in the functional formulations make it difficult to say which functional formulation actually performs better, although the *Davis* formulation has the largest biases at the 14° and 20° elevation angles which does appear to be statistically significant.

The VMF parametrization, realized here as $UNBVMF$, can be used down to the 5° elevation angle before the bias reaches 1 mm. As was the case for the hydrostatic functional formulation, estimating all three coefficients was shown to reduce the day-to-day variability of the bias. This variability is shown in the daily time series for station HARB for the year 2008 in Figure 4.13.

70
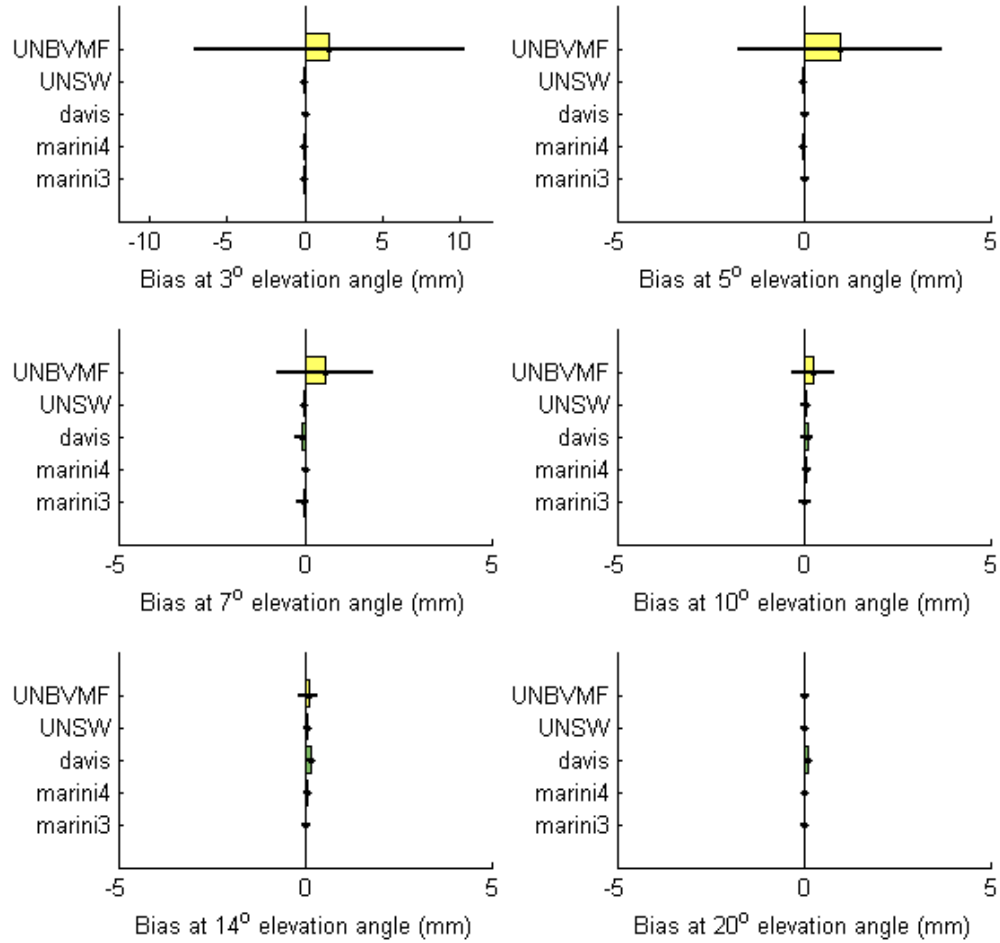
Figure 4.12: Mean and standard deviation of the functional formulations with respect to the non-hydrostatic slant factors determined from ray-tracing for elevation angles 3°, 5°, 7°, 10°, 14° and 20°. Units of millimeters.

4.3.3 Functional Formulations, Asymmetric

The functional formulations assessed in this section include various linear horizontal gradient models, which have different expressions for the gradient mapping function, a second order linear gradient model and low order spherical harmonic expressions for describing the asymmetry of the slant factors. Table 4.5 summarizes the formulations and the unknown coefficients that are estimated by the least squares process. In brackets, the
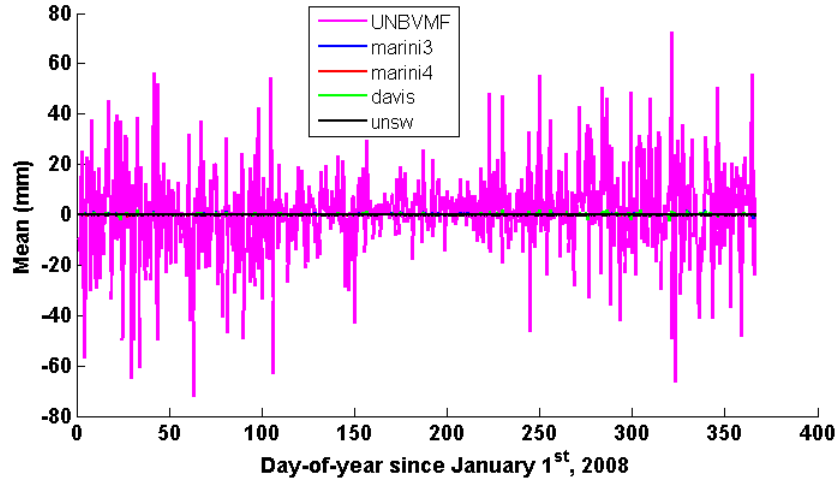
Figure 4.13: Example of the variation of daily mean bias at the 5° degree elevation angle for the functional formulations fitted to the non-hydrostatic slant factors for station HARB, for the year 2008. Units of millimeters.

"hyd", "non-hyd" and "tot" represent differences in the formulation which are dependent on which component of the delay we are dealing with. In the case of Chen & Herring formulation, we have four different versions which are distinguished by how the "C" coefficient in the gradient mapping function is obtained. In the case of the *hyd*, *nonhyd* and *Tot*, we use predefined values of 0.0031, 0.001 and 0.0032 respectively, while for *Est*, the "C" coefficient is estimated as an additional parameter in the least squares adjustment.

For the *MeindlNMF* formulation, the partial derivative of the Niell Mapping Function is used to model the elevation angle dependence of the gradients. The hydrostatic NMF is used for the hydrostatic component (*MeindlNMFhyd*), while the non-hydrostatic NMF is used for the non-hydrostatic and total components (*MeindlNMFnon − hyd*). We have included the estimation of total gradients to simulate what occurs for positioning purposes, as it is not possible to separate the contribution of the hydrostatic and non-hydrostatic gradients.

The assessment will be performed on the ability of the functional formulations to

72

Table 4.5: Summary of the characteristics of the asymmetric functional formulations evaluated in this section.

Functional Formulation	# of Unknowns	Coefficients
Linear Horizontal Gradient:		
Chen & Herring (hyd/non-hyd/Tot)	5	a,b,c,G_N,G_E
Chen & Herring (Est)	6	a,b,c,C,G_N,G_E
Davis	5	a,b,c, G_N,G_E
MacMillan	5	a,b,c, G_N,G_E
MeindlNMF (hyd/non-hyd/Tot)	5	a,b,c, G_N,G_E
2nd Order Polynomial:		
Seko	8	a,b,c, G_N,G_E, G_{NN}, G_{EE}, G_{NE}
Spherical Harmonics:		
SH11 n=1 m=1	6	a,b,c, a_{10}, a_{11}, b_{11}
SH21 n=2 m=1	9	a,b,c, a_{10}, a_{11}, b_{11}, a_{20}, a_{21}, b_{21}

model the asymmetry of the three dimensional ray-traced slant factors. This will be characterized by the RMS of the residuals from the least squares fit of the functional formulation to the ray-traced slant factors.

The estimated coefficients will also be assessed when possible. As the G_N and G_E terms of the linear gradient functional formulations are popular atmospheric parameters we will consider the effect of the formulations on these values. Of additional interest is the possibility of defining an improved estimation of the C coefficient in the Chen & Herring gradient mapping function as was discussed in Chapter 3

4.3.3.1 Hydrostatic

We begin by first considering only the linear horizontal gradient functional formulations. Figure 4.14 shows the mean RMS of the residuals, and corresponding spread, of all stations for the linear horizontal gradient function formulations for the year 2008. At the $3°$ elevation angle all linear horizontal gradient formulations perform approximately the same with an RMS of about 10 mm. This is a large improvement from the symmetric functional formulations and mapping functions which had an RMS of more than 50 mm
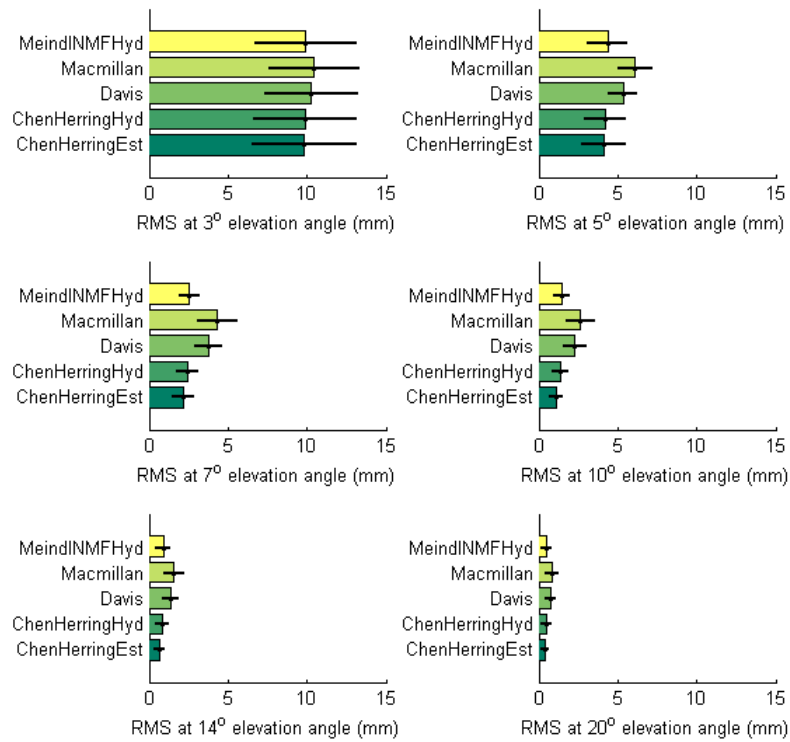
Figure 4.14: Mean RMS and standard deviation of the hydrostatic functional formulation errors with respect to the three dimensional ray-traced slant factors multiplied by a nominal 2300 mm, for elevation angles $3°$, $5°$, $7°$, $10°$, $14°$ and $20°$. Units of millimeters.

at this elevation angle.

As the elevation angle increases, the *ChenHerringEst* which included the estimation of the *C* coefficient in the gradient mapping function performs slightly better than the other functional formulations. The estimation of the *C* coefficient does not seem to provide a statistically significant advantage (at the 1σ level) over the constant value determined in Chen and Herring [1997]. The *MeindlNMFHyd* formulation also performed well. The *MacMillan* formulation which replaces the apparent elevation angle (of the *Davis* formulation) with the geometric elevation angle led to a slightly worse RMS. This would imply that simply replacing the apparent elevation angle with the geometric elevation angle leads

to a slight decrease in performance.
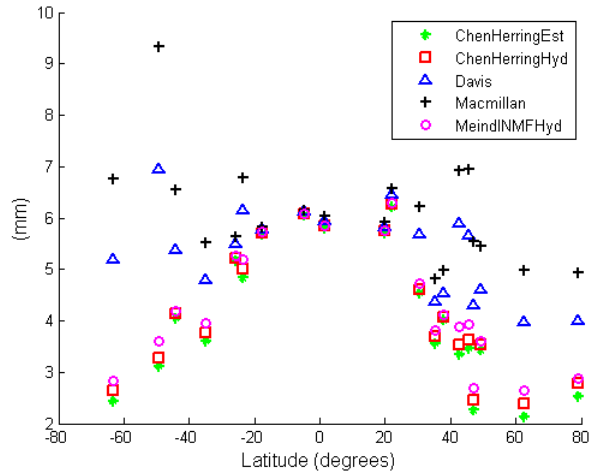
Figure 4.15: RMS of the discrepancies between the hydrostatic asymmetric linear horizontal gradient functional formulations and the three dimensional ray-tracing with respect to latitude. Units of millimeters.

Figure 4.15 shows the mean daily RMS of the residuals for the linear horizontal gradient functional formulations for each station versus latitude at the $5°$ elevation angle. The *Chen&Herring* functional formulations along with the *MeindlNMFhyd* formulation, all display a latitude dependence with a minimum RMS at mid- to high- latitudes, and a maximum RMS in the equatorial region. The *MacMillan* and the *Davis* functional formulations performs somewhat more erradic, with some stations showing an improvement in the RMS, in particular for high northern latitude stations, while in the southern hemisphere the RMS tends to increase.

Next, we discuss the functional formulations based on spherical harmonics and the 2nd order linear gradient formulation. Figure 4.16 shows the mean RMS of the residuals, and corresponding spread, of the remaining functional formulations. At low elevation angles the 2nd order polynomial (Seko) reduces the RMS by almost a factor of three when compared to the other functional formulations. At higher elevation angles the improvement
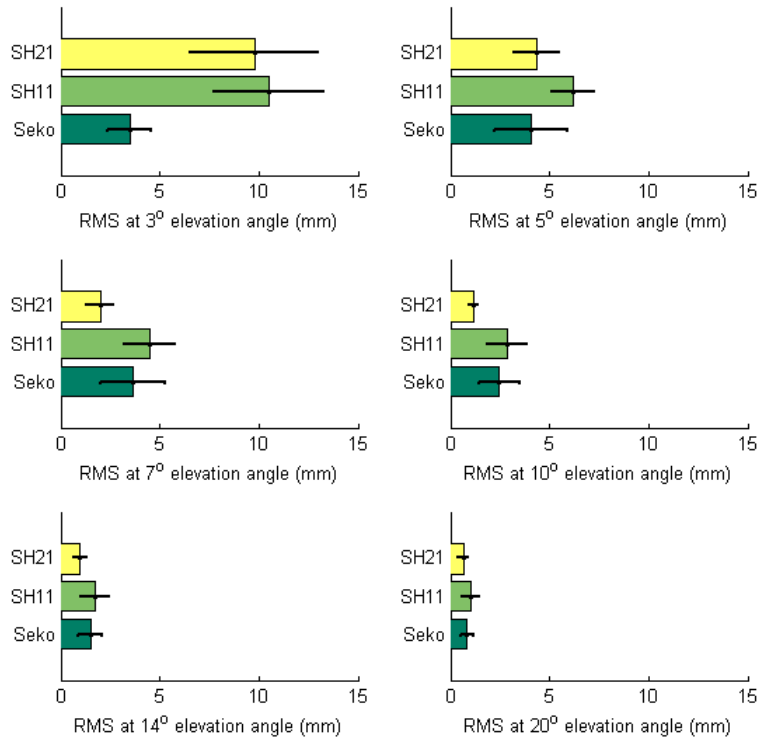
Figure 4.16: Mean RMS and standard deviation of the hydrostatic 2nd order polynomial and spherical harmonic functional formulations errors with respect to the three dimensional ray-traced slant factors multiplied by a nominal 2300 mm, for elevation angles $3°$, $5°$, $7°$, $10°$, $14°$ and $20°$.

is not as large as the asymmetric delay in general becomes less. The spherical harmonics of degree one (*SH*11 and *SH*21) perform similar to the linear gradient models, although *SH*21 does have an improvement in the RMS at the $7°$ elevation angle. Like the linear horizontal gradient formulations, the spherical harmonics of degree one are only able to model a single maxima and minima but also have elevation dependent terms that are estimated in the least squares adjustment. From these results it appears that these elevation angle dependent terms do not make a large improvement in the overall fit.

Figure 4.17 shows the RMS of the remaining three functional formulations with re-
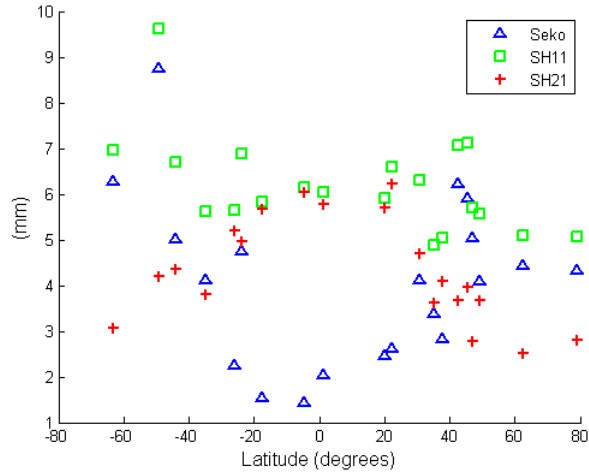
Figure 4.17: RMS of the discrepancies between the hydrostatic asymmetric 2nd order polynomial and spherical harmonic functional formulations and the three dimensional ray-tracing with respect to latitude. Units of millimeters.

spect to latitude. At equatorial latitudes, all three formulations perform better than the linear horizontal gradient formulations shown in Figure 4.15. The *Seko* formulation performs very well for mid-latitude stations although as we move towards the poles, the RMS grows, surpassing the RMS of the linear horizontal gradient functional formulations. The *SH*11 functional formulation performs well at mid latitudes, but, the RMS grows as it moves towards the poles and gives similar results to the *MacMillan* and *Davis* functional formulation. These three formulations all rely on the Marini formulation for modeling the elevation dependence of the slant factors. This is also true for the *SH*21 but the inclusion of two elevation angle dependent terms must aid in the fitting. The *MeindlNMFHyd* formulation uses the partial derivative of the Marini expression which seems to better approximate how the gradients increase with elevation angle.

Unfortunately, the inclusion of more unknowns may not be practical for geodetic processing software as it reduces the degrees of freedom of the adjustment, although Pany et al. [2010] showed that it is possible. Alternatively these higher order expressions could

be used as a method to compress the ray-traced slant factors in a closed form and thereby be a convenient method for distributing them to end users.

The results which are shown in Figures 4.15 and 4.17 can be explained by studying the geogrpahic variation of the asymmetric hydrostatic delay on a global level. Up to this point, due to constraints on processing capabilities, it was very difficult to develop a global ray-tracing campaign of a significant length, in this case one year, from which conclusions about the nature of the tropospheric gradient could be derived. Chen and Herring [1997] did perform a similar experiment, although ray-tracing was only performed at eight azimuth angles.

Figure 4.18 shows mean asymmetry of the hydrostatic slant factor multiplied by a nominal zenith delay of 230.0 cm versus azimuth at the $3°$ elevation angle for all stations over the year 2008. The mean symmetric delay has been removed in order to show the variation of the delay in terms of azimuth more clearly. In the bottom right corner of the plot, a legend which describes the axes and symbols is shown. For each box plotted in the figure, the x axis is the azimuth, while the y axis represents the asymmetric nominal hydrostatic slant delay. In the top left corner of each box the station name is shown. The solid blue line represents the mean annual asymmetry at the $3°$ elevation angle while the grey error bars show the standard deviation every $10°$ in azimuth.

In the figure, three distinct zones of hydrostatic gradient structures can be seen: a northern latitude zone; equatorial zone; and a southern latitude zone. In the northern and southern latitude zones, the asymmetric hydrostatic delay is characterized by a single maximum and single minimum. In the northern zone, the maximum occurs at an azimuth of approximately $180°$ while in the southern zone the azimuth of the maximum is approximately $0°$. These gradients of the mid- to high- latitude zones have been well understood and are due to the relatively stable temperature gradient that exists between the poles and the equator [Chen and Herring, 1997]. The amplitude of the mean asymmetry can reach

up to 22 cm peak-to-peak at the three degree elevation angle.

In the equatorial zone, it is possible to see a relatively stable trend of two maxima and two minima. The maxima occur at approximately $90°$ and $270°$ while the minima occur at $0°$ and $180°$. This asymmetry is due to the temperature gradients which exist in the north and south direction but which do not exist in the east and west direction for stations near the equator. Thus, the largest delay occurs for observations arriving parallel to the equator, while the shortest delay occurs for observations arriving perpendicular to the equator. The peak-to-peak amplitude of the mean asymmetry at these sites is about 5 cm at the three degree elevation angle.

Now that we understand the nature of the hydrostatic gradients it is possible to make sense of the latitude dependence of the RMS for the functional formulations shown in Figures 4.15 and 4.17. With respect to azimuth, the linear horizontal gradient functional formulations and the spherical harmonics of degree one, allow for one minimum and one maximum to be modeled with respect to azimuth. For stations located at mid- to high-latitudes this is ideal, as it agrees with the hydrostatic gradients seen in Figure 4.18 for those regions which exhibit a single maximum and single minimum. On the other hand, equatorial stations exhibit a strong bi-modal signal which cannot be modeled well by these expressions. For these stations the *Seko* functional formulation which can model two maxima and two minima in the azimuth component performs extremely well. But as we move away from the equator, the *Seko* formulation begins to perform worse since the the formulation is no longer suited to model the gradient structure at these mid- to high-latitudes.

The Chen & Herring functional formulation performed the best out the linear horizontal gradient category. The C coefficient in eq. (3.17) was originally determined by ray-tracing over 10 elevation angles and eight azimuths through the NCEP atmospheric data with a grid spacing of $2.5° \times 2.5°$ and only 7 vertical layers [Chen and Herring, 1997].

Figure 4.18: Mean asymmetry of the hydrostatic slant factors multiplied by a nominal zenith delay of 230.0 cm at the 3° elevation angle with respect to azimuth, over the year 2008, for all 20 IGS stations.

80

There is potential to improve the estimate of this coefficient as the CMC-GEM model has 21 layers and a $0.6° \times 0.6°$ grid spacing.

In the experiment above, a mean value of C was determined for each station over the whole of 2008. The C value for each station and its standard deviation were used to determine a weighted mean value which was equal to 0.0037 ± 0.0005 as compared to the value of 0.0031 obtained in Chen and Herring [1997]. A slight latitude dependence of the coefficient was seen and is shown in Figure 4.19. The variation can be well approximated using an expression based on $\cos(2\phi)$. However, due to the uncertainty, a fixed value of "C" may not improve positioning repeatability to a significant degree.

Figure 4.19: Mean values and standard deviations (1σ) of the hydrostatic C coefficient for each station versus latitude.

4.3.3.2 Non-hydrostatic

Figure 4.20 shows the mean RMS of the residuals, and the respective spread, for the various linear horizontal gradient functional formulations for the non-hydrostatic component over the year 2008. The magnitude of the RMS of the non-hydrostatic residuals is close to three times larger than the hydrostatic component and the standard deviations are increased as well. This implies that the linear horizontal gradients are not able to represent

the asymmetry of the non-hydrostatic slant factors as well as the hydrostatic component.
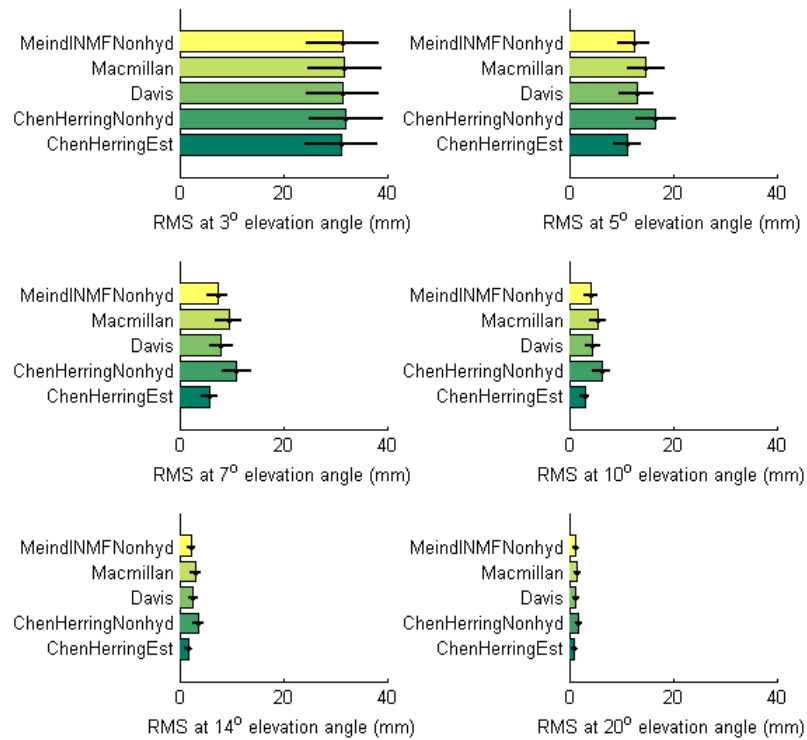
Figure 4.20: Mean RMS and standard deviation of the non-hydrostatic linear horizontal gradient functional formulations errors with respect to the three dimensional ray-traced slant factors multiplied by a nominal 220 mm, for elevation angles 3°, 5°, 7°, 10°, 14° and 20°.

The *ChenHerringEst* formulation which estimates the C coefficient has the smallest RMS of the group at all elevation angles. The *ChenHerringNonhyd* which uses $C =$ 0.001 performs 50% worse then when the "C" coefficient is estimated. The *Davis* and the *MeindlNMFNonhyd* formulations perform second best, showing an improvement over the *ChenHerringNonhyd* while the *MacMillan* formulation which assumes the geometric elevation angle is equal to the apparent elevation angle performs slightly worse than the more rigorous *Davis* formulation.

The RMS of the residuals for the non-hydrostatic functional formulations are shown in

Figure 4.21: RMS of the discrepancies between the non-hydrostatic asymmetric linear horizontal gradient functional formulations and the three dimensional ray-tracing with respect to latitude. Units of millimeters.

Figure 4.21. For the non-hydrostatic functional formulations, a slight improvement of the RMS could be seen for stations near the equator. This was in contrast to the hydrostatic results for the linear horizontal gradients which had the best performance at mid- to high-latitudes.

There appears to be a hemisphere dependence in the results, with southern hemisphere stations experiencing a small RMS than the northern hemisphere stations. One possible cause of this hemisphere dependence could be due to the amount of meteorological information that is available for the assimilation process. Typically the meteorological data is more plentiful in the northern hemisphere where as the southern hemisphere may rely more on climatologies rather than actual observations. As the actual meteorological observations would capture the day-to-day fluctuations of the water vapor more realistically, therefore leading to the higher RMS of the results.

Figure 4.22 shows the mean RMS for the spherical harmonics and 2nd order polynomial functional formulations at elevation angles of $3° - 20°$. A very similar pattern to the

hydrostatic results can be seen although both the magnitude of the RMS and the variability, indicated by the error bars, are larger than for the hydrostatic case. Below five degrees, the 2nd order polynomial (*Seko*) performs the best, with an RMS of approximatly 10 mm or less for all elevation angles. As the elevation angle grows, the spherical harmonics of degree 2 and order 1 (*SH*21) has the smallest RMS as well as the smallest standard deviations.

Figure 4.22: Mean RMS and standard deviation of the non-hydrostatic 2nd order polynomial and spherical harmonic functional formulations errors with respect to the three dimensional ray-traced slant factors multiplied by a nominal 220 mm, for elevation angles $3°$, $5°$, $7°$, $10°$, $14°$ and $20°$. Units of millimeters.

Figure 4.24 shows the mean asymmetry of the non-hydrostaticslant factors multiplied by a nominal zenith delay of 22.0 cm versus azimuth at the $3°$ elevation angle for all

Figure 4.23: RMS of the discrepancies between the non-hydrostatic asymmetric 2nd order polynomial and spherical harmonic functional formulations and the three dimensional ray-tracing with respect to latitude. Units of millimeters.

stations over the year 2008. Each box in the figure represents a station, along the x- axis is the azimuth, and along the y axis is the nominal asymmetric non-hydrostatic delay. There is a slight latitude dependence for high- northern and southern latitudes. This is caused by the amount of water vapor being less as you move away from the equator and towards the poles. For the northern latitudes, this produces a maximum at an azimuth of $\sim 180^\circ$ and a minimum at an azimuth of $\sim 0^\circ$ while the opposite occurs in the southern hemisphere. The standard deviation of the mean non-hydrostatic asymmetry is also much larger than the for the hydrostatic component. This indicates that the direction of the non-hydrostatic gradient is more variable as compared to the hydrostatic component.

Local conditions have a large influence on the mean asymmetry of the non-hydrostatic delay. This can be seen very well for station POL2, located in Bishkek, Kyrghyzstan. This site is located on the north side of the Kyrgyz Range, which is part of the Tian Shan Mountains. As there are no large bodies of water nearby, the mountains are the main driver of the climate. The tall peaks located to the south tend to lock the moisture in
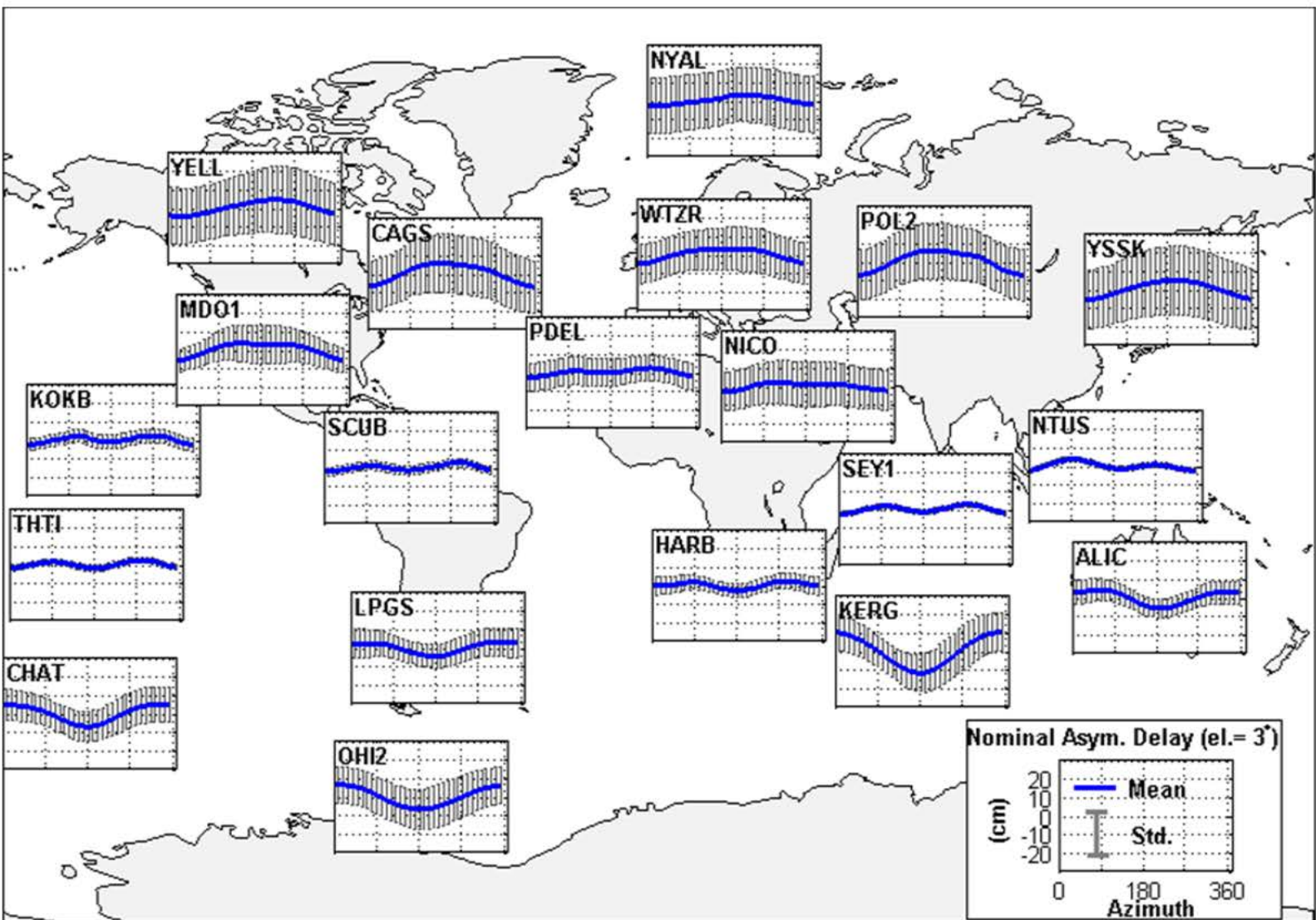
Figure 4.24: Mean asymmetry of the non-hydrostatic slant factors multiplied by a nominal zenith delay of 22.0 cm at the 3° elevation angle with respect to azimuth, over the year 2008, for all 20 IGS stations.

86

the mountains which receive large amounts of precipitation while an undulating steppe extends toward the north [of Congress, 1997]. This can be seen in Ghoddousi-Fard et al. [2009a, fig.5, p.1119]. These extreme climatic differences are most likely the cause of the large north-south gradient at the station which has a peak-to-peak amplitude of 40 cm.

The non-hydrostatic C coefficient was computed following the same manner as the hydrostatic coefficient and the results are shown with respect to latitude in Figure 4.25. No clear pattern can be seen in the results although it appears that equatorial and high-latitude stations have a larger variability that mid-latitude stations. The weighted mean was computed and was found to be equal to 0.0016 ± 0.0007 which is within one standard deviation of 0.0010 obtained in Chen and Herring [1997].
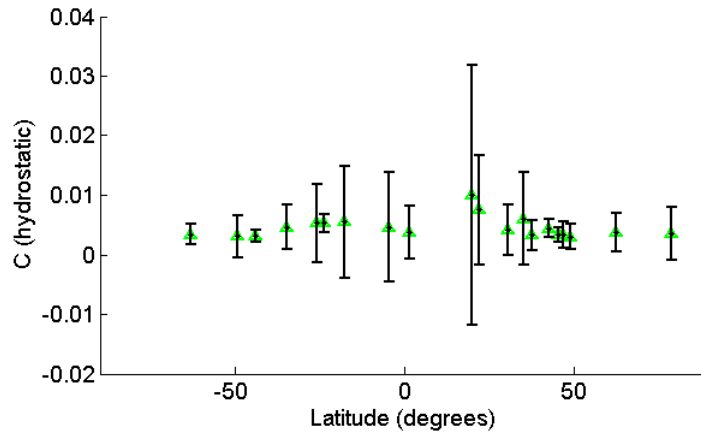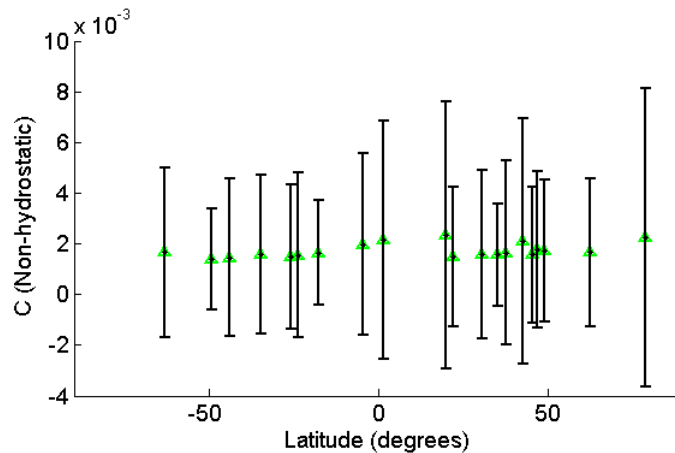

Figure 4.25: Mean values and standard deviations (1σ) of the non-hydrostatic C coefficient versus latitude.

4.3.3.3 Total

Figure 4.26 shows the mean RMS of the residuals, and the respective spread, for the linear horizontal gradient functional formulations. The magnitude of the RMS at $3°$ is approximately 20 mm for all functional formulations. For elevation angles above $5°$ the *ChenHerringEst* performed significantly better than the other formulations, reducing the

RMS by half in some cases. *ChenHerringTot*, which uses a value of $C = 0.0032$ did not perform as well as the estimated C value but performed equally well as the *MeindlNMFNonhyd* and the *Davis* formulations. Again the *MacMillan* formulation appears to have performed slightly worse than the other formulations with an RMS of 2–3 mm larger at the $5°$ elevation angle than the other formulations.
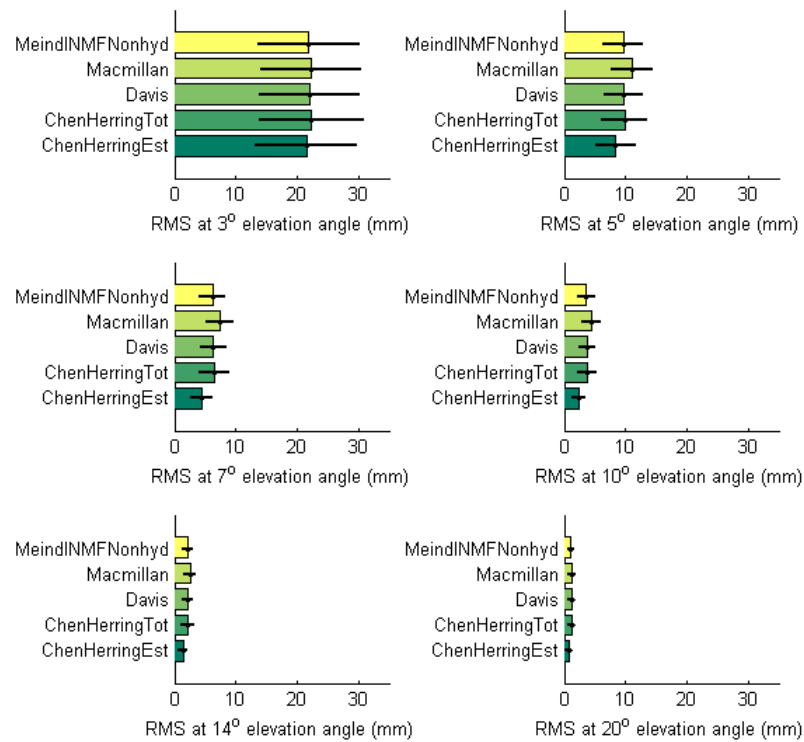
Figure 4.26: Mean RMS and standard deviation of the total linear horizontal gradient functional formulations errors with respect to the three dimensional ray-traced slant factors multiplied by a nominal 2520 mm, for elevation angles 3°, 5°, 7°, 10°, 14° and 20°.

Figure 4.27 shows the existence of a latitude dependence in the RMS of the linear horizontal gradient formulations. For stations at the equator, the RMS is typically twice as large as for high latitude stations. This latitude dependence is mostly due to the non-hydrostatic component as the RMS of the hydrostatic component was typically less than
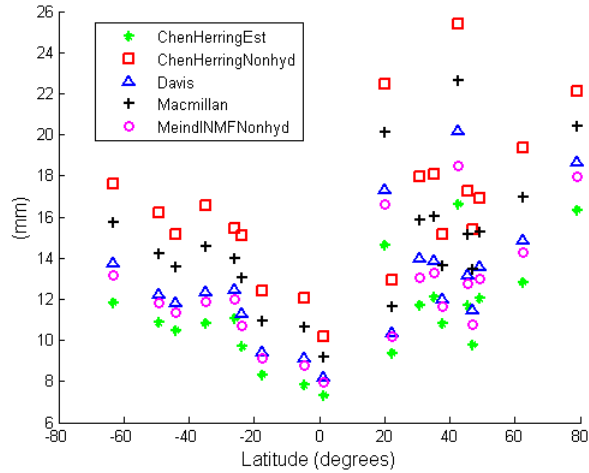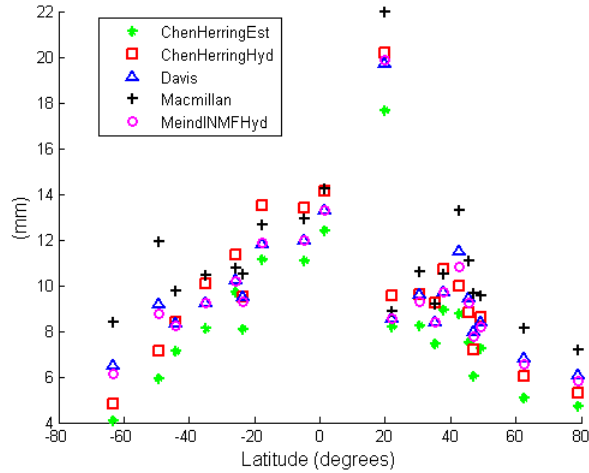
Figure 4.27: RMS of the discrepancies between the total asymmetric linear horizontal gradient functional formulations and the three dimensional ray-tracing with respect to latitude. Units of millimeters.

6 mm at $5°$ elevation angle for all latitudes. Station SCUB experiences the largest RMS (shown at a latitude of $\sim 20°$N). This will be address shortly.

The RMS of the spherical harmonics expressions and the 2nd order polynomial are shown in Figure 4.28. Again the *Seko* formulation performs excellent at low elevation angles although for higher elevation angles of $7°$ and $10°$ the spherical harmonics of degree 2 and order 1 (*SH*21) shows a slight improvement.

The latitude dependence of the spherical harmonics and 2nd order polynomial is less pronounced than the linear horizontal gradient formulations. In particular, the *Seko* formulation experiences almost no latitude dependence at all. Both *SH*11 and *SH*21 show a latitude dependence, performing best at high latitudes, with an RMS of about 5–6 mm, although suffering somewhat for equatorial stations, with the RMS growing to slightly larger than 10 mm.

Once again these latitude dependent variations can be explained by the studying the geographic variation of the total asymmetric delay shown in Figure 4.30. The azimuth
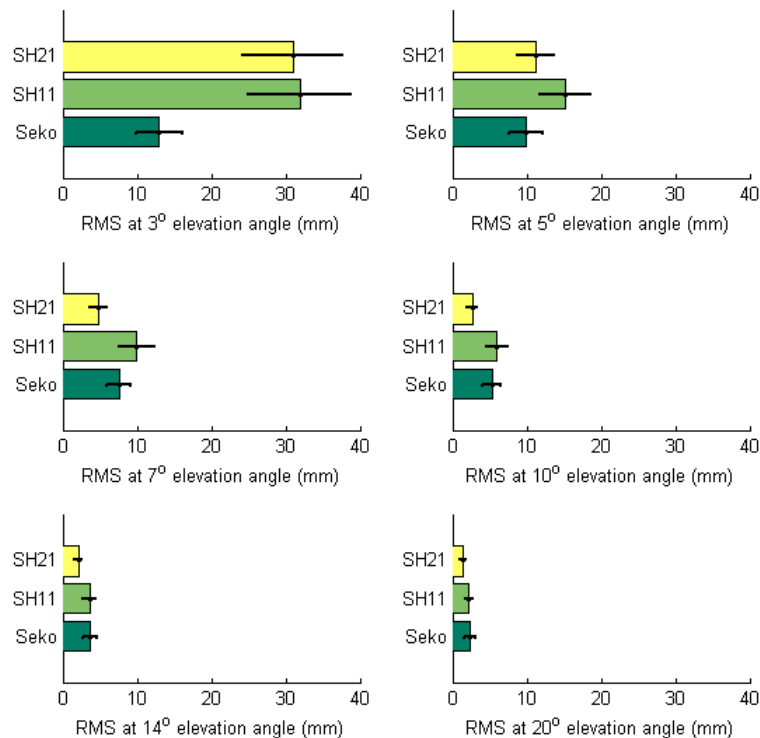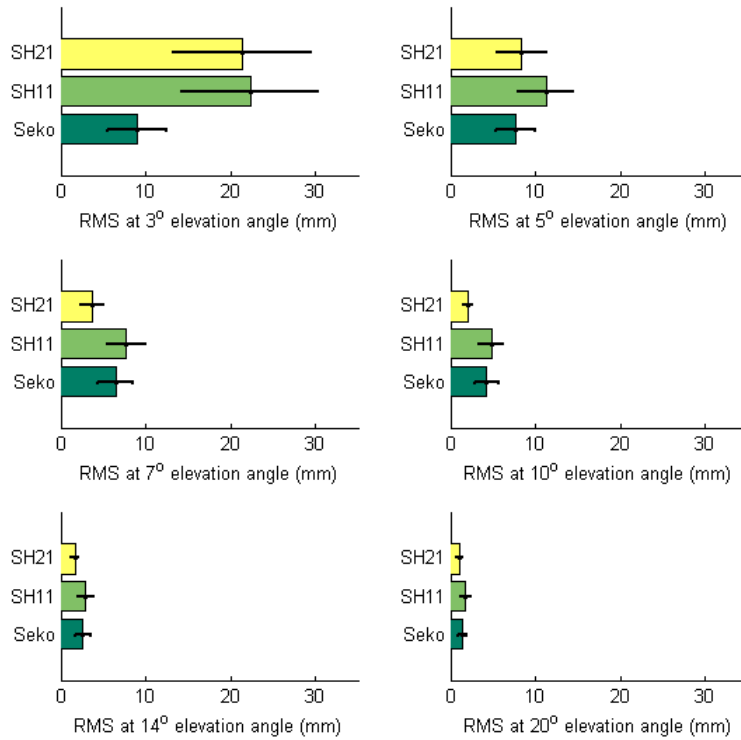
Figure 4.28: Mean RMS and standard deviation of the total 2nd order polynomial and spherical harmonic functional formulations errors with respect to the three dimensional ray-traced slant factors multiplied by a nominal 2520 mm, for elevation angles $3°$, $5°$, $7°$, $10°$, $14°$ and $20°$. Units of millimeters.

dependence for the total slant factors is typically dominated by the non-hydrostatic component. Several stations still have their hydrostatic signature, such as station KOKB and THTI which still exhibit the bi-modal trend which was seen in the hydrostatic component in Figure 4.18. In these cases, the non-hydrostatic component performed in a largely stochastic nature with approximately a zero mean but a standard deviation of 15–20 cm at $3°$ elevation angle. The peak-to-peak amplitude of the total asymmetric delay ranges anywhere from only a few centimeters to 25 cm at the $3°$ elevation angle.

Coming back to station SCUB, all asymmetric functional formulation performed worse
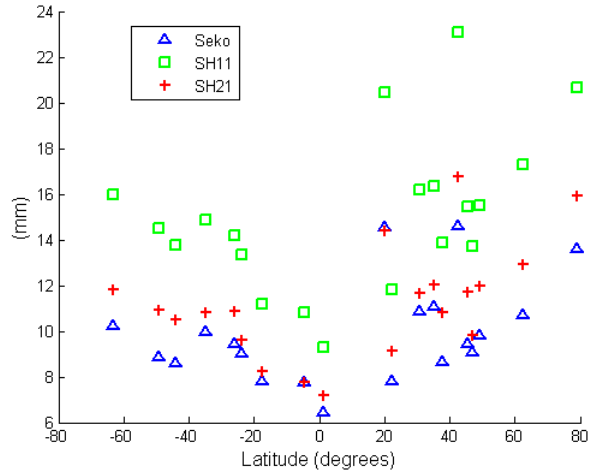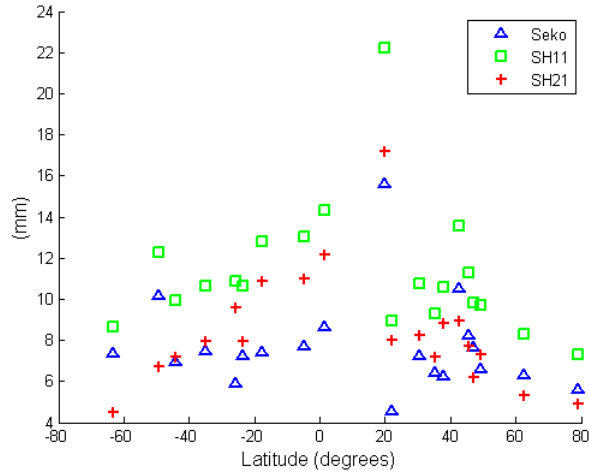
Figure 4.29: RMS of the discrepancies between the total asymmetric 2nd order polynomial and spherical harmonic functional formulations and the three dimensional ray-tracing with respect to latitude. Units of millimeters.

at this station. From Figure 4.30, we can see that this is due to the skewed nature of the asymmetric slant factors, which makes it difficult for the functional formulations to properly represent the feature which has a maximum at $\sim 300°$. This feature is mainly due to the non-hydrostatic delay which can be seen by looking at Figure 4.24.

In terms of which formulation would be best for estimating the total gradient using space geodetic observations, the *MeindlNMFNonhyd* and the *ChenHerringTot* formulation are recommended. If a *C* coefficient could be determined on an epoch/site specific basis, or if a strong correlation could be found between a the magnitude of the coefficient and a site specific parameter then this would improve the Chen & Herring formulation and therefore it would be recommended when the highest accuracies are required. However, at this time no such parameter has been determined.

Plotting the total *C* coefficient for each station versus latitude (Figure 4.31), no clear latitude dependence can be seen in the mean value. More substantial though, is the amount of variation seen for all stations. This indicates that the value of *C* can vary quite dramat-
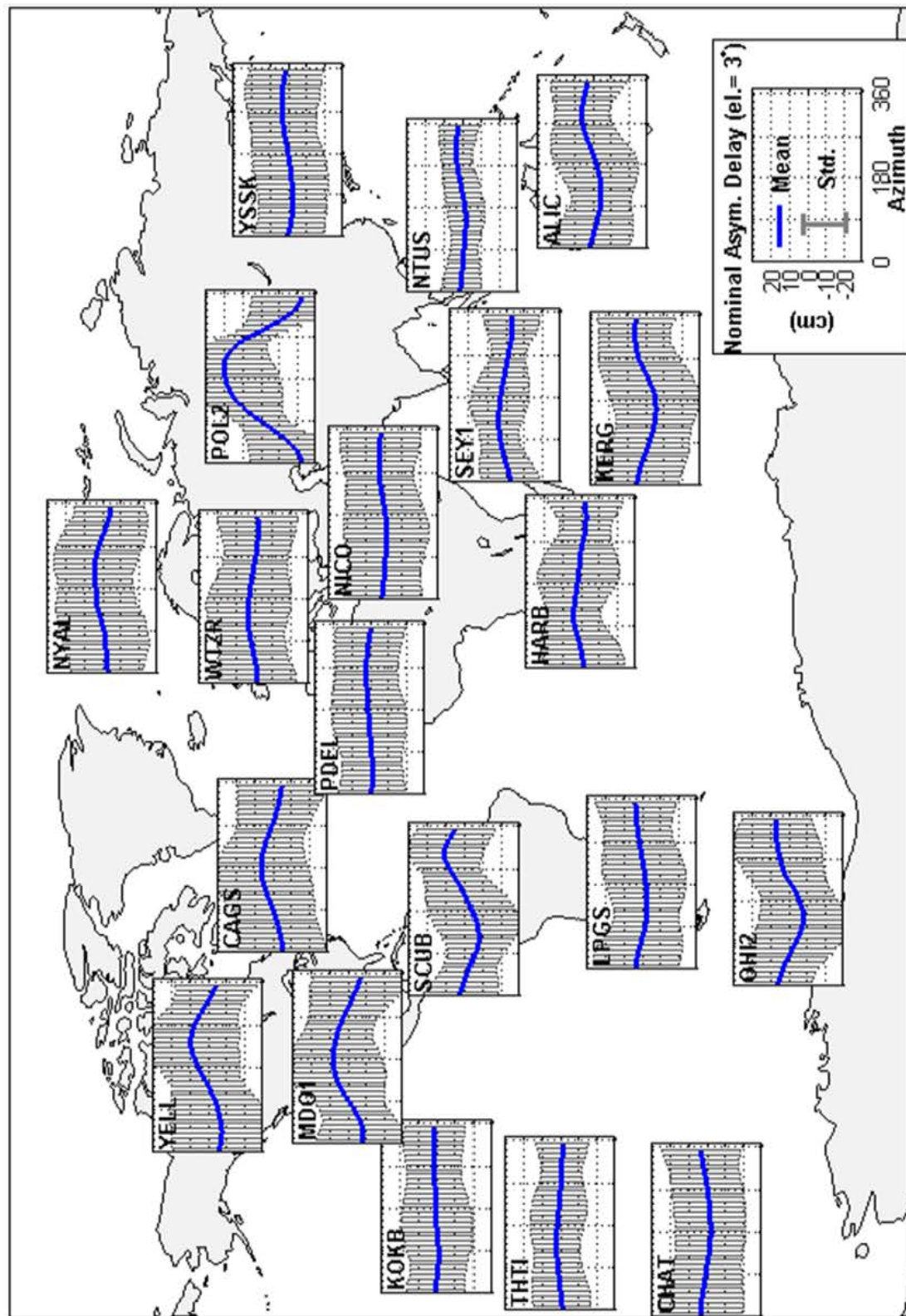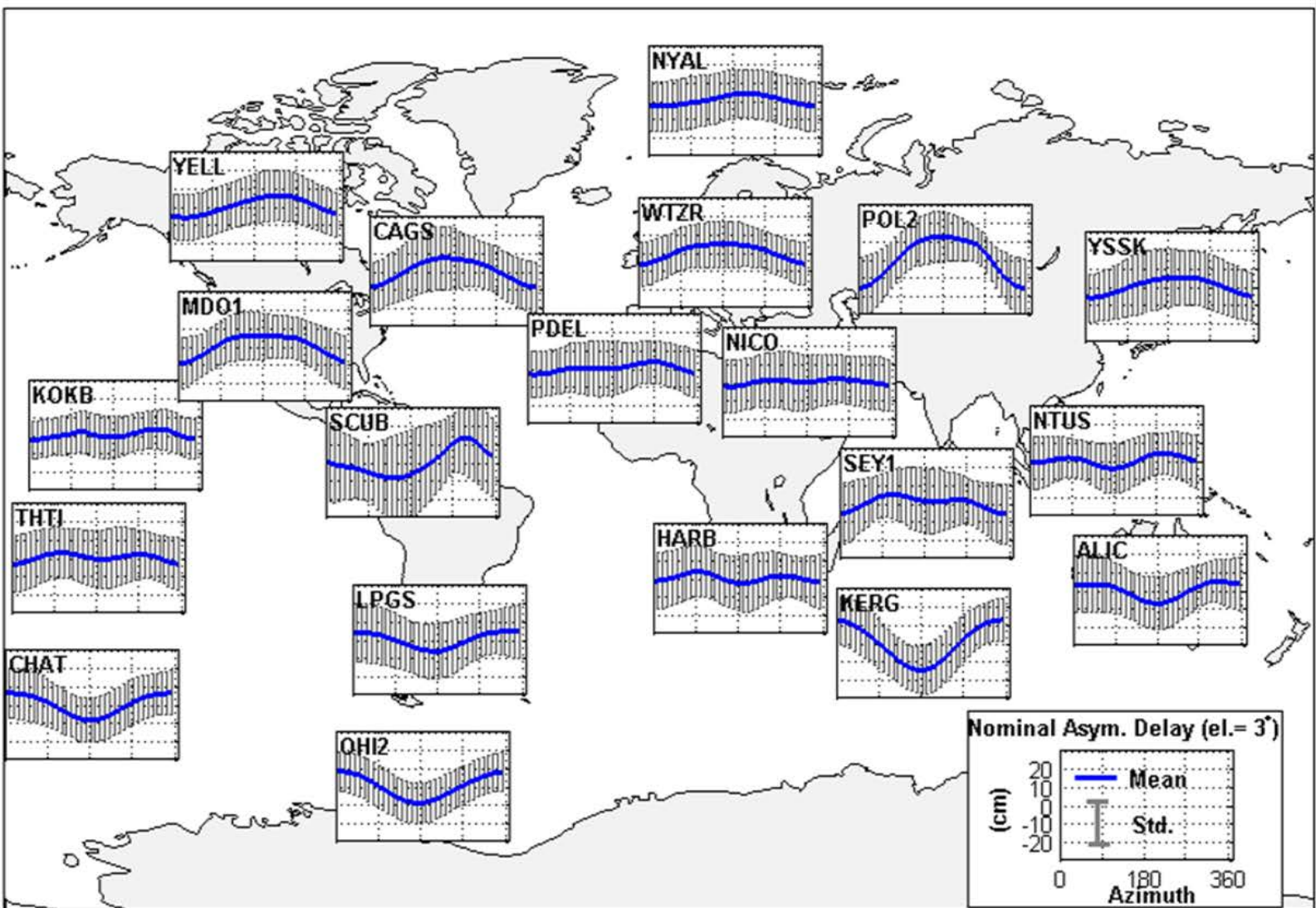
Figure 4.30: Mean asymmetry of the total slant factors multiplied by a nominal zenith delay of 252.0 cm at the 3° elevation angle with respect to azimuth, over the year 2008, for all 20 IGS stations.

92
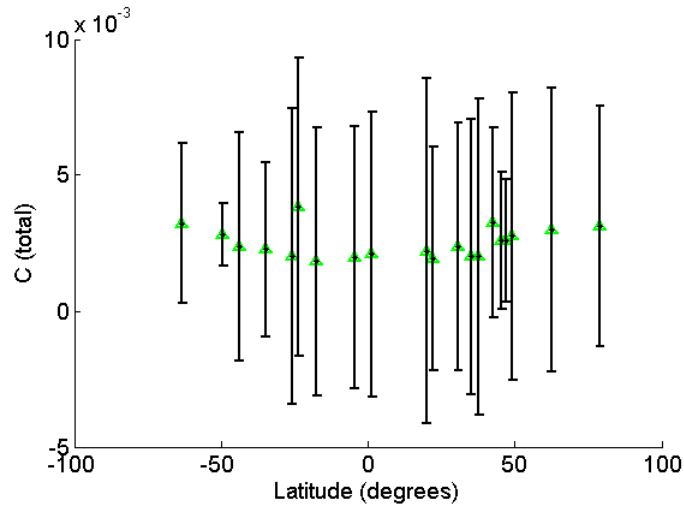
Figure 4.31: Mean values and standard deviations (1σ) of the total C coefficient versus latitude.

ically dependent on the local conditions at any given time. The weighted mean of the C coefficient was obtained, using the mean station values and their standard deviations, and a value of 0.0026 ± 0.0007 was determined. This is slightly smaller than the 0.0032 suggested by Chen and Herring [1997] but once again falls within one standard deviation at the 1σ confidence interval.

4.3.3.4   Comparison of Total Linear Horizontal Gradients

The differences in the gradient mapping function of the linear horizontal gradient functional formulations will have an effect on the magnitude of the estimated gradients. For space geodetic techniques, this could be an important consideration when comparing solutions between different software and techniques. To identify the impact of the gradient mapping functions, the estimated gradient parameters in the north-south and east-west directions were compared.

Figure 4.32 show the north-south and east-west gradients estimated by fitting the linear horizontal gradient formulations to the three dimensional ray-traced delays for the

total component. The *Meindl* functional formulation, on average, estimates larger gradients then the other techniques, while the *MacMillan* formulation estimates the smallest gradients. The error bars have been left off to reduce clutter, but typically the standard deviation is larger than the differences seen between the gradient parameters.
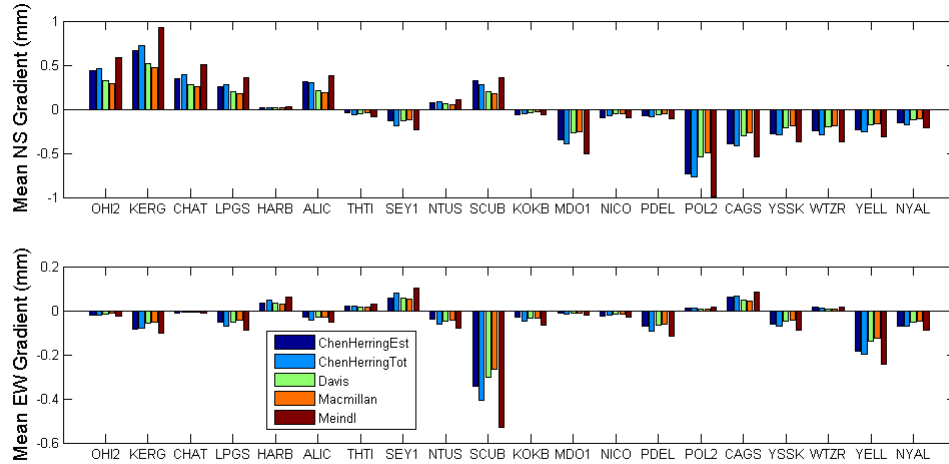
Figure 4.32: Mean north-south and east-west total gradients determined from the linear horizontal gradient functional formulations.

4.4   Summary and Recommendations

We have assessed the current state-of-the-art mapping functions and functional formulations used for space geodetic techniques. This was the first global evaluation of these mapping functions using three dimensional ray-tracing. We also investigated the fitting of the symmetric functional formulations to the three dimensional ray-tracing to identify if there exist any deficiencies in the mathematical model used to represent the elevation dependence of the tropospheric slant factors. Finally we evaluated several asymmetric functional formulations which are currently used for modeling the asymmetric delay for space geodetic techniques as well as several formulations which have not been extensively

tested.

In terms of the mapping functions, the VMF1 performed extremely well introducing less than 1 mm errors in station height and therefore it supports the fact that it is currently the recommend mapping function for geodetic applications. A small latitude dependence was found in the hydrostatic mapping function which was determined to be caused by the assumption of a spherical earth in the ray-tracing performed for the VMF1. As well, the GMF was found to be a good back up as it would not introduce a significant bias with respect to the VMF1 although a larger repeatability is to be expected.

For the symmetric functional formulations it was found that the *Marini*3 coefficient functional formulation is adequate for modeling the elevation angle dependence of the three dimensional tropospheric slant factors to below 1 mm down to an elevation angle of 3°. A slight improvement was found when a fourth coefficient was added (*Marini*4) however, it was not found to be a large enough improvement to warrant the adoption of this model. The use of the VMF parametrization could potentially be improved upon by estimating all three of the Marini coefficients rather than using the empirical coefficients, although this would need to be weighed against the added computation costs and an improvement in the position domain would need to be demonstrated.

The *Chen & Herring* asymmetric functional formulation and the *Meindl* formulation which uses the "tilting atmosphere" approach were found to be the optimal linear horizontal gradient formulations. When estimating gradient parameters in along with position and other nuisance parameters for positioning purposes, one of these two formulations should be used. When the "C" coefficient of the Chen & Herring formulation was estimated along with the other paramors in some cases there was a significant improvement although no clear parametrization of this coefficient could be established. Therefore an empirical model, either a function of latitude or some site/epoch specify parameter may improve the performance of the original Chen & Herring functional formulation and there-

fore this should be investigated further.

For the most part, the *Seko* and second degree spherical harmonics (*SH*21) was able to reduce the RMS of the residuals when compared to the linear horizontal gradient formulations, particularly at elevation angles below 7°. Although these models may not be practical for estimating the unknown coefficients from space geodetic observations, they may provide a means of representing the asymmetry of the troposphere in a closed-form manner which could be used to distribute corrections for the asymmetric tropospheric delay to users in a convenient manner.

Even with the additional parameters, several stations experienced an RMS of greater than 10 mm at the 5° elevation angle. Therefore, it may be necessary to explore higher order formulations, or this indicate that the use of ray-traced slant factors at the observation level may prove beneficial for high precision geodetic positioning. This is what will be explored in the chapter to come.

Chapter 5

Effect of Ray-traced Slant Factors on Estimated Geodetic Parameters

Although the experiment performed in Chapter 4 provided some insight into the deficiencies in current mapping functions, in the end we are mainly concerned with the impact of the tropospheric delay on the estimated geodetic parameters, in particular the receiver position. For this purpose a global subset of IGS stations was processed using the precise point positioning (PPP) technique [Zumberge et al., 1997; Kouba and Héroux, 2001].

The objective of this section is to compare the application of ray-traced slant factors to the current state-of-the-art approaches for modeling the tropospheric delay for geodetic positioning. Four strategies for modeling the azimuth and elevation angle dependence of tropospheric delay in PPP are assessed: (1) VMF1 with estimation of residual zenith delay; (2) VMF1 with estimation of residual zenith delay and two gradient parameters; (3) Ray-traced slant factors with estimation of residual zenith delay; and (4) Ray-traced slant factors with no estimation of tropospheric parameters. In addition, this processing will also act as a means of validating the ray-traced zenith delays produced by ray-tracing through the global CMC-GEM.

We begin with a review of the current strategies for mitigating the tropospheric delay for geodetic positioning. Next, a description of the PPP technique including the basic observable and correction models is given and the details of the processing strategy for the global campaign is provided. Finally, we present the impact of the various strategies on the positioning results, estimated parameters and convergence of the PPP solution.

5.1 Troposphere Delay Mitigation in Geodetic Positioning

Troposphere delay mitigation is a challenge for millimeter level positioning, especially in the height domain. Although the hydrostatic component of the delay is relatively stable, the non-hydrostatic delay can fluctuate quite rapidly which makes its prediction very difficult. For this reason, a residual tropospheric delay parameter must be estimated using the geodetic observations. On the other hand, the hydrostatic zenith delay, can be sufficiently modeled, following Saastamoinen [1972], as:

$$d_h^z = \frac{0.00227768 \cdot P_0}{1 - 0.00266\cos(2\phi) - 0.00028 \cdot h_{ref}},$$

(5.1)

where P_0 is the surface pressure at the site, ϕ is the station latitude and h_{ref} is the station height above the geoid in kilometers. Alternatively, if in situ measurements are not available, the zenith hydrostatic delay can be determined from ray-tracing through a NWM such as suggested by Boehm et al. [2006b].

The zenith non-hydrostatic delay must be estimated using the geodetic observations. Typically this parameter is refereed to as the residual zenith delay (δT) as it contains other elevation angle dependent errors, for example, mis-modeling of the hydrostatic component of the delay. In order to make the residual zenith delay parameter common among all satel-

lites and allow for its estimation, the residual slant delay of each observation is mapped to zenith using the non-hydrostatic mapping function. The residual zenith delay parameter is then estimated along with the other parameters, using either a piece-wise linear function or allowed to vary in a stochastic nature.

The optimal mapping function for both the hydrostatic and non-hydrostatic delays has been a continuous source of development. In Chapter 3 we discussed the various mapping functions which have been developed over the last decade. Currently, the VMF1 hydrostatic and non-hydrostatic mapping functions are recommended for all geodetic applications. In case these are not available, then it is recommended to use the GMF as it is fully consistent with NWM derived mapping functions [Boehm et al., 2006a].

MacMillan [1995] showed that the inclusion of the linear horizontal gradient slant factor model, with two parameters, G_N and G_E, which describe the asymmetry of the atmosphere, was beneficial for geodetic positioning. As it is not possible to separate the hydrostatic gradients from the non-hydrostatic gradients it is usually suggested to estimate the total gradients which is the combined effect of the hydrostatic and non-hydrostatic terms. However, Niell [2003] suggested that it may be beneficial to first remove the hydrostatic gradients and only estimate the non-hydrostatic gradients although this is not typically done in practice.

The inclusion of the three tropospheric parameters (δT, G_N and G_E) can lead to an over parametrization of the design matrix. In order to reduce the number of estimated parameters, several authors have investigated the use of ray-tracing at the observation level. Hobiger et al. [2008b] processed 13 sites from the IGS receiver network located within the Japanese Meteorological Agency (JMA) meso-scale weather model. They found that ray-traced delays without estimation of a residual zenith tropospheric delay parameter were not accurate enough to achieve cm level positioning in the height component. However, the horizontal component still yield sub-centimeter repeatability even without the estima-

tion of the tropospheric parameters. When a residual zenith delay parameter was estimated along with the ray-traced delays, a slight reduction in the north, east and up components was found when compared to the approach, using the GMF and estimating a residual zenith delay and two gradient parameters. Using a fine mesh-model, further improvement was seen during extreme weather events such as the passage of a typhoon [Hobiger et al., 2010].

MacMillan and Gipson [2009] applied ray-traced slant delays in a VLBI campaign and compared the results to an approach of using the VMF1 and assuming no horizontal variation of refractivity. They found reduction in baseline scatter in 75% of the stations when applying the ray-traced slant delays at the observation level.

Nordman et al. [2009] applied ray-traced delays obtained from the European High Resolution Limited Area Model (HIRLAM) to a Finnish regional GPS network. The solutions were computed using the double difference approach and it was found that the use of the ray-traced slant delays gave a 60% improvement over the solution which did not estimate any residual zenith delay or gradient parameters. When these parameters were estimated, there was no statistical improvement.

5.2 Precise Point Positioning

PPP is a technique for processing GNSS observations using a single receiver. Unlike traditional processing strategies, PPP uses un-differenced observations to determine the absolute position of a receiver on or near the Earth's surface. This makes it particularly susceptible to errors in troposphere zenith delays or mapping functions. PPP takes advantage of the precise carrier phase measurements, along with a priori orbit and clock products, to obtain centimeter level accuracy assuming the parameters have sufficient time to converge. In order to eliminate the effect of the ionosphere, PPP takes advantage of the

ionosphere delay-reduced linear combinations of the pseudorange (P_3) and carrier-phase observations (Φ_3). The simplified observation equations, in units of meters, are:

$$P_3 = \rho + c(dT - dt) + T + e_p,$$ (5.2)

and

$$\Phi_3 = \rho + c(dT - dT) + T + N\lambda + e_\Phi,$$ (5.3)

where ρ is the geometric range between satellite and receiver, c is the vacuum speed of light, dT and dt are the ionosphere reduced receiver and satellite clock errors, λ is the ionosphere delay-reduced carrier phase wavelength, N is the ambiguity and e_p and e_Φ is the ionosphere delay-reduced pseudorange and carrier phase noise and multipath. As it is not possible to separate constant receiver and satellite biases from the ambiguity N, the integer nature of the ambiguity cannot be utilized as is done in double differenced observations. This is one of the major limiting factors of PPP as it typically requires several hours for the parameters to converge and allow for cm level positioning accuracies.

As the satellite clock corrections (dt) are determined a priori to a sufficient accuracy by the IGS, this value can be fixed. The troposphere term, T, is composed of an a priori value and the residual zenith delay (δT) which must be estimated along with the receiver position (X, Y and Z), the receiver clock dT and one carrier phase ambiguity per satellite N_i.

In order to achieve centimeter level accuracy several error sources must be modeled including solid earth tides, ocean tidal loading, satellite antenna phase wind-up, satellite/receiver antenna offsets and satellite/receiver phase center variations. More details on these models including a comprehensive description of the error sources in PPP can be found in Kouba [2009].

Urquhart [2009] showed that the application of atmospheric pressure loading (APL)

resulted in small, but consistent improvements in the repeatability of PPP time series. Additionally, APL plays an important role when evaluating tropospheric models. According to Steigenberger et al. [2008], modeling hydrostatic zenith delays using empirical pressure values instead of either in-situ measurements or ray-traced zenith delays, may lead to partial compensation of the atmospheric loading signal. Therefore it is recommended that if empirical values are used to derive the zenith hydrostatic delays, then atmospheric loading corrections should not be applied. If, on the other hand, in-situ measurements or ray-traced zenith hydrostatic delays are used, then APL corrections should be applied. As we are using the latter case, we therefore are applying atmospheric loading corrections.

The APL time series were provided by the Goddard VLBI group and are available on the Web at `http://gemini.gsfc.nasa.gov/aplo`. These time series use the algorithm described in Petrov and Boy [2004] whereby the Green's Functions are convolved with atmospheric pressure fields obtained from NCEP. The pressure field has a resolution of $2.5° \times 2.5°$ and are provided every 6-hours. A SNREI earth model was used adopting PREM elastic parameters (see Dziewonski and Anderson [1981]) and the oceans were assumed to behave as an inverted barometer.

5.3 PPP Analysis

Daily 24 hour RINEX files for the 16 stations shown in Figure 5.1 were processed using the PPP technique. Several stations from the previous experiment were excluded due either to strange behavior in the coordinate time series possibly due to equipment changes or a malfunctioning receiver, or there were large data discontinuities in the time series. The files were processed using GAPS, which implements the standard PPP model described above along with precise clock and orbit products produced from the IGS. Additionally, all necessary models are included in order to attain cm level positioning when processing

over a 24 hour period.
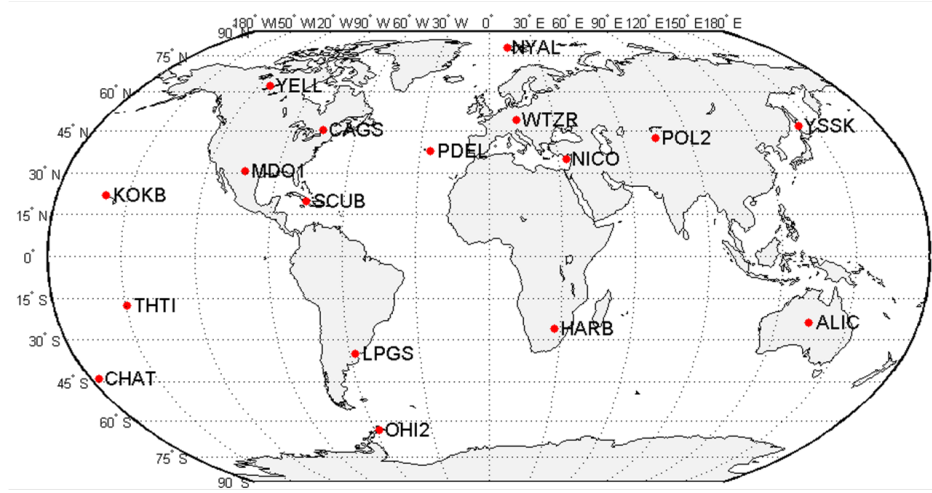
Figure 5.1: Global subset of IGS stations used in Experiment 2.

The unknown parameters are estimated using a forward only, sequential, weighted least squares filter of the form:

$$\boldsymbol{\delta}_i = (\boldsymbol{A}_i^t \boldsymbol{P}_i \boldsymbol{A}_i + \boldsymbol{C}_{\boldsymbol{\delta}_i^{-1}})^{-1} \boldsymbol{A}_i^t \boldsymbol{P}_i \boldsymbol{w}_i, \tag{5.4}$$

where $\boldsymbol{\delta}_i$ is the update vector, $\boldsymbol{A}_i$ is the design matrix, $\boldsymbol{P}_i$ is the observation weight matrix, and $\boldsymbol{w}_i$ is the misclosure vector all for epoch i. The covariance matrix of the estimated parameters, $\boldsymbol{C}_{\boldsymbol{\delta}_i}$, is updated at each epoch according to:

$$\boldsymbol{C}_{\boldsymbol{\delta}_i} = (\boldsymbol{A}_i^t \boldsymbol{P}_i \boldsymbol{A}_i + \boldsymbol{C}_{\boldsymbol{\delta}_{i-1}}^{-1})^{-1} + \boldsymbol{Q}_{\boldsymbol{\delta}}, \tag{5.5}$$

where $\boldsymbol{C}_{\boldsymbol{\delta}_{i-1}}$ is the covariance matrix from epoch $i-1$ and $\boldsymbol{Q}_{\boldsymbol{\delta}}$ is the process noise matrix.

The elevation angle cut-off was held fixed at 5 degrees, when available, and an observation weighting of $1/\sin\varepsilon$ was used. Non-tidal atmospheric pressure loading was applied at the coordinate level following Petrov and Boy [2004]. At the time of processing, GAPS

did not implement an ocean loading model. Since we are computing a solution over a 24 hour period, the majority of this effect would be removed and this is not expected to influence the results [Kouba, 2009].

The four different processing strategies which are assessed in this work are:

(1) VMF1 with estimation of residual zenith delay (VMF1): here, we assume that the atmosphere is symmetric. The VMF1-gridded mapping functions are used along with the a priori zenith delays, constrained to 2 cm, derived from the ECMWF analyses. The residual zenith delay is estimated using a random walk parameter of $5mm/\sqrt{(hr)}$.

(2) VMF1 with estimation of residual zenith delay and two gradient parameters (VMF1+grad): as suggested in McCarthy and Petit [2004], a N-S and E-W gradient are estimated from the GPS observations. The gradient parameters are estimated on an epoch-by-epoch basis using eq. (3.14). The gradient mapping function from Chen and Herring [1997] is used with C =0.0032. The gradient parameters are estimated using a random-walk model and are allowed to vary at a rate of $3mm/\sqrt{(hr)}$.

(3) Ray-traced slant factors with estimation of residual zenith delay (RT+est): here the approach of applying slant factors at the observation level as described in section 2.4.2 is implemented. The a priori hydrostatic zenith delays are provided at 5 minute intervals, and initially constrained to 2 cm. A residual zenith delay is estimated using the non-hydrostatic slant factors and with a random walk parameter of $5mm/\sqrt{(hr)}$. The ray-tracing has been described in Appendix IV.

(4) Ray-traced slant factors with no estimation of tropospheric parameters (RT only): ray-traced slant factors are applied at the observation level as described in section 2.4.2. Once again ray-traced zenith delays are provided at 5 minute intervals although we no

longer estimate a residual zenith delay parameter. In this case there are no troposphere parameters estimated by the GPS observations at all. Therefore, any un-modeled tropospheric delay will almost completely propagate as a bias into the station height parameter as well as the receiver clock parameter.

5.4   Results and Discussion

For each station, a linear polynomial was fit to the coordinate time series in the local geodetic reference frame to remove any linear site displacements due to crustal motion. For the detection of outliers in the coordinate time series an absolute rejection threshold of 30 mm in the horizontal and 50 mm in the vertical with respect to the fitted polynomial is used in addition to a statistical threshold of $3\sigma_{TH}$, where σ_{TH} is the standard deviation in the north, east and up direction with respect to the fitted polynomial. Any outliers were removed from all four processing strategies to keep the time series homogeneous.

Next, the weighted repeatability with respect to the linear polynomial was computed according to [Blewitt, 1989]:

$$\sigma = \left[\frac{\frac{n}{n-1} \sum_{i=1}^{n} \frac{(b_i - b_0)^2}{\sigma_i^2}}{\sum_{i=1}^{n} \frac{1}{\sigma_i^2}} \right], \tag{5.6}$$

where n is the number of observations, b_i is the estimated position (either north, east or up) on the ith day-of-year, b_0 is the linear regression polynomial evaluated at the corresponding day-of-year and σ_i is the formal standard deviation obtained from the least squares estimate of the PPP solutions.

Table 5.1 shows the repeatability of the north, east and up components for each station over the entire year. The results of strategy 3 (using the ray-traced slant factors) compare well to the current state-of-the-art approach, strategy 2, which estimated two gradient

Table 5.1: Repeatability of the north, east and up components. Units of millimeters.

| | Solution 1 | | | Solution 2 | | | Solution 3 | | | Solution 4 | | |
	North	East	Up	North	East	Up	North	East	Up	North	East	Up
ALIC	2.9	3.1	5.2	2.2	2.8	4.0	2.5	3.1	4.7	2.7	5.4	27.7
CAGS	5.5	4.1	10.2	5.7	4.2	11.6	5.3	4.0	10.0	5.2	4.5	12.7
CHAT	2.6	3.7	5.9	2.1	3.2	5.2	2.4	3.3	5.6	2.5	4.5	19.5
HARB	3.2	4.3	5.8	2.6	3.9	5.4	3.0	4.3	6.0	3.2	5.8	27.8
KOKB	3.1	4.0	7.0	2.6	3.6	6.7	3.1	3.9	6.9	3.0	7.8	26.7
LPGS	2.8	3.1	7.5	2.6	3.1	7.4	2.7	3.1	7.4	2.7	5.4	25.0
MDO1	3.3	2.8	5.7	2.8	2.4	5.5	2.9	2.6	5.6	3.0	4.0	24.1
NICO	2.9	3.7	6.7	1.9	3.1	5.4	2.4	3.6	6.4	2.5	4.7	24.9
NYAL	3.1	2.8	7.9	2.2	1.9	6.8	3.1	2.2	7.6	3.1	2.6	16.3
OHI2	2.6	3.6	12.5	2.2	3.3	11.6	2.5	3.2	12.1	2.6	3.5	19.1
PDEL	3.9	3.9	9.0	2.8	3.5	8.2	3.3	3.9	9.0	3.4	5.1	26.5
POL2	2.4	2.9	4.3	2.0	2.6	3.6	2.3	2.9	3.6	2.3	4.1	26.9
SCUB	5.0	5.3	10.6	4.1	4.9	9.7	4.1	4.8	8.8	4.8	7.4	40.9
THTI	4.4	4.9	11.4	3.1	4.3	8.6	4.1	5.1	11.3	4.2	8.7	34.1
WTZR	2.8	2.7	4.1	1.7	2.5	3.9	1.9	2.5	4.0	2.0	3.0	15.8
YELL	3.3	3.9	5.3	2.6	3.4	5.2	2.8	3.4	5.3	2.9	3.8	16.3
YSSK	3.3	3.0	6.7	2.1	2.5	6.3	2.3	2.8	6.1	2.4	3.4	16.4
Avg.	3.35	3.63	7.40	2.66	3.25	6.76	2.98	3.45	7.09	3.10	4.92	23.57

parameters. In the up direction, strategy 2 shows a reduction of 0.3 mm while in the horizontal component reductions of 0.3 mm and 0.2 mm are seen in the north and east components respectively. Compared to the assumption of a symmetric atmosphere, Strategy 3 which implemented the ray-traced slant factors, had a reduction of 0.4 mm, 0.2 mm and 0.3 mm in the north, east and up components respectively.

In the horizontal component, strategy 4 performance is comparable to the strategies which estimated tropospheric parameters, allowing for sub-centimeter repeatability, and actually out-performing strategy 1 in the north component. Ghoddousi-Fard et al. [2009b] showed that the north-south gradient was highly correlated with the north (or latitude) component of the position. In this case, the 3D ray-traced slant factors act as a supplement to the gradient parametrization, but are still able to adequately model the asymmetry and therefore improve the repeatability in the north (or latitude) component.

Strategy 4 suffers significantly in the up component as it solely relies on the accuracy of the ray-traced zenith delays. Without a residual zenith delay parameter estimated any error in the ray-traced zenith delay will be absorbed mainly by the station height and clock parameters. In areas which are known to have low water vapor activity, such as OHI2, WTZR and YELL the repeatabilities of the up component are actually less than 2 cm. However, areas located near the equator (SCUB and THTI in particular), which experience more variation in the water vapor content of the atmosphere, show significant degradation of the solutions, with the repeatability reaching over 3 cm in the up component.

To have a better understanding of the overall performance of the strategies on the entire network as well as identify seasonal trends the RMS of the weekly solutions for the network as a whole was computed. Figure 5.2 shows the weekly RMS of the PPP solutions variability in the north, east and up component. The weekly station variability is computed as the RMS of the differences between the estimated coordinates and the linear regression polynomial for each station for week long segments.

From Figure 5.2 it is once again evident that the tropospheric parameters only have a marginal influence in the horizontal component as the four time series are nearly indistinguishable in the north component, and only strategy 4 performs worse by several mm's in the east component. However, in the up component, strategy 4 is significantly degraded due to the errors in the ray-traced zenith delays, most likely due to variations in the water vapor content of the atmosphere as we will discuss shortly. Notice that in Figure 5.2, the up axis is on a scale of nearly 5 times that of the north and east components.

In order to better understand the temporal variations, in particular, for the up component of strategy 4, two groups of stations were chosen. Group 1 represents the northern latitude region, including stations NYAL, WTZR, YELL and YSSK, and Group 2 represents the equatorial region, including KOKB, NICO, SCUB and THTI. Due to the sparse stations at the southern latitudes it was not possible to do a similar comparison for this
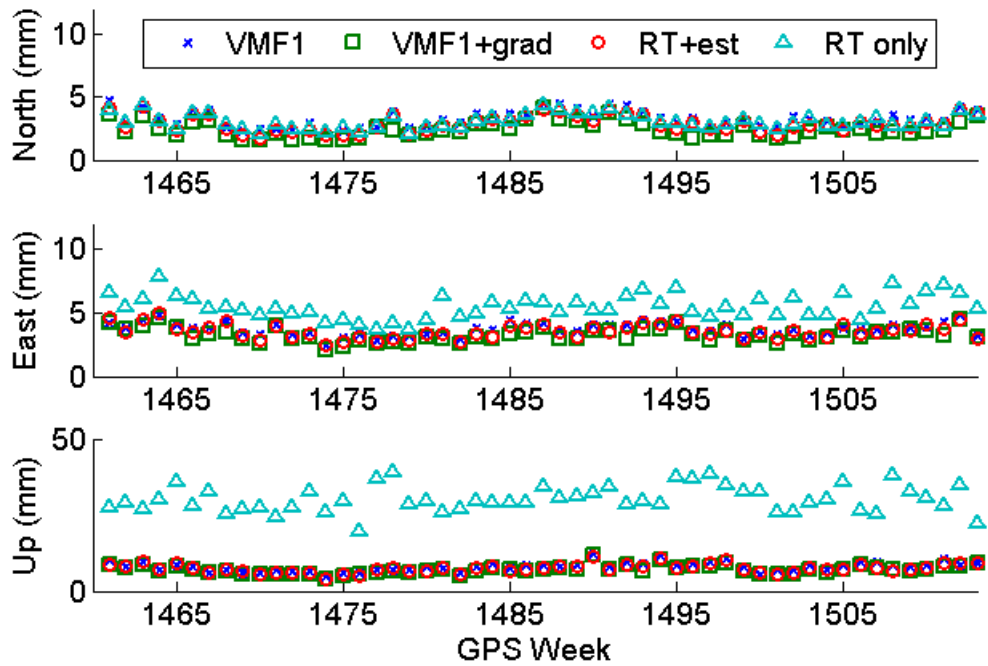
Figure 5.2: Weekly RMS of the north, east and up component of strategy 1 (VMF1), strategy 2 (VMF1+grad), strategy 3 (RT+est) and strategy 4 (RT only) for all of 2008, in millimeters

region as the stations are too inhomogeneous in latitude.

Figure 5.3 shows the weekly RMS of the up component of group 1, along with the monthly mean precipitable water (PW) in the surface layers up to the 500 mbar isobaric level. Precipitable water is a measure of the column water vapor content. According to Gaffen et al. [1992], mid- and high- latitude regions exhibit an annual cycle of atmospheric humidity, which is in phase with temperature, exhibiting a maximum in late summer and a minimum in winter. The RMS of strategy 4 is almost exactly in phase with the monthly mean precipitable water vapor which was obtained from Gaffen et al. [1992]. Strategies 1–3, which estimate tropospheric parameters, were not affected by these trends in the water vapor content as the residual zenith delay estimated from the GPS observations models the high variability which is associated with months of higher water vapor content. During
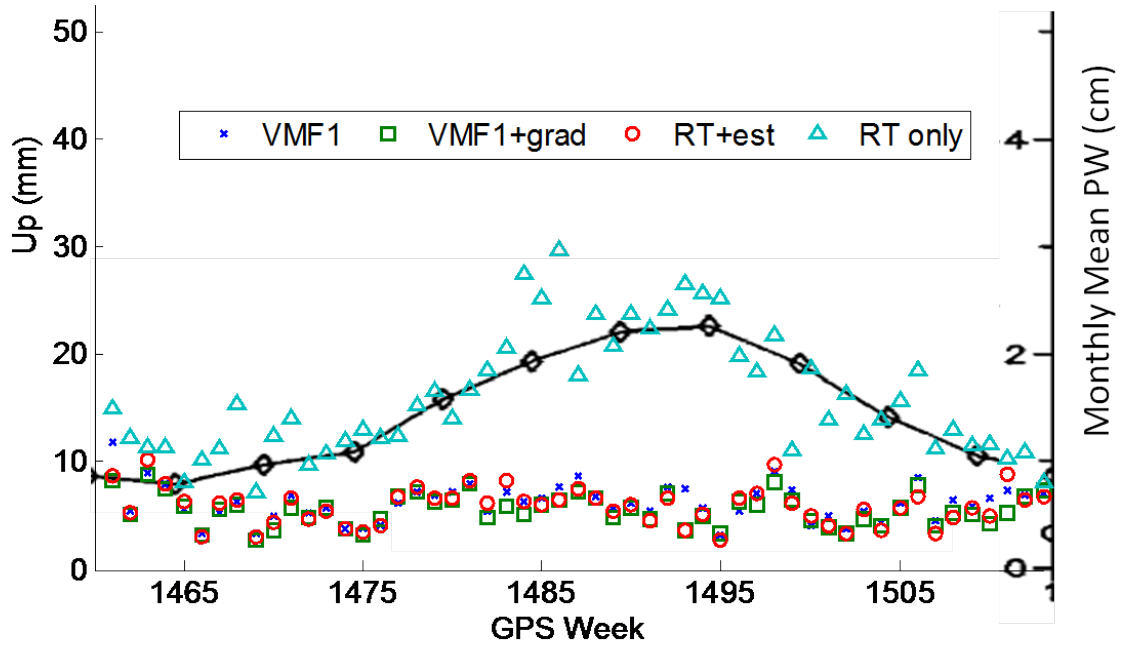
Figure 5.3: Weekly RMS of the up component for stations NYAL, WTZR, YELL and YSSK which represent high, northern latitudes in millimeters and the mean monthly precipitable water vapor in centimeters as given by Gaffen et al. [1992]

periods of low precipitable water vapour, the RMS of strategy 4 is actually quite good, less than 2 cm, while during the peak months, the RMS grows to nearly 3 cm.

Unlike the high latitude region, the equatorial region, shown in Figure 5.4 does not exhibit an obvious annual cycle in the RMS. This is partially due to the inhomogeneity of the four stations chosen, some located north of the equator while some are located south of the equator. Additionally, unlike the mid- to high- latitude stations whose partial water vapour is tied to the temperature, equatorial water vapour is closely related to mid-tropospheric relative humidity which is dependent on the local rainy season [Gaffen et al., 1992]. Therefore unlike the high northern latitude stations which all have maximum water vapour content in during the late summer, the equatorial stations are more inhomogeneous and no annual cycle is visible here. Therefore the repeatability at these locations is almost constant throughout the entire year, with a weekly RMS of the up component having a

mean of 4 cm.
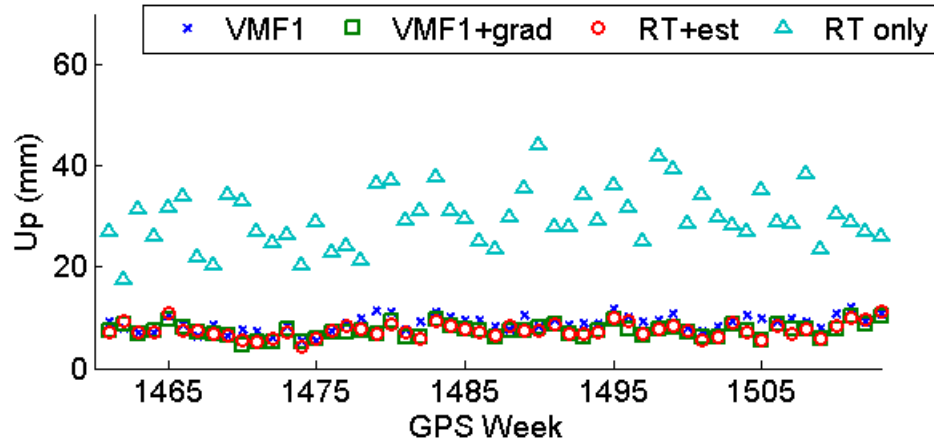
Figure 5.4: Weekly RMS of the up component for stations KOKB, NICO, SCUB and THTI which represent equatorial region. Units in millimeters

Overall, the estimation of a residual zenith delay and tropospheric gradient parameters produced the best station repeatability, closely followed by the use of ray-traced slant factors with estimation of residual zenith delay. It was demonstrated that even when not estimating a residual zenith delay parameter, ray-traced zenith delays can produce sub-centimeter level repeatability (1σ) in the horizontal component and several centimeter level positioning in the height component. The precision of this approach was heavily dependent on the local atmospheric conditions, and seasonal/geographic variations were seen which corresponded to seasons/areas of increased water vapor activity. The good performance of strategy 4 is an indication of the accuracy of the ray-traced zenith delays which we will assess in section 5.4.1.

The application of the 3D ray-traced slant factors along with the estimation of a residual zenith delay parameter (strategy 3) was an improvement over the symmetric VMF1 mapping functions which also estimated a residual zenith delay parameter. This indicates that the azimuth dependent variation of the 3D slant factors are able to model, at least partially, the actual azimuth dependence of the troposphere on GPS observations.

110

5.4.1 Accuracy of Ray-traced Zenith Non-hydrostatic Delays

The accuracy of the ray-traced zenith non-hydrostatic delays were assessed using the estimated non-hydrostatic delays obtained from the PPP processing. Kouba [2009] showed that the accuracy of the estimated non-hydrostatic delays from PPP are around 6 mm (1σ) or better therefore they will be a good indication of the accuracy of the ray-traced zenith delays. For the comparison only the final estimated value (24h UTC) of the zenith non-hydrostatic delay was compared to the ray-traced non-hydrostatic delay at the corresponding epoch. This was to ensure convergence of the PPP solution and to prevent over-sampling from producing optimistic results [Kouba, 2008].
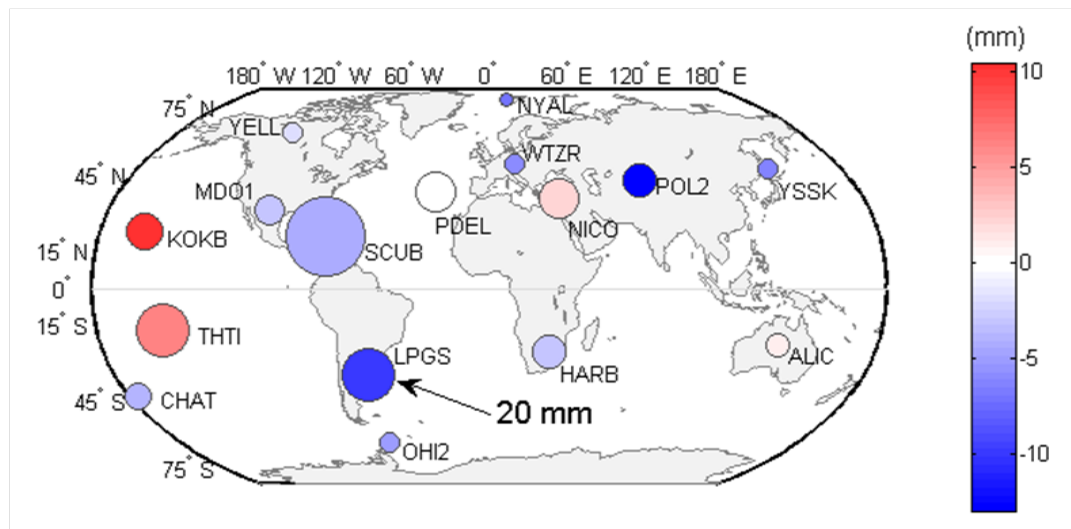
Figure 5.5: Mean bias (indicated by color bar) and standard deviation (indicated by size of marker) between the GPS derived non-hydrostatic zenith delays and ray-traced non-hydrostatic zenith delays derived from the CMC-GEM model.

Figure 5.5 shows the mean bias and standard deviation of the difference between the PPP estimated and the ray-traced non-hydrostatic zenith delays. The bias is indicated by the color bar on the right, while the standard deviation is indicate by the size of the marker. For reference, LPGS has a standard deviation of 20 mm as indicated in the figure. In terms of the bias, the majority of the stations exhibit a ray-traced delay that is larger than the

estimated delay. With the exception of two stations, the bias is generally less than 5 mm. In general, the largest variability occurs at stations located at mid- to equatorial latitudes and in tropical regions, the largest of which is station SCUB which has a standard deviation of 30 mm. Stations at high latitudes, and continental locations have smaller variability.

Figure 5.6 shows a histogram of the difference between the ray-traced and estimated non-hydrostatic delays for all stations and epochs. The mean of histogram is 2.96 mm while the standard deviation is 15.52 mm (1σ). The histogram is slightly skewed to the left indicating the tendency of the ray-traced delays to over-predict the non-hydrostatic delay.
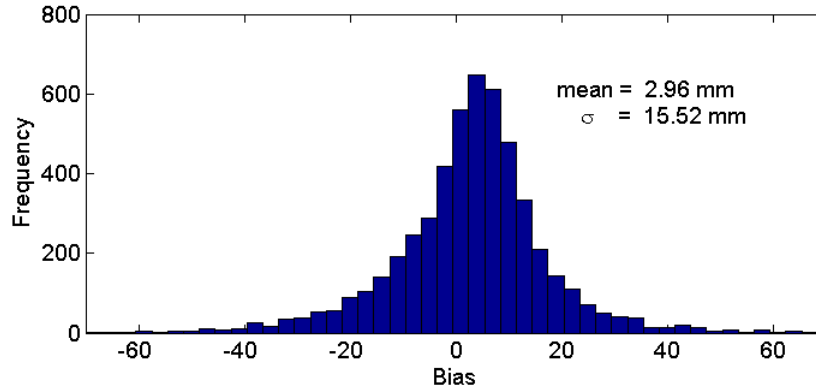
Figure 5.6: Histogram of the biases between the GPS derived and ray-traced non-hydrostatic delays.

Overall, there is good agreement between the ray-traced zenith non-hydrostatic delay and the estimated non-hydrostatic delay. Although the bias is small, only 3 mm, the main limiting factor of using ray-traced tropospheric delays without estimation of residual zenith delay parameter is the short term variability of the water vapor content in the atmosphere.

5.4.2   Estimated Gradients Versus Ray-traced Gradient

The gradients derived from strategy 2 are compared to the gradients estimated in Chapter 4 using the *ChenHerringTot* formulation. Both the PPP strategy and the ray-traced derived gradients, used the functional formulation of Chen and Herring [1997], with a value of C=0.0032. The main difference between these two types of gradients is that the PPP derived gradients are determined sequentially, in a weighted least squares filter over 24 hours, while the gradients determined from the ray-tracing are derived from a single epoch. Additionally, the observation distribution of the PPP gradients is much worse than the ray-traced gradients which will have a uniform distribution of observations throughout the sky. For this comparison, the elevation angle cutoff of the ray-traced delays was increased to 5 degrees to make it consistent with the elevation cutoff of the PPP processing. Although the techniques are inhomogeneous the mean gradients should be similar and provide some information ability of the NWM to describe the asymmetry of the GPS observations.

Table 5.2 show the mean, standard deviations and correlations of the gradients determined by ray-tracing through the CMC-GEM and those derived from PPP. Additionally, Figures 5.7 and 5.8 shows the mean north-south and east-west gradients plotted by station, in order of increasing latitude from left-to-right. In the plot we have also included for comparison, the north-south and east-west gradients computed at the Center for Orbit determination (CODE) for a homogenous reprocessed GPS campaign [Steigenberger, 2010].

Table 5.2 shows that the ray-traced and PPP derived gradients are all positively correlated. Typically the correlation is better for continental sites, such as YELL and WTZR, as well as high latitude sites such as NYAL and OHI2, while the correlation for coastal and equatorial sites is less. Although the three techniques are inhomogeneous, with respect to each other, the solutions agree well in most cases, both in magnitude and direction of the gradients. In terms of the east-west gradients, shown in Figure 5.8, most stations agree

Table 5.2: Mean, standard deviation and correlation between tropospheric gradients derived from PPP and from ray-tracing through the CMC-GEM model in units of millimeters.

| | | CMC-GEM | | | | PPP | | | | | |
| | | North | | East | | North | | East | | Correlation | |
Station	Latitude	Mean	Std	Mean	Std	mean	std	mean	std	North	East
OHI2	-63.3	0.44	0.37	-0.03	0.39	0.40	0.28	-0.18	0.26	0.55	0.46
CHAT	-43.9	0.42	0.48	0.02	0.51	0.15	0.37	-0.11	0.37	0.26	0.42
LPGS	-34.9	0.30	0.58	-0.05	0.60	-0.60	0.54	-0.09	0.61	0.22	0.16
HARB	-25.8	0.02	0.55	0.01	0.39	-0.20	0.43	0.07	0.32	0.34	0.16
ALIC	-23.6	0.27	0.54	-0.01	0.37	0.03	0.42	-0.09	0.32	0.44	0.24
THTI	-17.5	-0.03	0.71	0.06	0.67	-0.49	0.77	0.25	0.53	0.20	0.05
SCUB	20.0	0.60	1.10	-0.61	0.76	0.37	0.90	-0.39	0.74	0.09	0.20
KOKB	22.1	-0.05	0.36	-0.06	0.38	-0.37	0.43	-0.07	0.44	0.27	0.26
MDO1	30.6	-0.32	0.43	0.01	0.37	-0.27	0.29	-0.12	0.31	0.45	0.29
NICO	35.1	0.00	0.61	-0.02	0.50	0.01	0.41	0.02	0.40	0.38	0.22
PDEL	37.7	-0.06	0.62	-0.14	0.52	0.16	0.44	-0.20	0.35	0.16	0.28
POL2	42.6	-0.63	0.42	0.01	0.22	-0.56	0.45	0.02	0.18	0.31	0.28
YSSK	47.0	-0.26	0.50	-0.08	0.55	-0.22	0.32	-0.03	0.31	0.41	0.31
WTZR	49.1	-0.28	0.52	0.01	0.44	-0.19	0.41	-0.02	0.31	0.48	0.45
YELL	62.4	-0.20	0.39	-0.20	0.38	-0.18	0.31	-0.23	0.30	0.46	0.40
NYAL	78.9	-0.16	0.34	-0.07	0.35	-0.07	0.23	-0.10	0.25	0.63	0.71
Mean		0.00	0.53	-0.07	0.46	-0.13	0.44	-0.08	0.38	0.35	0.31
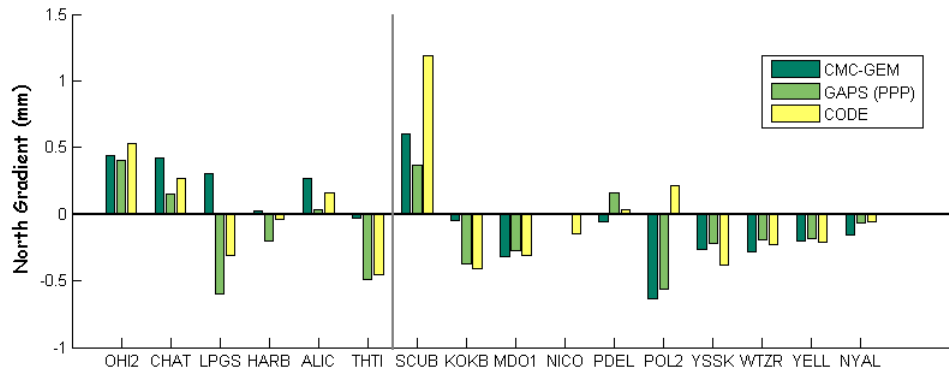
Figure 5.7: Mean north-south tropospheric gradients determined by GAPS (PPP), ray-tracing through CMC-GEM model and from CODE. Units of millimeters.

well between the three techniques although, unlike in the nouth-south case, the two GPS techniques do not always agree on the direction of the gradient. In Figure 5.7 it is possible to see the latitude dependence of the North-South gradient which is due to the temperature gradients existing as we move from the poles towards the equator Chen and Herring [1997].
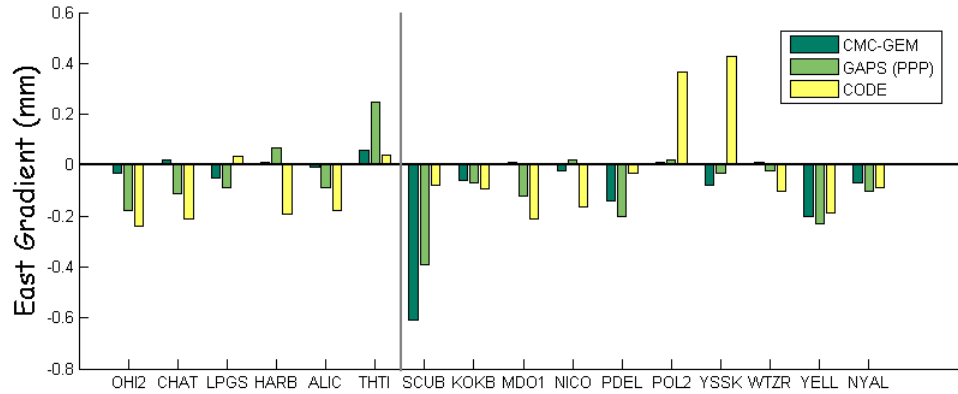
Figure 5.8: Mean east-west tropospheric gradients determined by GAPS (PPP), ray-tracing through CMC-GEM model and from CODE

The stations LPGS, HARB and THTI show agreement in the direction of the gradient between the two GPS techniques but an opposite direction for the ray-traced gradients. As the two GPS techniques agree, it would lead us to believe this may be a result of local weather anomalies which the NWM cannot detect, possibly due to the fewer number of observations in the southern hemisphere or due to the coarse resolution of the CMC-GEM analyses.

Overall the gradients agree relatively well. The application of high resolution weather models in areas where there was disagreement between the ray-traced and GPS derived gradients may help explain differences in the results. This is also a good reason for the inclusion of GPS derived quantities of water vapor into NWM analyses as they are able to add a lot of information concerning both the spatial and temporal resolution of water

vapor variations.

5.4.3   Effect of Estimating Troposphere Parameters on Convergence

The convergence time necessary to achieve cm level accuracy is one of the limiting factors of PPP [Bisnath and Gao, 2007]. The removal of the tropospheric parameters (residual zenith delay and gradient terms) from the design matrix could aid in reducing the convergence time of the solution while at the same time allow for mm level positioning in the horizontal domain and cm level positioning in the height domain.

To identify the impact of the different PPP strategies on convergence time, the convergence of the station position was studied. In all processing strategies, there were no constraints placed on the receiver coordinates, clock parameters or ambiguities. The residual zenith delay was constrained to 2 cm as ray-traced zenith delays were used and the gradient parameters were constrained to 1 cm.

In terms of position, we define convergence as, the time it takes for the 3D position solution to reach a threshold of 10 cm with respect to the final value. Convergence is only achieved when the solution no longer leaves this threshold.

Figure 5.9 show the percentage of solutions which have converged to the given threshold vs the number of epochs processed for each strategy. As the processing was performed at 5 minute intervals, each epoch represents 5 minutes. The results were unexpected as it was believed that the reduction in parameters of strategy 4 would improve the convergence of the solution. The poor convergence of strategy 4 is most likely due to errors in the modeling of the zenith non-hydrostatic delay which may cause more variation in the coordinates, especially in the up component. Both strategies which did not estimated the tropospheric gradients showed somewhat improved convergence, but after about 20 epochs, the advantage is negligible.

A number of factors are believed to have influenced the results. Ideally, kinematic

116
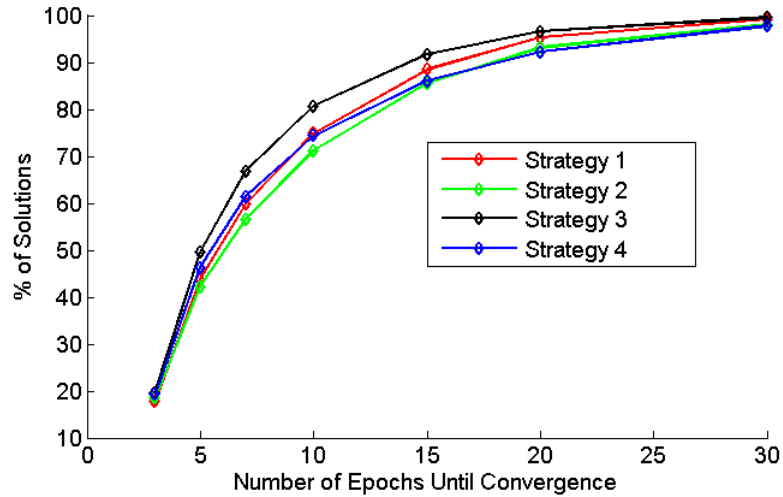
Figure 5.9: Convergence of the various strategies to 10 cm 3D position threshold. Each epoch represents 5 minutes.

processing would be used to study the convergence time, or short static sessions with an observation rate of 30 seconds. Secondly, as all techniques relied on ray-traced tropospheric delays, the initial a priori zenith delays were constrained tightly to 2 cm. It may have been more beneficial to include a strategy which only had available a climatology model to derive the a priori delays such as UNB3m [Leandro et al., 2007].

5.5   Summary

To summarize the results of this section: All strategies assessed in this chapter used the same PPP model and options including elevation cut-off angle, a priori zenith delays and stochastic models. The strategy of using the VMF1 hydrostatic and non-hydrostatic mapping functions, along with the estimation of a residual zenith delay and two gradient terms (strategy 2) and the use of the three dimensional ray-traced slant factors and estimated residual zenith delay (strategy 3) resulted in all most identical station repeatability in the horizontal component, while strategy 2 had an improvement of just over 1%.

117

Strategy 3 performed better than using only the VMF1 and not estimating any gradient parameters (Strategy 1) which implies that the three dimensional slant factors do represent real azimuth dependencies of the tropospheric delay. Finally, using only ray-traced zenith delays and slant factors performed almost equally as good as the other techniques in the horizontal components but suffered significantly in the up component. The precision of this strategy was shown to be a function of geographic location as well as containing a seasonal component which was in phase with the variation of water vapor content of the atmosphere.

The ray-traced non-hydrostatic delays were compared to the estimated zenith delays obtained from the PPP campaign. There was only a small bias of several millimeters between the two types of non-hydrostatic delays, although the ray-traced delays were not capable of modeling the variability of the GPS estimated delays which acted as truth.

The estimated gradients from strategy 2 were compared to gradients determined by ray-tracing though the CMC-GEM model. Overall, there was good agreement between the north-south gradients with only several exceptions. By comparing the results to gradients determined from CODE, it was believed these differences were due to the inability of the NWM to capture local variations in specific regions.

An attempt was made to assess the convergence properties of the various strategies. Due to the limitations in processing time it was difficult to draw any conclusions from this assessment. Recommendations were given on a possible experiment which could better assess the convergence properties of PPP under the various strategies.

Chapter 6

Conclusions

The objective of this dissertation, was to identify if there are any deficiencies in the current state-of-the-art tropospheric slant factor models which are currently in use for precise geodetic applications.

6.1 Summary

The current state-of-the-art models in use today for space geodetic positioning using radio signals were reviewed. Two experiments were undertaken spanning a full year, for twenty locations distributed globally which hoped to evaluate these models.

In the first experiment, ray-tracing was performed through three dimensional refractivity fields produced from the CMC-GEM global analyses consisting of nearly 5 million ray-traced observations taken at predefined azimuths and elevation angles. We began with an assessment on the current state-of-the-art mapping functions. It was found that the VMF1 produces the best results, introducing the smallest bias and producing the best repeatability out of all symmetric mapping functions currently in use. When it is not available, the GMF was found to be an excellent backup as it does not depend on any external

parameters yet is consistent with the VMF1, in that it would not cause a bias in the station position, but only cause an increase in the variability of the time series. A small, latitude dependence of the VMF1 was found, the cause of which was identified as the assumption of a spherical earth in the ray-tracing. The impact of this bias would be an error of 2 mm in the station height at the equator and at the poles, while mid-latitude stations would not experience any bias.

Several of the most popular symmetric functional formulations were evaluated. All of the symmetric functional formulations evaluated, with the exception of the *Davis* functional formulation, was capable of modeling the elevation dependence of the slant factors to less than 1 mm for all elevation angles down to three degrees. The addition of a fourth term to the Marini expression did yield some improvement, although it was not statistically significant at the 1σ level. Additionally, it was found that fitting all three coefficients of the Marini expression to the ray-traced slant factors was an improvement over the VMF parametrization. However, this improvement comes with a drawback of higher computation costs. Overall, it was found that the *Marini*3 coefficient expression is more than adequate to meet the demands for modeling the symmetric delay.

Asymmetric functional formulations were also assessed. The spherical harmonics of degree 2 and order 1 resulted in the smallest RMS for elevation angles between 5 and 20 degrees. The *Seko* functional formulation performed very well for extremely low elevation angles. Unfortunately, it is not practical to use these formulations when estimating gradients from space geodetic observations as the addition of up to 6 extra gradient coefficients would certainly hurt the other parameters of interest. For this purpose, linear horizontal gradient formulations are still necessary even though they have an increased RMS of the residuals. Out of the five possible options the Chen & Herring and the Meindl formulations performed the best. Some advantage was seen when estimating the gradient mapping function coefficient in the Chen & Herring formulation but even when using the

original values good results were achieved.

The estimation of the gradient mapping function coefficient in the Chen & Herring expression was also investigated. It was found that the new estimated coefficients agreed with the original values determined in Chen and Herring [1997] to within one standard deviation at the 1σ confidence level. A slight latitude dependence was seen, in both the value of the coefficient, but perhaps more importantly in the variability of the coefficient. For equatorial locations the variability of this coefficient was much larger. If a correlation could be found between the "C" coefficient and either a site or epoch specific parameter, it may potentially improve tropospheric gradient estimation.

In order to explain the benefits of the various asymmetric functional formulations it was attempted to characterize the variation of the asymmetric delay on a global basis. It was found that for the hydrostatic component, three distinct zones existed, a northern latitude zone, an equatorial zone and a southern latitude zone. Both the northern and southern zone experienced mean gradients which exhibited a single minimum and maximum, and were out of phase by approximately $180°$, in azimuth, with each other. Surprisingly the equatorial zone exhibited a bi-modal variation with respect to azimuth which to this authors knowledge has not been identified before. In each zone, the azimuth dependence is caused by temperature and atmosphere thickness gradients which are in general inclined towards the poles. For the non-hydrostatic component the variations do not exhibit as strong a latitude dependence as they are more susceptible to local climatic processes. Several stations in particular showed excellent examples of the impact of local conditions such as topography.

The second experiment performed consisted of a global PPP campaign to assess the benefit of using the three dimensional ray-traced slant factors at the observation level. Four strategies were compared including: VMF1 with estimation of a residual zenith delay, VMF1 with estimation of residual zenith delay and two gradient parameters, ray-traced

slant factors and estimation of a residual zenith delay and ray-traced slant factors with no estimation of tropospheric parameters.

Unlike past approaches to applying ray-tracing at the observation level, a new approach of using slant factors which can be applied in a similar manner as current mapping functions was described and implemented. This approach eliminates the need to adjust the stochastic estimation and allows for the software to directly output the total zenith delay (predicted+estimated). Also it would allow for the use of other external a priori zenith delay calibration techniques which may prove beneficial.

It was found that all approaches resulted in sub-centimeter repeatability in the horizontal component. However, the strategies which accounted for both a residual zenith delay and the asymmetry of the tropospheric delay, whether by estimation or by three dimensional ray-tracing, gave the best repeatability. In the up direction, the use of only ray-traced zenith delays had repeatabilities almost four as large as the other techniques. The estimation of tropospheric gradients resulted in the best repeatability, with a 1% improvement over the use of ray-traced slant factors and an improvement of nearly 9% over the use of only VMF1 and ignoring the asymmetry of the troposphere. The good performance of the ray-traced slant factors does justify its use as a means of modeling the asymmetry of the tropospheric delay.

A comparison between the troposphere products derived from ray-tracing and those derived from the GPS observations were performed. The non-hydrostatic zenith delays obtained by ray-tracing through the CMC-GEM were compared to the estimated zenith delays obtained from the PPP campaign. Overall a small bias of 3 mm was found with a standard deviation of 15 mm at the 1σ level. Typically the ray-traced delay was larger than the estimated delay.

Next the total north-south and east-west gradients estimated from the ray-traced slant factors were compared to the gradients estimated from the GPS observations. The ray-

traced gradients agreed well in direction, particularly in the North-South component, while some differences were seen in the East-West component. This is mainly believed to be due to the difficulty of the NWM in modeling small scale phenomenon in the water vapor distribution. Overall, the correlation between the PPP gradients and the ray-traced gradients was 32% for both the north-south and east-west components which shows moderate agreement between the techniques.

An assessment on the convergence time of the four solutions was also performed. Very little difference was found and was most likely due to the processing strategy employed in the PPP campaign such as the a priori constraints and observation rate. Recommendations for a future comparison are outlined and this would most likely be able to clarify the results.

6.2 Recommendations

The following, are recommendations which have stemmed from the work presented in this thesis.

- Mapping Functions: The VMF1 should be used for all geodetic applications as it agrees best with the three dimensional ray-tracing. The GMF can be used as a backup without introducing a significant bias into the station position. A small latitude bias was found with respect to the hydrostatic ray-traced slant factors which warrants further study as to the impact in the position domain.

- The Marini 3 coefficient expression is capable of modeling the elevation dependence of both the hydrostatic and non-hydrostatic slant factors down to the $3°$ elevation angle with sub-millimeter accuracy. This, along with its convenient closed form, makes it our recommendation as the functional formulation for the development of future symmetric mapping functions.

- Higher-order asymmetric functional formulations such as spherical harmonics of higher order polynomials, may provide a means of providing closed-form expressions for describing the azimuth dependence of the tropospheric delay. Their use for the estimation of tropospheric parameters from geodetic observation may be somewhat limited.

- For the purpose of estimating gradients using space geodetic observations, the linear horizontal gradient formulations of Chen & Herring and Meindl are recommended. A small improvement could be possible by finding an analytical form to describe the variation of the C parameter in the Chen & Herring gradient mapping function.

For positioning purposes:

- The VMF1 along with the estimation of a residual zenith delay and two gradient parameters provides the best repeatability in the station time series although it showed only a small improvement over the ray-traced slant factors with an estimated residual zenith delay.

- Ray-traced zenith delays without estimation of any residual tropospheric delay parameters can provide sub- centimeter level precision in the horizontal components, and centimeter level precision in the vertical component.

6.3 Future Work

Mapping Functions Although the VMF1 did not introduce a significant bias into the solutions, the non-hydrostatic variability is still quite high. Further work could be performed to find if an improvement in the position domain can be gained by fitting all three coefficient of the Marini expression.

A slight latitude dependence was found whose cause was identified to be the simplification of the shape of the earth to a constant sphere. Although the impact on the position domain may not be significant, it will be important to study the effect this bias has on the position domain.

Symmetric Functional Formulation Evaluation   The symmetric functional formulations were shown to be ideal candidates for future mapping functions. The estimation of the three coefficients was shown to be beneficial in terms of reducing the variability of the differences between the three dimensional ray-tracing and the functional formulations. This benefit may or may not have an impact on the position domain.

Asymmetric Functional Formulation Evaluation   The asymmetric functional formulations evaluated in this work used an evenly distributed observation scheme covering the entire sky. In reality, if these functional formulations are used to estimate gradient terms from space geodetic techniques, the distribution is much less homogenous and the number of low elevation angle observation much fewer. Work should be carried out to assess the performance of these formulations under realistic constellations.

No attempt was made to characterize the change in the gradients over time, both on short time scales sub-daily, and on long time scales, annually and longer. Identifying how the gradients change over time will aid in the estimation of gradients using space geodetic observations and therefore should be studied further.

Ray-tracing at the Observation Level   Ray-tracing at the observation level is still in its infancy. As the resolution and accuracy of the NWM improves, we will see additional benefit. For this study the NWM were provided on a 3 hour basis, with initializations every 12 hours. This may not be enough to properly model the variation of the slant factors over time. Therefore, NWM with higher temporal and spatial resolution should be studied.

The need for improved stochastic modeling, both in terms of the space geodetic observations and the ray-traced observations is necessary. As we seek to use lower elevation angle cutoffs by improving the modeling of the slant factors at low elevation angles, the observation weighting must also be adjusted to reflect this improvement. Additionally, the correlations between the ray-traced slant factors can be quite large and are likely a function of the grid resolution of the NWM. In order to prevent over optimistic formal errors, these correlations should be considered.

Although reasonable agreement was found between the ray-traced gradients and the estimated gradients in PPP and from CODE, further work needs to go into identifying the cause of the differences. Some progress has already been made on this topic from various groups around the world, but especially on the ray-tracing side of things more work needs to be done.

The use of ray-traced zenith delays for positioning purposes showed promise and may be beneficial in some applications. However, as was shown there are times when the ray-traced zenith delays can vary quite significantly. Ideally, if either ray-traced zenith delays or slant factors are to be used for positioning purposes, a quality indicator of the expected accuracy of the products would be necessary.

References

Bean, R., and E. Dutton (1966). "Radio meteorology." *NBS Monograph Series*, Vol. 92, p. 435.

Bevis, M., S. Businger, S. Chiswell, T. A. Herring, R. A. Anthes, C. Rocken, and R. H. Ware (1994). "GPS Meteorology: Mapping zenith wet delays onto precipitable water." *Journal of Applied Meteorology*, Vol. 33, No. 3, pp. 379–386.

Bisnath, S., and Y. Gao (2007). "Current state of precise point positioning and future prospects and limitations." *Earth: Our Changing Earth — IUGG XXIV General Assembly*, International Union of Geodesy and Geophysics, Perugia, Italy, July 2–13.

Blewitt, G. (1989). "Carrier phase ambiguity resolution for the Global Positioning System applied to geodetic baselines up to 2000 km." *Journal of Geophysical Research*, Vol. 94, No. B8, pp. 10–187.

Bock, O., J. Tarniewicz, C. Thom, J. Pelon, and M. Kasser (2001). "Study of external path delay correction techniques for high accuracy height determination with gps." *Physics and Chemistry of the Earth, Part A: Solid Earth and Geodesy*, Vol. 26, No. 3, pp. 165 – 171, `doi:DOI: 10.1016/S1464-1895(01)00041-2`.

Boehm, J., J. Kouba, and H. Schuh (2008). "Forecast vienna mapping functions 1 for real-time analysis of space geodetic observations." *Journal of Geodesy*, Vol. 83, No. 5, pp. 397–401, `doi:10.1007/s00190-008-0216-y`.

Boehm, J., A. E. Niell, P. Tregoning, and H. Schuh (2006a). "Global Mapping Function (GMF): A new empirical mapping function based on numerical weather model data." *Geophysical Research Letters*, Vol. 33, No. L07304, `doi:10.1029/2005GL025546`.

Boehm, J., and H. Schuh (2003). "Vienna Mapping Functions." *Proceedings of the 16th Working Meeting on European VLBI for Geodesy and Astrometry*, eds. W. Schwegmann, and V. Thorandt, Bundesamt für Kartographie und Geodäsie, Verlag des Bundesamtes für Kartographie und Geodäsie, Frankfurt/Leipzig, Germany, May 9–10, pp. 131–144. `http://www.hg.tuwien.ac.at/Archiv/Papers/2003_16thEuVLBI_boehm_pa_a.pdf`.

Boehm, J., B. Werl, and H. Schuh (2006b). "Troposphere mapping functions for GPS and very long baseline interferometry from European Centre for Medium-Range Weather Forecasts operational analysis data." *Journal of Geophysical Research*, Vol. 111, No. B02406, `doi:10.1029/2005JB003629`.

Böhm, J., and H. Schuh (2001). "Spherical harmonics as a supplement to global tropospheric mapping functions and horizontal gradients." *Proceedings of the 15th Working Meeting on European VLBI for Geodesy and Astrometry*, eds. D. Behrend, and A. Rius, Institut d'Estudis Espacials de Catalunya, Barcelona, Spain, September 7–8, pp. 143–148. `ftp://io.ieec.fcr.es/ieec/gps/15wmevga/pdf/boehm.pdf`.

Böhm, J., and T. VanDam (2009). "Modeling deficiencies and modeling based on external data." Second GGOS Unified Analysis Workshop, IERS, Grand Hyatt, San Francisco, CA, USA, December 11–12. (Oral presentation).

Born, M., and E. Wolf (1999). *Principles of Optics: Electromagnetic Theory of Propagation, Interference and Diffraction of Light*. 7th ed., 986 pp., Cambridge University Press, Cambridge, U.K., ISBN 0521642221, `doi:10.2277/0521642221`.

Chandra, S., E. L. Fleming, M. R. Schoeberl, and J. J. Barnett (1990). "Monthly mean global climatology of temperature, wind, geopotential height and pressure for 0–120 km." *Advances in Space Research*, Vol. 10, No. 6, pp. 3–12, `doi:10.1016/0273-1177(90)90230-W`.

Chao, C. (1972). "A model for tropospheric calibration from daily surface and radiosonde balloon measurements." Technical Memorandum, California Institute of Technology, Jet Propulsion Laboratory, Pasadena, Calif., 17 pp.

Chao, C. (1974). "The tropospheric calibration model for mariner mars 1971." Technical Report 32–1587, California Institute of Technology, Jet Propulsion Laboratory, Pasadena, Calif., 17 pp.

Chen, G., and T. A. Herring (1997). "Effects of atmospheric azimuth asymmetry on the analysis of space geodetic data." *Journal of Geophysical Research*, Vol. 102, No. B9, pp. 20489–20502, `doi:10.1029/97JB01739`.

COESA (1962). "U.S. Standard Atmosphere, 1962 — ICAO standard atmosphere to 20 kilometers, proposed ICAO extension to 32 kilometers, tables and data to 700 kilometers." U.S. Government Printing Office, United States Committee on Extension to the Standard Atmosphere (COESA), National Aeronautics and Space Administration, United States Air Force, United States Weather Bureau, Washington, D.C., December, 278 pp., `http://handle.dtic.mil/100.2/AD659893`.

COESA (1976). "U.S. Standard Atmosphere, 1976." U.S. Government Printing Office NOAA–S/T 76–1562, United States Committee on Extension to the Standard Atmosphere (COESA), National Oceanic and Amospheric [sic] Administration, National

Aeronautics and Space Administration, United States Air Force, Washington, D.C., October, 227 pp., `http://hdl.handle.net/2060/19770009539`.

COMET-UCAR (1999). "NWP model fundamentals.", University Corporation for Atmospheric Research (UCAR), Cooperative Program for Operational Meteorology, Education and Training (COMET), (Lecture Notes), `http://www.meted.ucar.edu/topics_nwp.php`.

of Congress, L. (1997). *Kazakstan, Kyrgyzstan,Tajikistan, Turkmenistan, and Uzbekistan:Country Studies*. 1st ed., 570 pp., Library of Congress: A Federal Research Division, Washington, DC.

Cove, K. (2005). *Improvements in GPS Tropospheric Delay Estimation with Numerical Weather Prediction*. M.Sc.E. thesis, University of New Brunswick, Dept. of Geodesy and Geomatics Engineering, Fredericton, N.B., Canada, May, 98 pp., Technical Report 230, `http://gge.unb.ca/Pubs/TR230.pdf`.

Davis, J. L., G. Elgered, A. E. Niell, and C. E. Kuehn (1993). "Ground-based measurement of gradients in the "wet" radio refractivity of air." *Radio Science*, Vol. 28, No. 6, pp. 1003–1018, `doi:10.1029/93RS01917`.

Davis, J. L., T. A. Herring, I. I. Shapiro, A. E. E. Rogers, and G. Elgered (1985). "Geodesy by radio interferometry: Effects of atmospheric modeling errors on estimates of baseline length." *Radio Science*, Vol. 20, No. 6, pp. 1593–1607, `doi:10.1029/RS020i006p01593`.

Dietterich, T. (1998). "Approximate statistical tests for comparing supervised classification learning algorithms." *Neural Computation*, Vol. 10, No. 7, pp. 1895–1923.

Eresmaa, R., M. Nordman, M. Poutanen, J. Syrjärinne, J. Luntama, and H. Järvinen (2008). "Parameterization of tropospheric delay correction for mobile gnss positioning: a case study of a cold front passage." *Meteorological Applications*, Vol. 15, No. 4, pp. 447–454.

Gaffen, D., A. Robock, and W. Elliott (1992). "Annual cycles of tropospheric water vapor." *Journal of Geophysical Research*, Vol. 97, p. 18.

Ghoddousi-Fard, R., and P. Dare (2007). "A climatic based asymmetric mapping function using a dual radiosonde raytracing approach." *Proceedings of the 20th International Technical Meeting of the Satellite Division of the Institute of Navigation — ION GNSS 2007*, The Institute of Navigation, Fort Worth, Tex., September 25–28, pp. 2870–2879.

Ghoddousi-Fard, R., P. Dare, and R. Langley (2009a). "A web-based package for ray tracing the neutral atmosphere radiometric path delay." *Computers & Geosciences*, Vol. 35, No. 6, pp. 1113–1124.

Ghoddousi-Fard, R., P. Dare, and R. Langley (2009b). "Tropospheric delay gradients from numerical weather prediction models: effects on gps estimated parameters." *GPS Solutions*, Vol. 13, pp. 281–291.

Gill, M., W. Murray, and W. M. (1981). *Practical optimization*. 401 pp., Academic Press, London, U.K., ISBN 0-12-283952-8.

Hastie, T., R. Tibshirani, and J. Friedman (2008). *The Elements of Statistical Learning: Data Miniing, Inference, and Prediction*. 764 pp., Springer, New York.

Herring, T. A. (1992). "Modelling atmospheric delays in the analysis of space geodetic data." In de Munck and Spoelstra [1992], pp. 157–164.

Hobiger, T., R. Ichikawa, Y. Koyama, and T. Kondo (2008a). "Fast and accurate ray-tracing algorithms for real-time space geodetic applications using numerical weather models." *Journal of Geophysical Research*, Vol. 113, No. D20, `doi:10.1029/2008JD010503`.

Hobiger, T., R. Ichikawa, T. Takasu, Y. Koyama, and T. Kondo (2008b). "Ray-traced troposphere slant delays for precise point positioning." *Earth, Planets and Space*, Vol. 60, No. 5, pp. e1–e4, `http://www.terrapub.co.jp/journals/EPS/pdf/2008e/6005e001.pdf`.

Hobiger, T., S. Shimada, R. Ichikawa, Y. Koyama, and T. Kondo (2010). "Improving gps positioning estimates during extreme weather situations by the help of fine -mesh numerical weather models." *Journal of Atmospheric and Solar-Terrestrial Physics*, Vol. 72, No. 2–3, pp. 262–270, `doi:10.1016/j.jastp.2009.11.018`.

Ichikawa, R., T. Hobiger, Y. Koyama, and T. Kondo (2008). "An Evaluation of the Practicability of Current Mapping Functions using Ray-traced Atmosphere Slant Delays from JMA Mesoscale Numerical Weather Data." *AGU Fall Meeting Abstracts*, pp. A612+.

Ifadis, I. M. (2000). "A new approach to mapping the atmospheric effect for GPS observations." *Earth, Planets and Space*, Vol. 52, No. 10, pp. 703–708, `http://www.terrapub.co.jp/journals/EPS/pdf/5210/52100703.pdf`.

Janes, H., R. Langley, and S. Newby (1991). "Analysis of tropospheric delay prediction models: Comparisons with ray-tracing and implications for gps relative positioning." *Bulletin Géodésique*, Vol. 65, No. 3, pp. 151–161.

Jensen, A. B. O. (2005). "Numerical weather predictions for GPS positioning." In *A Window on the Future of Geodesy — Proceedings of the IAG 2003 General Assembly, Sapporo, Japan, June 30 – July 11*, ed. F. Sansò, Vol. 128 of *International Association of Geodesy Symposia*, Springer, Berlin, ISBN 978-3-540-24055-6, pp. 65–70, `doi:10.1007/3-540-27432-4_12`.

Johnson, D. L., B. C. Roberts, and W. W. Vaughan (2002). "Reference and standard atmosphere models." *10th Conference on Aviation, Range, and Aerospace Meteorology*, Portland, Oreg., May 13–16. `http://hdl.handle.net/2060/20020092087`.

Kouba, J. (2008). "Implementation and testing of the gridded Vienna Mapping Function 1 (VMF1)." *Journal of Geodesy*, Vol. 82, No. 4, pp. 193–205, `doi:10.1007/s00190-007-0170-0`.

Kouba, J. (2009). "A guide to using international gnss service (igs) products." Report, Geodetic Survey Division, Natural Resources Canada, Ottawa,Ontario, May, `http://acc.igs.org/UsingIGSProductsVer21.pdf`.

Kouba, J., and P. Héroux (2001). "Precise point positioning using IGS orbit and clock products." *GPS solutions*, Vol. 5, No. 2, pp. 12–28.

Laroche, S. (n.d.). "Data assimilation cycles at the canadian meteorological centre." (Online), Canadian Meteorological Centre. `http://collaboration.cmc.ec.gc.ca/cmc/cmoi/product_guide/docs/lib/cycle_en.pdf`

Leandro, R. F., M. C. Santos, and R. B. Langley (2007). "GAPS: The GPS analysis and positioning software – a brief overview." *Proceedings of the 20th International Technical Meeting of the Satellite Division of the Institute of Navigation — ION GNSS 2007*, The Institute of Navigation, Fort Worth, Tex., September 25–28, pp. 1807–1811. `http://gauss.gge.unb.ca/papers.pdf/iongnss2007.leandro.gaps.pdf`.

Lemoine, F. G., S. C. Kenyon, J. K. Factor, R. Trimmer, N. K. Pavlis, D. S. Chinn, C. M. Cox, S. M. Klosko, S. B. Luthcke, M. H. Torrence, Y. M. Wang, R. G. Williamson, E. C. Pavlis, R. H. Rapp, and T. R. Olson (1998). "The development of the joint NASA GSFC and the National Imagery and Mapping Agency NIMA geopotential model EGM96." TP 1998-206861, NASA Goddard Space Flight Center, Greenbelt, Md., July, 575 pp., `http://hdl.handle.net/2060/19980218814`.

MacMillan, D., and J. Gipson (2009). "Recent modeling improvements in solve analysis." 19th European VLBI for Geodesy and Astronomy Working Meeting, Bordeaux, FR, March24–25.

MacMillan, D. S. (1995). "Atmospheric gradients from very long baseline interferometry observations." *Geophysical Research Letters*, Vol. 22, No. 9, pp. 1041–1044.

Marini, J. W. (1972). "Correction of satellite tracking data for an arbitrary tropospheric profile." *Radio Science*, Vol. 7, No. 2, pp. 223–231, `doi:10.1029/RS007i002p00223`.

Mathworks (2010). "Levenberg-marquardt method." (Online), R2010b Documentation — Optimization Toolbox. `http://www.mathworks.com/help/toolbox/optim/ug/brnoybu.html#f204`

McCarthy, D. D., and G. Petit (Eds.) (2004). *IERS Conventions (2003)*. 127 pp., Frankfurt am Main: Verlag des Bundesamts für Kartographie und Geodäsie, Frankfurt, ISBN 3-89888-884-3, IERS Technical Note 32, `http://www.iers.org/MainDisp.csl?pid=46-25776`.

Meindl, M., S. Schaer, U. Hugentobler, and G. Beutler (2004). "Tropospheric gradient estimation at code: Results from global solutions." *Journal of the Meteorological Society of Japan*, Vol. 82, No. 1 B, pp. 331–338, cited By (since 1996) 6. `http://www.scopus.com/inward/record.url?eid=2-s2.0-2942527021&partnerID=40&md5=d9f2508d6ca24c65e157dfc1c5a9abf2`

Mendes, V. B. (1999). *Modeling the Neutral-Atmosphere Propagation Delay in Radiometric Space Techniques*. Ph.D. thesis, University of New Brunswick, Dept. of Geodesy and Geomatics Engineering, Fredericton, N.B., Canada, April, 349 pp., Technical Report 199, `http://gge.unb.ca/Pubs/TR199.pdf`.

More, J. (1978). "The Levenberg-Marquardt algorithm: implementation and theory." *Numerical analysis*, pp. 105–116.

de Munck, J. C., and T. A. TH. Spoelstra (Eds.) (1992). *Proceedings of the Symposium Refraction of Transatmospheric Signals in Geodesy*, No. 36, Netherlands Geodetic Commission, The Hague, The Netherlands, May 19–22, 197 pp.

Niell, A. E. (1996). "Global mapping functions for the atmosphere delay at radio wavelengths." *Journal of Geophysical Research*, Vol. 101, No. B2, pp. 3227–3246, `doi:10.1029/95JB03048`.

Niell, A. E. (2000). "Improved atmospheric mapping functions for vlbi and gps." *Earth, Plant and Space*, Vol. 52, No. 10, pp. 699–702.

Niell, A. E. (2003). "The IMF mapping functions." *International Workshop on GPS Meteorology*, Tsukuba, Japan, January 14–17, p. 10. `http://www.haystack.mit.edu/geo/pubs/the_imf_mapping_functions_rev2.pdf`.

Nievinski, F. G. (2006). "Numerical weather models for tropospheric mitigation in marine kinematic GPS: A daylong analysis." *Proceedings of the 19th International Technical Meeting of the Satellite Division of the Institute of Navigation — ION GNSS 2006*, The Institute of Navigation, Fort Worth, Tex., September 26–29, pp. 2017–2026, (student paper award). `http://gge.unb.ca/Research/GRL/PrincessOfAcadia/Publications/NievinskiIONGNSS2006.pdf`.

Nievinski, F. G. (2009). *Ray-tracing Options to Mitigate the Neutral Atmosphere Delay in GPS*. M.Sc.E. thesis, University of New Brunswick, Dept. of Geodesy and Geomatics Engineering, Fredericton, N.B., Canada, May, 232 pp., Technical Report 262, `http://gge.unb.ca/Pubs/TR262.pdf`.

Nievinski, F. G., L. Urquhart, and M. C. Santos (2008). "Impact of mapping functions based on spherical, ellipsoidal, gradient, and 3d atmospheric structures on GPS Precise Point Positioning." Fall Meeting 2008, American Geophysical Union, San Francisco, Calif., December 15–19, Eos Trans. AGU Fall Meet. Suppl., Abstract G41A-0611. (Poster presentation).

Nifisi, V. (2010). Personal communication. Institute of Geodesy and Geophysics,Technical University of Vienna, Vienna, Austria.

Nifisi, V., L. Urquhart, and J. Boehm (2010). "First results of the benchmarking campaign." Workshop on Ray-tracing for Geodetic Space Techniques, IAG Working Group 4.3.3, Vienna, Austria, April 29–30. (Oral presentation).

Nocedal, J., and S. Wright (2006). *Numerical Optimization*. 664 pp., Springer Science + Buisness Media, LLC, New York, U.S.A., ISBN 10:0-387-30303-0.

Nordman, M., R. Eresmaa, J. Boehm, M. Poutanen, H. Koivula, and H. Järvinen (2009). "Effect of troposphere slant delays on regional double difference gps processing." *Earth, planets and space*, Vol. 61, No. 7, pp. 845–852.

OFCM (2007). "Rawinsonde and pibal observations." In *Federal Meteorological Handbook No. 3*, Office of the Federal Coordinator for Meteorology, Silver Spring, Md., FCM-H3-1997, `http://www.ofcm.gov/fmh3/fmh3.htm`.

Overton, M. (2001). *Numerical computing with IEEE floating point arithmetic*. 1st ed., 104 pp., Society for Industrial and Applied Mathematics, Philidelphia, U.S.A, ISBN 0-89871-571-7.

Pany, A., J. Böhm, and H. Schuh (2010). "Ray-traced delays for the improvement of troposphere delay modelling in vlbi." Ray-tracing Workshop, Institute of Geodesy and Geophysics, Technical University of Vienna, Vienna,AU, April28–29. (Oral presentation).

Pany, A., J. Böhm, H. Schuh, T. Hobiger, and R. Ichikawa (2009). "Modeling azimuthal asymmetries of the troposphere delay during a 14-days typhoon period in tsukuba." *Proceedings of the 19th European VLBI for Geodesy and Astrometry Working Meeting*, Universite Bordeaux, March 24–25, pp. 44–48.

Petrov, L., and J. P. Boy (2004). "Study of the atmospheric pressure loading signal in very long baseline interferometry observations." *Journal of Geophysical Research*, Vol. 109, No. B03405, `doi:10.1029/2003JB002500`.

Picard, R., and D. Cook (1984). "Cross-validation of regression models." *Journal of the Americal Statistical Association*, Vol. 79, No. 387, pp. 575–583.

Rocken, C., S. Sokolovskiy, J. M. Johnson, and D. Hunt (2001). "Improved mapping of tropospheric delays." *Journal of Atmospheric and Oceanic Technology*, Vol. 18, No. 7, pp. 1205–1213, `doi:10.1175/1520-0426(2001)018<1205:IMOTD>2.0.CO;2`.

Rothacher, M., S. Schaer, L. Mervart, and G. Beutler (1995). "Determination of antenna phase center variations using gps data." *Proc 1995 IGS Workshop*, pp. 205–220.

Rüeger, J. M. (2002). "Refractive index formulae for radio waves." *FIG XXII International Congress*, International Federation of Surveyors (FIG), Washington, D.C., April 19–26. `http://www.fig.net/pub/fig_2002/Js28/JS28_rueger.pdf`.

Saastamoinen, J. (1972). "Atmospheric correction for the troposphere and stratosphere in radio ranging of satellites." In *The Use of Artificial Satellites for Geodesy*, eds. S. W. Henriksen, A. Mancini, and B. H. Chovitz, Vol. 15 of *Geophysical Monograph Series*, American Geophysical Union, Washington, D.C., ISBN 0-87590-015-1, pp. 247–251.

Seko, H., H. Nakamura, and S. Shimada (2004). "An evaluation of atmospheric models for GPS data retrieval by output from a numerical weather model." *Journal of the Meteorological Society of Japan*, Vol. 82, No. 1B, pp. 339–350, `doi:10.2151/jmsj.2004.339`.

Steigenberger, P. (2010). Personal communication. Technical University of Munich, Munich, Germany, Munich, Germany.

Steigenberger, P., J. Boehm, and V. Tesmer (2008). "Comparison of GMF/GPT with VMF1/ECMWF and implications for atmospheric loading." *Journal of Geodesy*, (submitted).

Thessin, R. N. (2005). *Atmospheric signal delay affecting GPS measurements made by space vehicles during launch, orbit and reentry*. Master's thesis, Massachusetts Institute of Technology, Dept. of Aeronautics and Astronautics, Cambridge, Mass., 182 pp., `http://hdl.handle.net/1721.1/33211`.

Torge, W. (2001). *Geodesy*. 3rd ed., 416 pp., de Gruyter, Berlin, ISBN 978-3-11-017072-6, compl. rev. and extend. ed.

Treuhaft, R. L. (1992). "Tropospheric and charged particle propagation errors in very long baseline interferometry." In de Munck and Spoelstra [1992], pp. 45–53.

Urquhart, L. (2009). "Atmospheric pressure loading and its effects on precise point positioning." *Proceedings of the 22nd International Technical Meeting of the Satellite Division of the Institute of Navigation — ION GNSS 2009*, The Institute of Navigation, Savannah, Ga., September 22–25, pp. 658–667, (student paper award).

Urquhart, L., F. G. Nievinski, and M. C. Santos (2010). "Evaluation of different strategies for mitigating azimuthally asymmetric tropospheric delays." European Geosciences

Union General Assembly 2010, EGU, Vienna, Austria, May 02–07. (Poster presentation).

Ware, R., J. Braun, S. Ha, D. Hunt, Y. Kuo, C. Rocken, M. Sleziak, T. Van Hove, J. Weber, and R. Anthes (2000). "REAL-TIME WATER VAPOR SENSING WITH SUOMINET–TODAY AND TOMORROW." *Bull. Am. Met. Soc*, Vol. 81, pp. 677–694.

Yan, H., and J. Ping (1995). "The generator function method of the tropospheric refraction corrections." *The Astronomical Journal*, Vol. 110, No. 2, pp. 934–939, `doi:10.1086/117574`.

Yunck, T. P. (1993). "Coping with the atmosphere and ionosphere in precise satellite and ground positioning." *Geophysical Monograph 73*, International Union of Geodesy and Geophysics, Washingtion, DC/Brussels, Belgium, mar, pp. 1–16.

Zumberge, J., M. Heflin, D. Jefferson, M. Watkins, and F. Webb (1997). "Precise point positioning for the efficient and robust analysis of GPS data from large networks." *Journal of Geophysical Research*, Vol. 102, No. B3, pp. 5005–5017.

Appendices

Appendix I

Cross Validation

Ideally, when fitting a model to a set of data, the entire data set would be available. However, this is rarely true. In the case of slant factor modeling, we need to balance the number of observations taken at each station and epoch, with our ability to generate a time series of significant length from which we can draw statistical conclusions about the performance of each model over a wide range of stations and seasonal periods.

Let $\mathscr{D}$ be the full set of observations taken at all possible azimuths between $0°$ and $360°$ and elevation angles between $3°$ and zenith. The problem at hand is how to obtain the predicted accuracy of a fitted model, $f(\boldsymbol{x})$, for the entire set, $\mathscr{D}$, only using a subset of observations, $\mathscr{D}_s$, taken at discrete azimuths and elevation angles.

Consider a model, $f(\boldsymbol{x})$, fit to the subset $\mathscr{D}_{sub} \in \mathscr{D}$. The predicted error of the model for the subset is:

$$Err_{\mathscr{D}_{sub}} = E[L(\boldsymbol{Y}, \hat{f}(\boldsymbol{X}))|\mathscr{D}_{sub}], \tag{I.1}$$

where $L(\boldsymbol{Y}, \hat{f}(\boldsymbol{X}))$ is the loss function, which is a measure of the error between the observations $\boldsymbol{Y}$ and the model $f(\boldsymbol{X})$. In our case since we are using the least squares criterion, the loss function is given by, the least squares criterion:

$$\boldsymbol{F}(\boldsymbol{x}) = \sum_{i=1}^{n} [y_i - f(x_i)]^2, \tag{I.2}$$

$Err_{\mathscr{D}_{sub}}$ is an unbiased estimate of the predicted error of the fitted model for the observations $\mathscr{D}_{sub}$, this is, in general, not the case when the estimated parameters $\boldsymbol{X}_{sub}$ determined from the subset are applied to the full set of observations $\mathscr{D}_{full}$, which when working with noisy data or non-parametric models is due to over-fitting [Hastie et al., 2008].

Although over-fitting is not generally a concern for slant factor modeling, as the general behavior of the slant factors with respect to elevation angles can be very well represented by a continued fraction form of $1/\sin(\varepsilon)$ and most functional formulations are of low order, an experiment was devised to test if the predicted error obtained fitting a subset of observations to the functional formulations would be a good representation of the error of that model over the entire set.

Cross validation (CV) is a statistical technique used for evaluating how a fitted model will perform when used on an independent set. In this particular case, we have functional formulations which are being fit to a subset of observations and we are extrapolating the performance statistics to evaluate how the formulations would perform on the full set of observations made over any portion of the sky. Several of the more popular cross validation techniques include: leave one out, $n \times 2$-fold and n-fold.

Ideally, we would have a sufficiently large data set so that a validation set could be set aside (hold-out validation) and be used as an independent assessment of the model's performance. This was achieved by ray-tracing on a very dense grid of observations on a $1° \times 1°$ grid over the entire sky (360 degrees in azimuth, and from 3 degrees to 90 degrees in elevation angle). The ray-tracing was performed using a high resolution NWM from the ECMWF for a single epoch (2008/08/12) and a single station (TSUK, Japan).

From these observations three data sets were created as follows:

Set A: All 31,320 observations

Set B: Fitting set: Actual observation scheme (324 observations), every 10 degrees in azimuth and elevation angles:3°, 5°, 7°, 10°, 14°, 20°, 40°, 70°, and zenith.

Set C: Hold-out set: Union of set B and set C = set A

k-fold Cross Validation: For the k-fold technique, the data is first randomly divided into k subsets, also called folds, of approximately the same size. k iterations are performed, each time holding out a single fold to act as validation data, while the remaining k-1 folds are used as training data. For each iteration, prediction error is computed as:

$$Err_{\mathscr{D}_s} = \frac{1}{k} \sum_{i=1}^{k} \boldsymbol{y}_i - \hat{\mathrm{f}}^{-\mathrm{k}(\mathrm{i})}(\boldsymbol{x}_i), \tag{I.3}$$

where $\boldsymbol{y}_i$ are the test observations, $\mathrm{f}^{-\mathrm{k}(\mathrm{i})}(\boldsymbol{x}_i)$ is the fitted model computed with the kth part of the data removed, evaluated at the test points ($\boldsymbol{x}_i$).

Typical values for k are between 5 and 10. A drawback of this approach is that each training set shares 80% of the data. This can introduce a correlation between the runs which can lead to erroneous conclusions about the performance of the fitted model Dietterich [1998].

Leave-one-out: Leave one out cross validation is simply a special case of the k-fold technique whereby k equals the number of observations. In this way, only a single observation is withheld at any given time, and the $n - 1$ observations are used to fit the model. This approach is usually not chosen as it can be very computationally demanding.

Repeated k-fold To overcome the problem of the k-fold technique described above, Dietterich [1998] found that this could be diminished by increasing the number of estimates of the loss function. One way to do this is to perform a single k-fold run as described

139

above, but then reshuffle the folds and perform a second k-fold run. This attempts to achieve the best qualities of both the k-fold and leave one out techniques; namely many estimates of the loss function, but without the high computation times.

Each of the three cross validation techniques were performed using set B on various functional formulations assessed in this work. The goal of the CV techniques is to obtain the true error ($Err_{\mathcal{D}_{full}}$) but only using the subset of observations from set B. As an alternative we can also simply use the residuals of the least squares fit of the functional formulation to the subset of observations to predict the true error. According to CV theory, this options should result in an optimistic prediction of the true error.

The true error, $Err_{\mathcal{D}_{full}}$, is computed by fitting the functional formulations to set B, but then apply the estimated parameters to the hold out set C. As this is the independent set this will be the best prediction of the true error of the functional formulation.

Figures I.1 and I.2 show the difference in the mean bias between the four validation techniques and the true error of the functional formulation for the hydrostatic slant factors(Figure I.1) and the non-hydrostatic slant factors (Figure I.2) versus elevation angle. Each subplot in the figure shows the bias introduced for each individual functional formulation.

For the hydrostatic results the use of the residuals from the least squares fit best represented the true error. In most of the plots the difference between the true error and the error predicted from the residuals is nearly zero. The use of the folding cross validation techniques actually give pessimistic results of the true error especially for low elevation angles.

The same can be said for the non-hydrostatic results. The true error is best predicted by the residuals of the least squares fit to the subset of observations. Leave-one-out CV again performed second best although slightly worse agreement between the true error and the predicted error of this technique can be seen as low elevation angles, especially in the
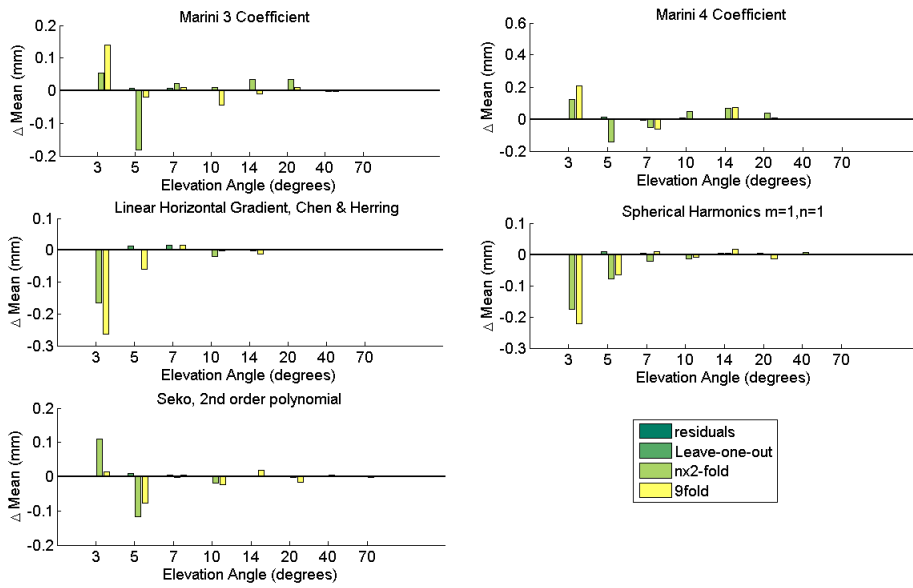
Figure I.1: Difference in mean bias due to the assessment technique for the hydrostatic component.
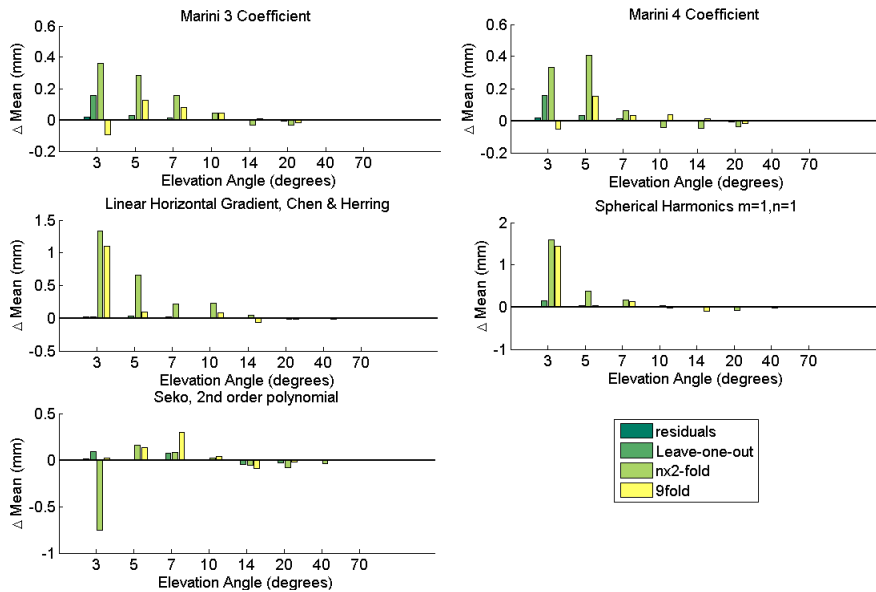

Figure I.2: Difference in the mean bias due to the assessment technique for the non-hydrostatic component.

case of the Marini expressions.

The most likely reason for the good error prediction of the residuals from the least squares fit of the subset of observations is that the functional formulations are low order expansions, and are good representations of the variation of the slant factor with respect to elevation angle. Additionally, even in the reduced data set, the number of observations to the number of unknowns is very small so this tends to prevent any over-fitting from occurring.

From these results we can conclude that the loss function (L):

$$L = \boldsymbol{r}_{sub} = \left(\boldsymbol{y}_{sub} - f(\boldsymbol{x}_{sub})\right), \tag{I.4}$$

where $\boldsymbol{r}_{sub}$ is the vector of residuals obtained from the least squares fit of the observations of the subset ($\boldsymbol{y}_{sub}$) to the functional formulation $f(\boldsymbol{x}_{sub})$, is the best technique for evaluating the functional formulations described in Chapter 3. One note of caution: these results are only valid for the observation scheme and low order formulations which were evaluated in this work and do not prove that eq. (I.4) will always be the best predictor of the true error of the functional formulation over the entire sky.

Appendix II

Ill-Conditioning

An ill-conditioned least squares problem is one in which small changes in the observations result in large changes in the estimated parameters. The condition number is a good indicator of the conditioning of a matrix. The condition number can be computed as:

$$cond(\boldsymbol{B}) = \|\boldsymbol{B}\|\|\boldsymbol{B}\|^{-1}, \tag{II.1}$$

where $\boldsymbol{B}$ is a square matrix, and $\| \bullet \|$ is the matrix norm operator. A system that is well conditioned has a condition number that is close to 1. While an ill-conditioned system has a condition number much larger than 1. Column one of Table II.1 shows the condition numbers of the Hessian matrix ($\boldsymbol{J}^T\boldsymbol{J}$) for the functional formulations evaluated in this work using the observation scheme described in section 4.2.2 (reduced observation scheme (a)). In all cases the condition number is large which indicates that the systems of equations are ill-conditioned. But, at what point is a system *too* ill-conditioned, and if so what can we do about it?

To investigate the cause of the ill-conditioning, we first study the design matrix which is populated by computing the partial derivatives of the functional formulations with respect to each unknown parameter (eq. (4.4)). Figure II.1 is a plot of the partial derivative
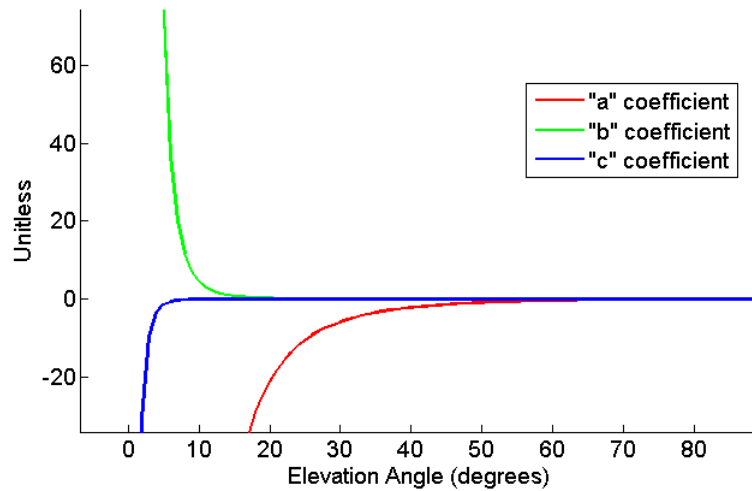
Figure II.1: Partial derivatives of the unknown coefficients of the Marini 3 coefficient expression with respect to elevation angle.

of the Marini expression, truncated at three coefficients. Notice that above an elevation angle of 30 degrees the partial derivatives look very similar. It is not until we reach and elevation angle of 15 degrees that the partial derivatives begin to diverge. This indicates the importance that low elevation angles play in fitting these coefficients as the parameters can only be uniquely determined with the inclusion of these observations.

To see if the choice of elevation angles has an impact on the condition number, the partial derivatives were computed every one degree in elevation angle and azimuth. The condition number of the Hessian matrix was then recomputed and the results compiled in the second column of Table II.1 under observation scheme (b). Although the condition numbers were reduced by an order of magnitude is some cases, overall they are still very large.

A second cause of the ill-conditioning could be due to the scaling of the Hessian matrix. Poor scaling occurs when there are large differences in the magnitude of the elements of the matrix. Normally this can be caused by inappropriate units. Equation (II.2) shows the elements of the Hessian matrix for the Marini expression truncated to three coeffi-

144

Table II.1: Condition numbers and numerical precision for IEEE double precision machine for various functional formulations, computed for observation scheme: (a) using the reduced observation set and; (b) using the full observation set

Model	Observation Scheme (a)		Observation Scheme (b)	
	Cond #	prec	Cond #	prec
Linear Horizontal Gradient (1)	8.30E+08	7	2.38E+08	8
Seko	7.34E+09	6	1.09E+09	7
Marini (3)	8.65E+08	7	2.38E+08	8
Marini (4)	1.98E+11	5	1.65E+11	5
UNSW	2.14E+11	5	1.77E+11	5
Davis	4.78E+08	7	1.27E+08	8
SH21	2.46E+10	6	2.99E+09	7
SH11	3.34E+09	6	5.61E+08	7

cients. The difference between the element (1,1) and (3,3) is on the order of magnitude of 10^5, which is poorly scaled and therefore is likely the cause of the ill-conditioning.

$$(J^T J) = \begin{bmatrix} 8936877.11158001 & -1133251.45600156 & 27997.4845715713 \\ -1133251.45600156 & 148015.01475818 & -3686.7810378304 \\ 27997.4845715713 & -3686.7810378304 & 92.0428000537618 \end{bmatrix} \cdot$$

$$(II.2)$$

How do we decided how large is too large? Overton [2001] gives a rule-of-thumb which should be used when determining if a system of equations is "too" ill-conditioned and therefore should be concerned with round-off errors. The number of significant digits of a solution is approximately equal to:

$$p = \log_{10}(eps) - \log_{10}(cond(\boldsymbol{J}^T \boldsymbol{J})), \qquad (II.3)$$

where *eps* is the floating point precision of the computing system. In our case, all computations were performed using Matlab which conforms to IEEE floating point double

precision; thereby it has 16 significant digits. The resulting numerical precision of the various functional formulations are shown in the final column of Table II.1. Boehm et al. [2008] suggest that an error of 1×10^{-5} in the a coefficient of the VMF1 which use the Marini expression, can lead to an error of 1 cm at 5 degree elevation angle. Therefore, according to the rules-of-thumb given by Overton [2001], there are enough significant digits to ensure accurate results in the fitting process.

In order to safe guard against any loss of precision in the fitting process, we have chosen to use the Levenberg-Marquadt algorithm, described in section 4.2.3. The algorithm can aid in solving poorly scaled problem by choosing to multiply the parameter λ by the diagonal of the Hessian matrix rather than the identity matrix [Mathworks, 2010], which helps normalize the matrix. Additionally, data snooping was used to identify any potential outliers, which may be due to the poor scaling of the matrice,s and these were removed before the time series analysis.

Appendix III

Observation Geometry For Assessment of Tropospheric Models

Several possibilities exist for choosing the observation geometry used for calibrating the functional formulations and in the assessment of the tropospheric models. Ichikawa et al. [2008] chose realistic satellite geometries to simulate the effect on receiver position of tropospheric slant delay errors for both symmetric mapping function and the linear horizontal gradient model. Eresmaa et al. [2008] used a similar strategy for evaluating the effect on position error of un-modeled tropospheric slant delays for a cold front passage but for fitting, a homogenous distribution of 67 hypothetical satellite positions were used to calibrate the functional formulations. Hobiger et al. [2010] and Pany et al. [2009] chose to ray-trace on a dense $1° \times 1°$ grid of the entire sky in order to obtain a complete representation of the atmosphere. In total this represents over 30,000 observations per epoch per station. We have chosen a similar strategy to Hobiger et al. [2010] and Pany et al. [2009] in that we want a uniform observation scheme over the entire sky. To achieve a substantial time series on a global set of stations some modifications were needed in order to reduce the number of observations and allow for efficient processing time.

In terms of elevation angle, it is well known that the delay increases at a rate approximately equal to $1/sin(\varepsilon)$. Therefore it would seem appropriate to choose elevation angles that are evenly spaced in $1/sin(\varepsilon)$. This would imply sampling more densely at low elevation angles, where the delay increases rapidly and less densely at higher elevation angles where the delay changes much slower. Based on past observation schemes for developing mapping functions [Boehm et al., 2006b], the final elevation angles were chosen to be $3°$, $5°$, $7°$, $10°$, $14°$, $20°$, $40°$, $70°$, and zenith.

In terms of azimuth, the maximum spacing between observation will be a function of the spatial resolution of the NWM. In our case we have chosen to use the CMC-GEM NWM which has a grid resolution of approximately 66 km at the equator. Keeping in mind that the spatial resolution of a NWM is typically 3 to 4 times that of the grid resolution, the smallest features which are resolvable by the NWM are approximately 200 km. Although there are agencies which produce NWMs with a higher spatial resolution we wanted to choose a global model to evaluate the performance of the functional formulations over a wide range of geographic and temporal conditions.

According to Ghoddousi-Fard and Dare [2007], a ray that leaves the atmosphere at 3 degrees travels approximately 700km. At the exit point the contribution of the delay is very small and the variation of the atmosphere is relatively low. As the spatial resolution of the NWM is approximately 200km, we want the distance between the two ray's as they exit the atmosphere to be no larger than this value. Keep in mind that when the ray's are propagating through the lower part of the atmosphere, where the effect of the refractivity is much greater, they will be much closer together.

Using the relationship between the radius shown in Figure III.1 and assuming that the arc distance is approximately equal to the chord distance, the difference in azimuth between two adjacent rays should be no larger than 16 degrees. In the end the spacing in azimuth was chosen to be every 10 degrees as the additional computation costs were not
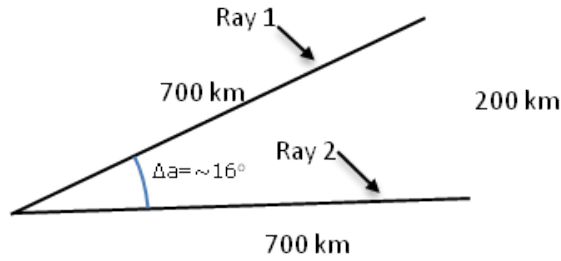
148

deemed to be significant.

Figure III.1: Spacing between observations in azimuth domain for two rays. For a ray at 3 degrees the ray exits the atmosphere at 700km. The minimum feature resolution of the CMC NWM is approximately 200 km. Therefore the spacing between the observations should be no larger than 16 degrees.

In order to evaluate the impact of the observation geometry on the calibration and assessment of the tropospheric models, the observation scheme described above was compared to a dense $1° \times 1°$ grid of observations obtained by ray-tracing through a high resolution NWM developed by the ECMWF. The horizontal grid resolution of this NWM is $0.1° \times 0.1°$, which is 6 times higher than the CMC-GEM model. Additionally, the date, August 12, 2008 and the site Tsukuba, Japan were chosen as this would represent a worst case scenario in terms of the variation of small scale phenomenon, especially the water vapor content.

Figure III.2 shows the observation sampling for the dense grid (red dots) and the reduced sampling (blue). The reduced sampling aims to only sample the delay in areas where the delay is expected to vary more rapidly. Using the assessment technique described in section 4.2.4 and validated in Appendix I, several of the functional formulations described in Chapter 3 are compared to assess the impact of the reduced observation scheme versus using the full set of observations shown in Figure III.2.

From Figures III.3 and III.4 it is possible to see that the reduced sampling has little to no impact on the conclusions which would be drawn from the assessment. The largest
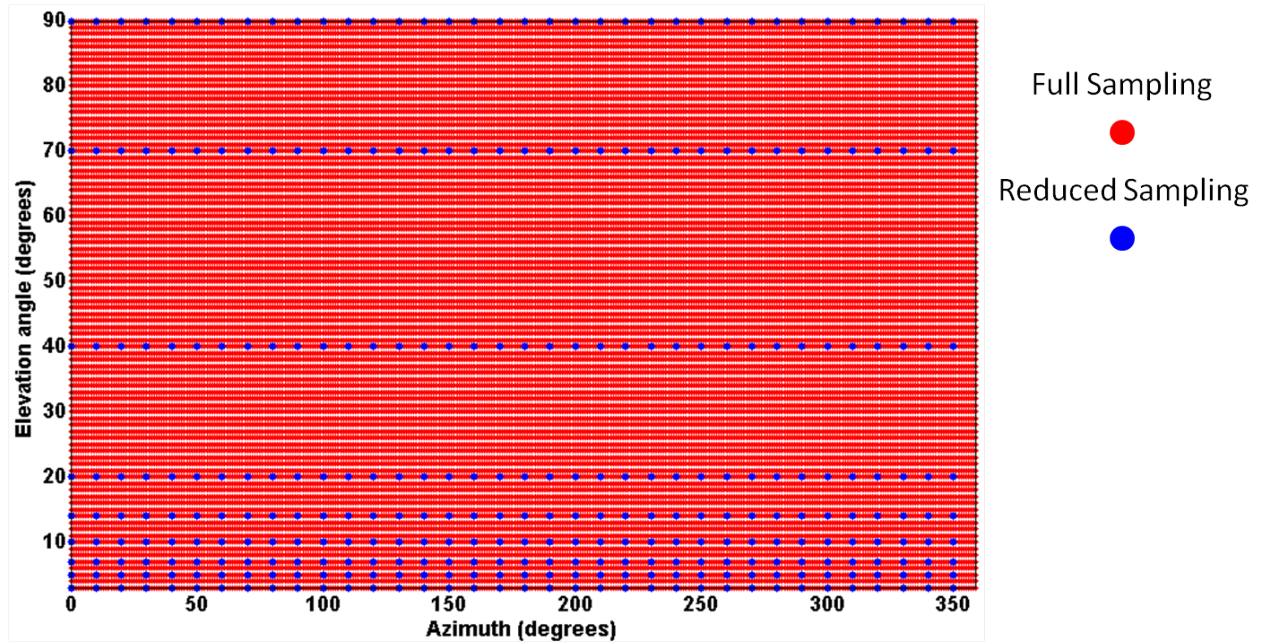
Figure III.2: Observation geometry for the full sampling (1 deg x 1 deg spacing) (red dots) and the reduced sampling (blue dots) used in this campaign.
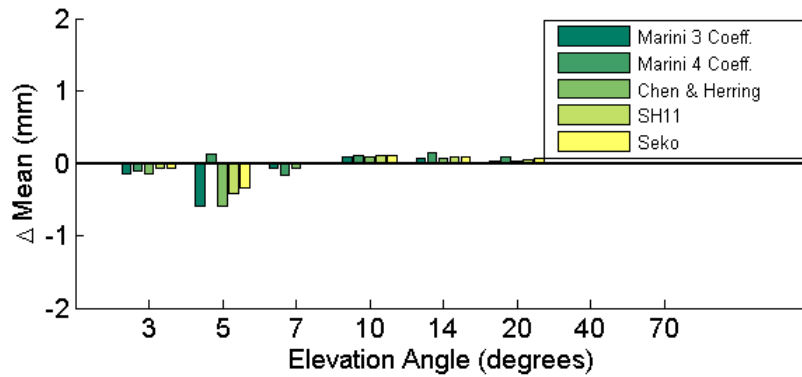

Figure III.3: Impact of the reduced sampling strategy on the mean bias between the hydrostatic ray-traced slant factors and the functional formulations

150

differences between the mean bias occur at the elevation angles of 3° and 5° and even here are less than 0.5 mm for both the hydrostatic and non-hydrostatic. For the hydrostatic case, the differences are negative below seven degrees, and positive above seven degrees. This may be due to the fact that the correlations between the observations were not accounted for. In the full observation scheme the dense sampling may not be optimal as the observations, especially at high elevation angles, will be extremely correlated. The discarding of the observations may actually aid in the fitting as it may help reduce this correlation. Ideally, each observation would be given a weight which accounts for this correlation.
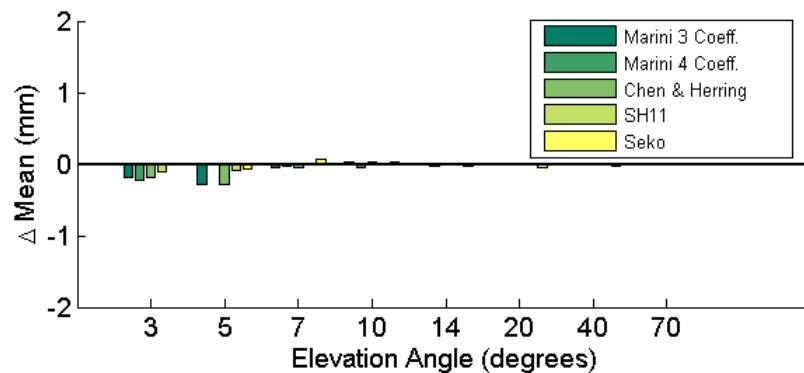

Figure III.4: Impact of the reduced sampling strategy on the mean bias between the non-hydrostatic ray-traced slant factors and the functional formulations

Comparisons of the difference in the mean of the functional formulations fitted with the reduced set and the full set indicated that differences of up to 1 mm could occur. Figures III.5 and III.6 shows the uncertainty of the functional formulations fitted using the full set of observations and the reduced observations for the hydrostatic and no-hydrostatic slant factors respectively. As the uncertainties are much larger than the 1 mm difference in mean, this would not have an impact on the conclusions drawn from our results using the reduced data set. Therefore the results indicate that the reduced observation scheme that we have chosen is a good representation of the full sky and can therefore be used to evaluate the functional formulations without introducing a bias into the conclusions.
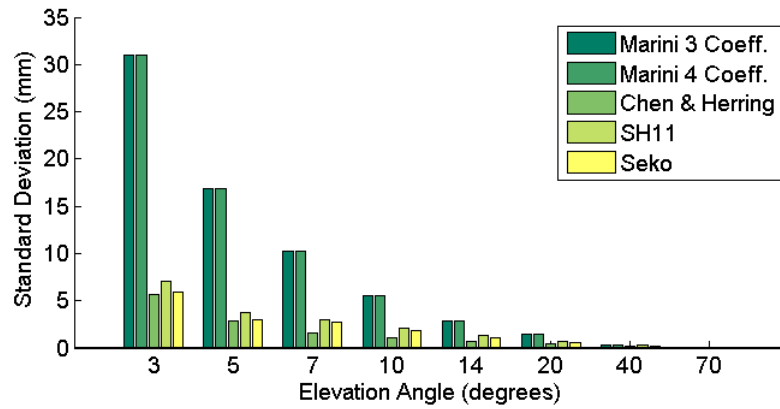
Figure III.5: Impact of the reduced sampling strategy on the standard deviation of the hydrostatic ray-traced slant factors and the functional formulations
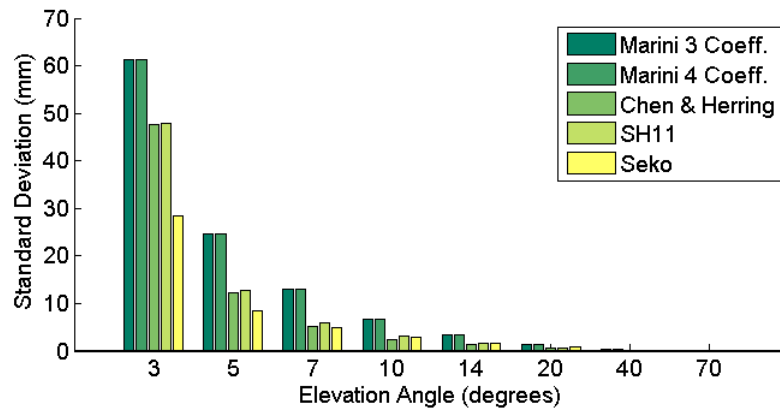

Figure III.6: Impact of the reduced sampling strategy on the standard deviation of the non-hydrostatic ray-traced slant factors and the functional formulations

Appendix IV

Ray-tracing Algorithms

The ray-tracer used in this work was originally developed in Nievinski [2009] and was adopted by this author with several modifications. Only details of the ray-tracer that are specific to this work are described below. For any further details the reader is asked to see Nievinski [2009]. Additionally, several recommendations on various elements of ray-tracing are included in the discussion.

IV.1   Propagation of the Ray Through the atmosphere

In order to evaluate the integral in eq. (2.7) and eq. (2.8) the refractivity must be sampled at discrete intervals along the ray-path. The sampling strategy employed in this work is to use a pre-defined step size defined along the ray-path. Unlike the adaptive quadrature scheme employed by Nievinski [2009] the pre-defined step size allows for the quadrature routine to be computed in one step, rather then by performing several iterations, sampling at higher and higher densities. Table IV.1 shows the location of the sampling of refractivity along the ray-path. This is the same sampling strategy employed in the benchmarking campaign performed in Nifisi et al. [2010] and confirms that the accuracy of the delay is

Table IV.1: Increments of step size, defined along the ray-path.

Length along ray-path	Increment (m)
0-2 km	10 m
2-6 km	20 m
6-16 km	50 m
16-36.5 km	100 m
36.5-136.5 km	500 m
136.5 km -infinity	1000 m

not affected by this scheme.

The solution of the full Eikonal equation (eq. (2.24))is not computationally efficient. By constraining the ray-path to a constant azimuth it is possible to greatly decrease the computation time per ray while having a negligible impact on the magnitude of the delay [Nievinski, 2009]. This can be achieved by assuming a spherical structure when computing the gradient of refractivity, ∇n, and therefore the gradient always points to the center of the sphere causing the horizontal component of the gradient to be zero. This ray-path is refereed to as the bent-2D ray-path as it is constrained to a 2D plane [Nievinski, 2009, Section 3.1.2]. Although the ray is constrained to a 2D plane, the atmosphere itself is still 3D.

For most geodetic applications we do not know the satellite's apparent direction. Instead, by assuming that the satellite or radio source is at an infinite distance, we can obtain the geometric direction to the source using the receiver position and the position of the source. However, if we ray-trace at an initial direction equal to the geometric direction, the ray will miss the target due to bending of the ray-path. Therefore, it is necessary to perform several iterations before the initial direction can be determined to the necessary tolerance. To solve the boundary value the shooting method is employed. In order to improve the convergence to the final geometric direction, the a priori bending angle formula developed by Hobiger et al. [2008a] was implemented in the software. This has no effect

154

on the end delay, only in the number of iterations before the final delay is determined.

IV.2   Elements of Ray-tracing

We evaluate the effect of stopping height, supplemental atmosphere, geopotential model and the radius of curvature of the earth on ray-traced delays. Ideally, these results can be used by future developers as a guideline for the minimum requirements for high accuracy ray-tracing.

IV.2.1   Stopping Height

The stopping height in ray-tracing is the point from which we consider the atmosphere to be represented as the vacuum of space. In the past, several different stopping heights have been employed for ray-tracing studies. Mendes [1999] reported that the contribution of the neutral atmosphere above 75 km can be ignored, although a stopping height of 100 km was employed during the ray-tracing comparisons. Hobiger et al. [2008a]considered the refractivity of the neutral atmosphere to be negligible above a height of 86 km which is the maximum heights of the parameters given in the US Standard Atmosphere 1976.

In order to establish the stopping height we have ray-traced at six elevation angles and have included results for eight stopping heights, 200, 175, 150, 125, 100, 80, 75 and 50 km. The results are shown in Figure IV.1 where the discrepancies in the total delay are given with respect to the ray-traced delay for a stopping height of 200 km (which we assume as a truth value). The y-axis is scaled logarithmically in order to make the graph more visible. It appears that using a stopping height of 80 km may introduce an error of approximately 1 mm and by increasing the maximum height to 100 km we can reduce this to only 0.01 mm error in the delay and is therefore recommended that the 100 km stopping height be used.
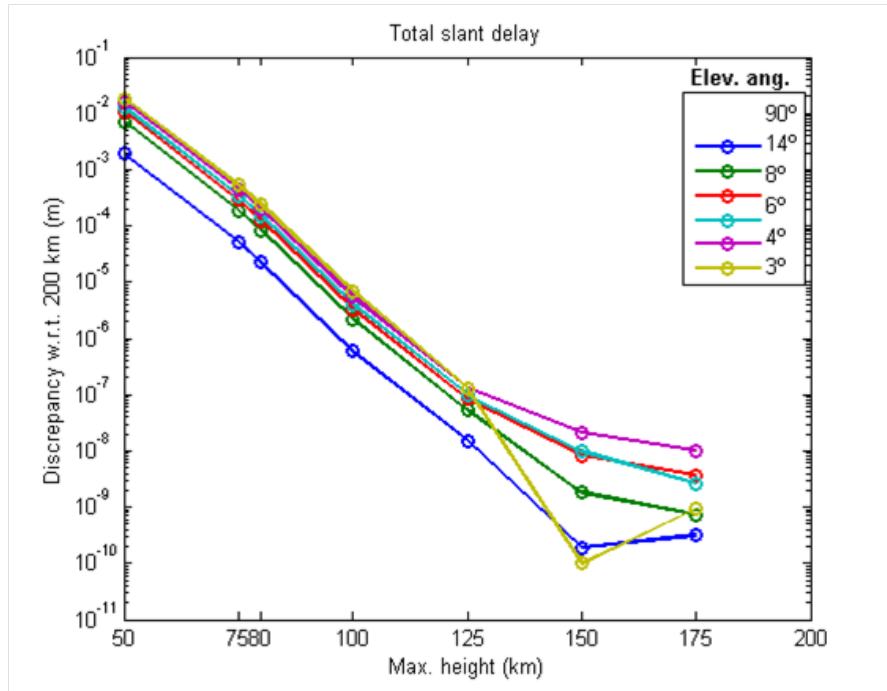
Figure IV.1: Discrepancy in total slant delays due to stopping height of ray-tracing. The discrepancies are given with respect to the delays computed using a stopping height of 200 km. The delay were computed at: $45°$ N, $-66°$ E, 23 m height on 2008/01/01

IV.2.2 Stacking of Supplemental Atmosphere on NWM

As most NWM only provide data to a pressure level near the top of the atmosphere, it is necessary to consider the refractivity occurring beyond this point, which we refer to as the pierce point of the NWM. The accuracy necessary for the supplemental atmosphere will depend on a number of factors including:

- Stacking/Extrapolation technique

- Height of the upper most pressure level (CMC 50 hPa, ECMWF 1hPa etc.)

- Stopping height of ray-tracing

- Formulation of the delay: zenith delay, slant delay, or slant factors

156

As the humidity at such altitudes is negligible, it is not necessary to extrapolate this parameter above the NWM and we can assume that the contribution of the water vapor in the atmosphere to refractivity is zero. Therefore we only consider the extrapolation of temperature and pressure above the NWM using the supplemental atmospheres.

The temperature and pressure values from the supplemental atmosphere tables cannot be used directly as this would cause discontinuities in the profiles as we move from the NWM into the supplemental atmosphere. As the pressure is more important for refractivity, we chose to discard the pressure values from the supplemental atmosphere altogether and instead rely on the hydrostatic equilibrium assumption to extend the pressure as observed at the top of the NWM to the maximum ray-tracing height using the equation [Mendes, 1999]:

$$P(i) = P_0 \frac{T(i)}{T_0}^{\frac{-g_c M}{R \beta}}, \tag{IV.1}$$

where:

$P(i)/T(i)$ – pressure/ temperature at height i in the extended profile;

P_0/T_0 – pressure/temperature at pierce point;

$g_c = 9.80665 \ m/s^2$, is the nominal constant gravity value;

$M = 28.9644\text{e-}3 \ kg/mol$, is the molar mass of dry air;

$R = 8.316963 \ J/(mol * K)$, is the universal gas constant;

β – constant lapse rate.

The values for $T(i)$ are obtained from the temperature profile of the supplemental atmosphere after a constant offset is removed between the temperature at the top of the

NWM, T_0, and the temperature of the supplemental atmosphere interpolated/extrapolated to the height of T_0, computed by:

$$T_{offset} = T_{supp}(h_{top}) - T_{NWM}(h_{top}),$$ (IV.2)

where $T_{NWM}(h_{top})$ and $T_{supp}(h_{top})$ are the temperature at the pierce point of the NWM obtained from the NWM itself and the supplemental atmosphere.

The maximum height of the pressure levels of the NWM will determine the reliance placed on the supplemental atmosphere. In the following tests we assess the impact of the supplemental atmosphere when using the CMC-GEM global run. We consider the use of three supplemental atmospheres data sets:

- Cospar International Reference Atmosphere (CIRA) 1986;

- US Standard Atmosphere (1976);

- US Standard Atmosphere (1962).

The CIRA 1986 [Chandra et al., 1990] is a monthly, mean global climatology of temperature, wind, geopotential height and pressure from the surface to a height of 120 km with a latitudinal range of 80°S to 80°N with a grid resolution of 10°. The US Standard Atmospheres [COESA, 1962, 1976], on the other hand, attempted to depict mid-latitude, year round mean conditions. The model was created to be valid at 45° N but we apply the model over the entire globe. The values for the US Standard Atmosphere 1976 were obtained from [COESA, 1976] while the profile for the US Standard Atmosphere (1962) was obtained from Nifisi [2010]. The profiles for the two versions of the US Standard Atmosphere used in this assessment are shown in eq. (IV.2).

A stopping height of 100 km was chosen for the ray-tracing, and three comparisons were performed using the global CMC-GEM. First we consider the total zenith delay

Table IV.2: Profiles of temperature and geometric height for the the US Standard Atmosphere 1976 and 1966.

US Standard Atmosphere 1976		US Standard Atmosphere 1966	
Height (km)	Temp (K)	Height (km)	Temp (K)
20	198.639	50	268
25	208.399	80	200
30	219.585	100	210
35	233.292	130	533
40	247.021	150	893
45	260.771	—	—
50	270.65	—	—
55	264.164	—	—
60	250.35	—	—
65	236.513	—	—
70	226.509	—	—
75	221.552	—	—
80	216.65	—	—

computed on a 5° x 5° grid over the entire globe for epoch 2008/08/12. Figures IV.2 and IV.3 show the discrepancy of the total zenith delays computed using the US Standard Atmosphere 1976 with respect to CIRA 1986. CIRA 1986 was chosen as the reference since it is the most recent and is able to model the seasonal and latitude variation of the parameters.

Notice that Figure IV.2 which shows CIRA1986 minus the US Standard Atmosphere 1966, we can clearly see the latitudinal "bands" which are due to the US Standard Atmosphere 1976 being fixed in latitude. Although this atmosphere was intended to be used at a latitude of 45°N the differences in the total zenith delay of +/- 0.05 mm, are well below the accuracy of the ray-traced delays. The use of the US Standard Atmosphere 1962 values on the other hand does introduce a significant bias in the total zenith delays which reach a maximum of nearly 2 cm at the poles. As the supplemental atmosphere may affect the slant delays more greatly, Figure IV.4 shows the difference in slant delay observed at a
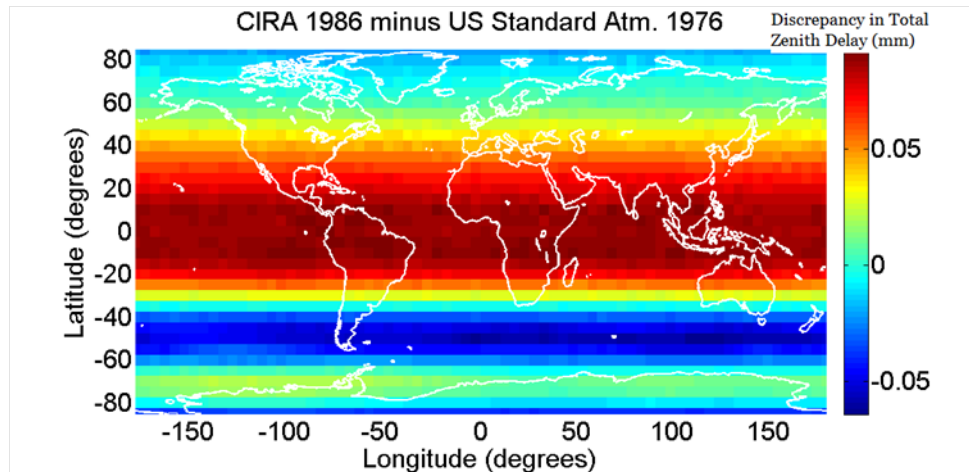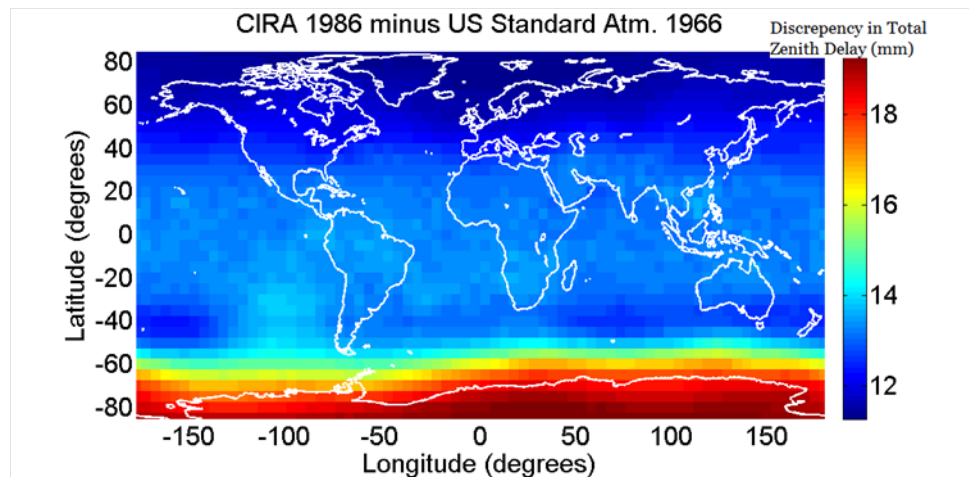
159

Figure IV.2: Discrepancy in total zenith delay due to different stacking atmospheric (CIRA 1986 and US Standard Atmosphere 1976) profiles. The zenith delays were computed on a 5° by 5° grid for the epoch 2008/08/12

Figure IV.3: Discrepancy in total zenith delay due to different stacking atmospheric (CIRA 1986 and US Standard Atmosphere 1966) profiles. The zenith delays were computed on a 5° by 5° grid for the epoch 2008/08/12

5° elevation angle, in the north direction, over the entire globe between the US standard atmosphere 1976 and CIRA 1986. Although the discrepancies are now slightly larger than in the zenith direction they are still below the accuracy level of the slant delays. The largest differences occur at the equatorial regions and near the poles.
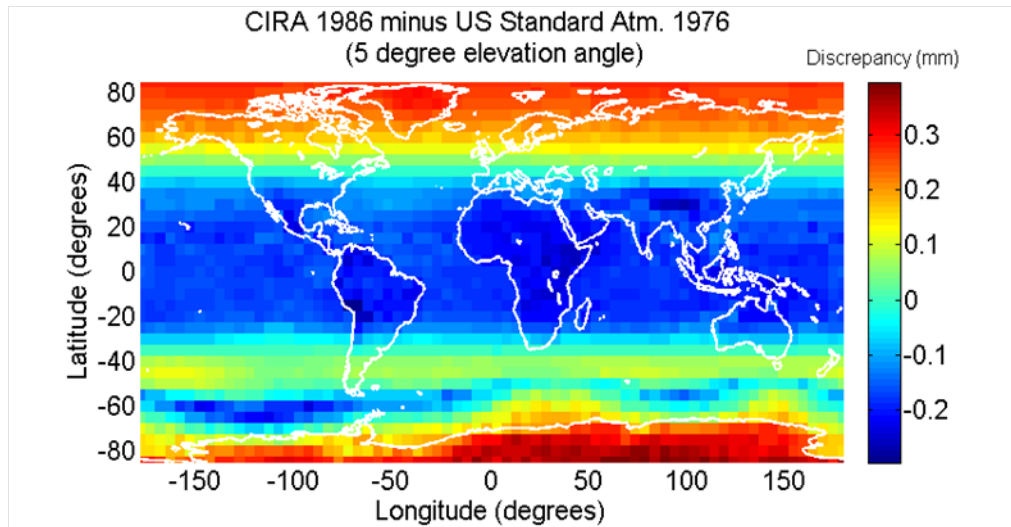

Figure IV.4: Discrepancy in total slant delay at a 5 degree elevation angle due to different stacking atmospheric (CIRA 1986 and US Standard Atmosphere 1966) profiles. The slant delays were computed on a 5° by 5° grid for the epoch 2008/08/12

In conclusion, it appears that if we use the hydrostatic equilibrium equation along with a temperature profile from a supplemental atmosphere, and properly remove any offsets occurring at the boundary of the NWM, then the complexity of the supplemental atmosphere is of little importance. A simple look up table which is only a function altitude is the only requirement, although some consideration should be given to the pressure levels of the NWM.

IV.2.3   Gravity Formulas for Converting to Geopotential Heights

In order to calculate the relative geopotential ΔW, we have compared several geopotential models including:

1. Normal Gravity: Closed Formula [Torge, 2001, p. 105, eq. 4.38] and [NIMA, 2000], infinite series in spherical coordinates; first two terms of the series in spherical coordinates [Torge, 2001, p. 107, eq. 4.46]

2. Normal gravitation, no centrifugal [Torge, 2001, p. 105, eq. 4.38, $\omega = 0$]

3. Federal Meteorological Handbook No. 3 [OFCM, 2007] Appendix D (denoted "us fmh 3" in figures)

4. EGM96, expansion up to degree and order 360 [Lemoine et al., 1998], plus centrifugal potential (denoted "actual gravity" in figures)

We perform two comparisons: 1) a single site comparison showing the discrepancies in the total zenith delay versus height for the various formulations, given with respect to actual gravity as defined above, and; 2) we compare several of the formulations on the global scale by evaluating the total slant delay, once again, on a $5°$ by $5°$ grid. We chose not to evaluate all of the formulations due to high computational cost of evaluating, for example item 4, using EGM96, for each ray-trace.

For the single site comparison, the position chosen was Fredericton, Canada ($46°$N, $-66°$W, 23m). Figure IV.5 shows the difference in zenith delay as a function of height for the different geopotenial models. Not shown on the plot is "normal gravitation, no centrifugal" as the discrepancies were two order of magnitudes larger. Overall the differences between the remaining formulations are very small, certainly sub millimeter.

In terms of slant delay we compared several normal gravity formulations and the US Federal Meteorological Handbook No. 3 formula. We once again used a 5 degree elevation angle and the north direction over the global grid. The discrepancies seen were negligible, although approaching 1mm when computed over the entire globe (Figure IV.6).
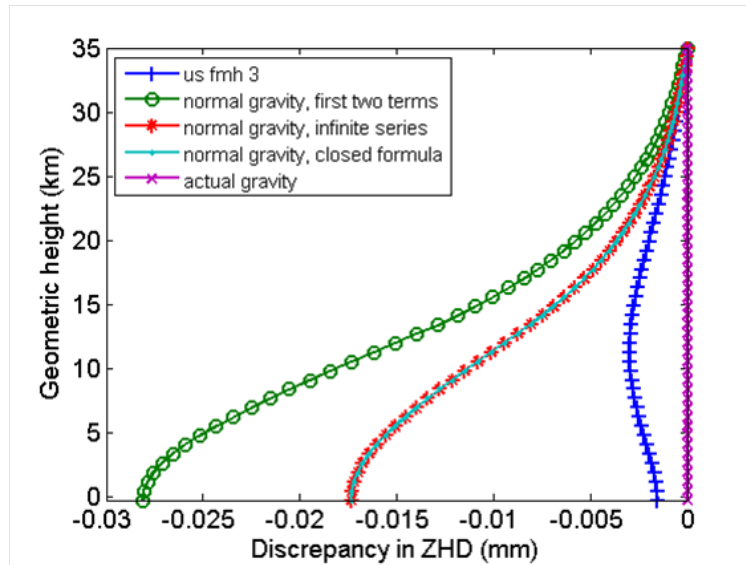
Figure IV.5: Discrepancy in zenith hydrostatic delay versus height due to different gravity formulations for Fredericton, Canada (46°N, −66°W, 23m) (After [Nievinski, 2009])
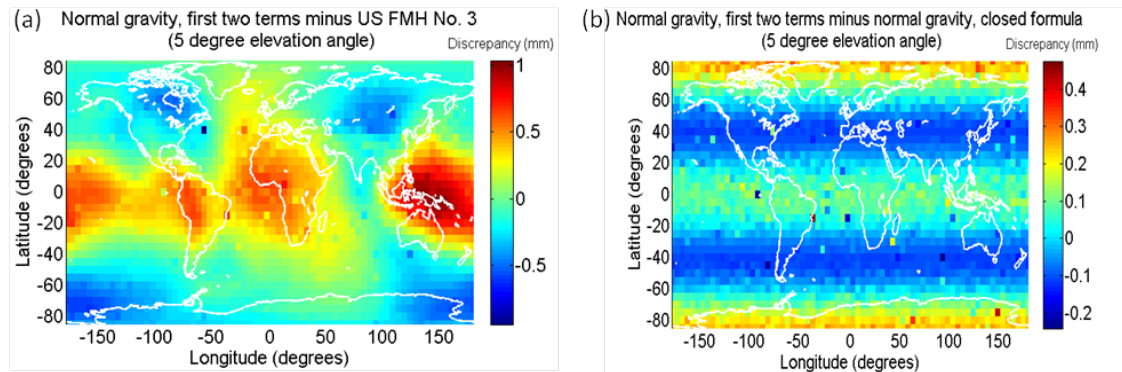

Figure IV.6: Discrepancy in total slant delay at 5 degree elevation angle over the entire globe on a 5° by 5° grid, epoch 2008/08/12. 10.a) Normal gravity, first two terms minus US Federal Meteorological Handbook No 3; b) Normal gravity first two terms, minus normal gravity, closed formula.

IV.2.4   Radius of Curvature of the Earth

The figure of the earth will have a non-negligible effect on the ray-tracing results. There are many geometrical figures of the earth, we have included some of the more common representations for computing the radius of the earth:

1. Constant Radius - $R = 6,378,100$m;

2. Gaussian Mean Curvature - $R = \sqrt{MN}$, where M and N are the curvature of the meridian and the prime vertical respectively

3. Euler's Formula - Describes a rotational ellipsoid with a radius $R = \left[\frac{\cos^2(\alpha)}{M} + \frac{\sin^2(\alpha)}{N} \right]^2$ where M and N are the curvature of the meridian and the prime vertical respectively and α is the geodetic azimuth measured in the horizontal plane between the ellipsoidal meridian plane of point P (ie. receiver) and the vertical plane containing point P and the target point [Torge, 2001, p.97]).

4. Ellipsoidal Coordinates - The atmospheric parameters are defined in ellipsoidal coordinates, therefore the radius of curvature of the earth is not computed.

We first compare the simplified earth radiuses, Gaussian mean curvature minus the constant radius. We have not included figures for zenith delay as it was found that the various definitions of the earth's radius resulted in negligible differences. Figure IV.7 shows the discrepancy in the total slant delay, at a 5 degree elevation angle, which has maximum discrepancies at the pole (4 mm) and at the equator (-5mm).

Figures IV.8 and IV.9 show the discrepancies in slant delay if the Gaussian mean curvature and the Euler formulation is used with respect to the ellipsoid coordinates. The use of the Gaussian mean curvature again causes none negligible errors at mid latitudes although at the error near the poles becomes negligible. The use of the more realistic Euler formula, shows good agreement with the ellipsoidal coordinates and can be safely
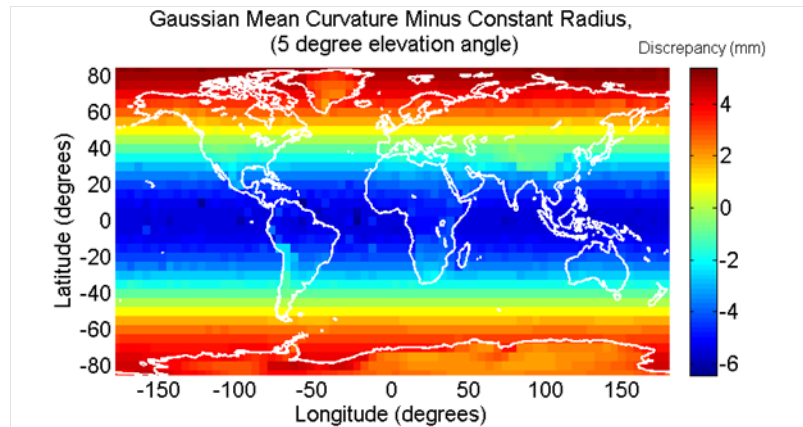
Figure IV.7: Discrepancy in total slant delay at 5 degree elevation angle over the entire globe on a 5° by 5° grid, epoch 2008/08/12, between a radius of curvature defined using a Gaussian mean curvature versus a constant radius.

used over the entire globe without introducing any significant errors in the slant delay. The impact of the different radiuses in the zenith direction is negligible.
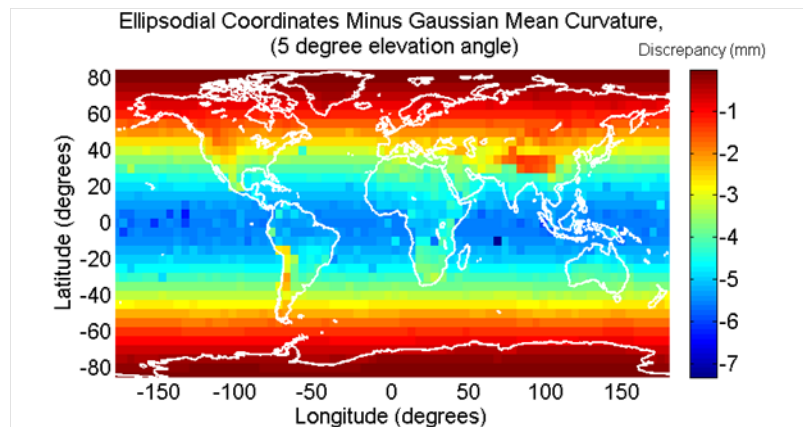

Figure IV.8: Discrepancy in total slant delay at 5 degree elevation angle over the entire globe on a 5° by 5° grid, epoch 2008/08/12, between ray-tracing in ellipsoidal coordinates and using Gaussian mean curvature.
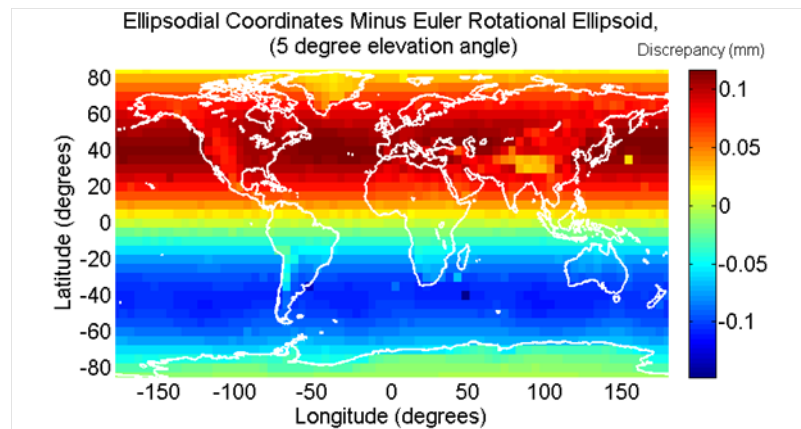
Figure IV.9: Discrepancy in total slant delay at 5 degree elevation angle over the entire globe on a 5° by 5° grid, epoch 2008/08/12, between ray-tracing in ellipsoidal coordinates and a rotational ellipsoid with a radius defined using Euler's Formula.

Vita

Full Name: Landon Andrew Urquhart

Place and Date of Birth: Dundee, Nova Scotia, Canada; June 18, 1985.

Permanent Address:
> RR#2 West Bay
> Nova Scotia, Canada
> B0E 3K0

Universities Attended:
> Acadia University, Wolfville, Nova Scotia (2003–2005)
> (Certificate of Applied Science)
> University of New Brunswick, Fredericton, New Brunswick, Canada
> (Bachelor of Science in Geodesy and Geomatics Engineering).

Publications:

Urquhart, L., F. G. Nievinski, and M. Santos (2008). "Fitting of nwm ray-traced slant factors to closed-form tropospheric mapping functions: Preliminary results." In *Geodesy for Planet Earth — Proceedings of the 2009 IAG General Assembly, , Argentina, July 2–13*, ed. M. G. Sideris, Vol. 133 of *International Association of Geodesy Symposia*, Springer, Berlin, ISBN 978-3-540-85425-8, pp. 71–79, `doi:10.1007/978-3-540-85426-5_9`.

Urquhart, L. (2009a). "Application of spherical harmonics for modeling horizontal tropospheric gradients: Preliminary results." 2009 Semi-Annual Graduate Seminar, University of New Brunswick, Department of Geodesy and Geomatics Engineering, Fredericton, N.B., March 30. (Oral presentation).

Urquhart, L. (2009b). "Atmospheric pressure loading and its effects on precise point positioning." *Proceedings of the 22nd International Technical Meeting of the Satellite Division of the Institute of Navigation — ION GNSS 2009*, The Institute of Navigation, Savannah, Ga., September 22–25, pp. 658–667, (student paper award).

Urquhart, L. (2009c). "An analysis of multi-frequency carrier phase linear combinations for gnss." Tech. Rep., University of New Brunswick, Fredericton, N.B., Canada, February, 71 pp., Technical Report 263, `http://gge.unb.ca/Pubs/TR263.pdf`.

Cao, W., A. Hauschild, P. Steigenberger, R. Langley, L. Urquhart, M. Santos, and O. Montenbruck (2010). "Performance evaluation of integrated gps/giove precise point positioning." *Proceedings of the International Technical Meeting of the Satellite Division of the Institute of Navigation*, The Institute of Navigation, San Diego, Calif., January 25–27, pp. 540–552.

Presentations:

Thirumurchi, T., L. Urquhart, R. Langley, and R. Leandro (2007). "Unb3 data management script assessment." GEOIDE Technical Workshop – Project 31, Toronto, Canada, November 18–19. (Oral presentation).

Nievinski, F. G., L. Urquhart, and M. C. Santos (2008). "Impact of mapping functions based on spherical, ellipsoidal, gradient, and 3d atmospheric structures on GPS Precise Point Positioning." Fall Meeting 2008, American Geophysical Union, San Francisco, Calif., December 15–19, Eos Trans. AGU Fall Meet. Suppl., Abstract G41A-0611. (Poster presentation).

Urquhart, L., and M. C. Santos (2008). "An analysis of multi-frequency carrier phase linaer combinations for gnss." 37th COSPAR Scientific Assembly, COSPAR, Montreal, Canada, July 13–20. (Poster presentation).

Böhm, J., L. Urquhart, P. Steigenberger, T. Hobiger, and H. Schuh (2010). "Future prospects of troposphere delay modeling in gnss analysis." Second GGOS Unified Analysis Workshop, IGS, Newcastle, UK, July 11–12. (Oral presentation).

Nifisi, V., L. Urquhart, and J. Boehm (2010). "First results of the benchmarking campaign." Workshop on Ray-tracing for Geodetic Space Techniques, IAG Working Group 4.3.3, Vienna, Austria, April 29–30. (Oral presentation).

Urquhart, L., F. G. Nievinski, and M. C. Santos (2010). "Evaluation of different strategies for mitigating azimuthally asymmetric tropospheric delays." European Geosciences Union General Assembly 2010, EGU, Vienna, Austria, May 02–07. (Poster presentation).